Alma Mater Studiorum - Università di Bologna

DOTTORATO DI RICERCA IN

ASTROFISICA

Ciclo XXXII

UNDERSTANDING THE FORMATION OF THE FIRST BLACK HOLES: DEEP OBSERVATIONS OF THE MOST DISTANT QUASARS

Presentata da: Riccardo Nanni

Coordinatore Dottorato:

Chiar.mo Prof.
Francesco R. Ferraro

Supervisore:

Dottor.
Roberto Gilli

Co-supervisori:

Chiar.mo Prof. Cristian Vignali

Esame finale anno 2020

Settore Concorsuale: 02/C1 – Astronomia, Astrofisica, Fisica della Terra e dei Pianeti
Settore Scientifico Disciplinare: FIS/05 – Astronomia e Astrofisica

"For that one fraction of a second, you were open to options you had never considered. That is the exploration that awaits you. Not mapping stars and studying nebulae, but charting the unknown possibilities of existence."
Q (Star Trek The Next Generation)

"A long time ago in a galaxy far, far away..."
Star Wars opening crawl

Contents

Executive summary

The existence of supermassive black holes (SMBHs), with $M_{BH} \sim 10^8 - 10^{10} M_\odot$, powering quasars (QSOs) up to $z \sim 7.5$, and hence formed in less than 1 Gyr, is a challenge for modern astrophysics. In order to explain these SMBH masses, accretion of gas must have proceeded almost continuously close to the Eddington limit, or even at super-Eddington rates, with fairly low radiative efficiency (η<0.1). The seeds of the observed SMBHs could either be the remnants of PopIII stars ($\sim 100 M_\odot$; Madau & Rees 2001), or more massive ($\sim 10^{4-6} M_\odot$) BHs formed from the direct collapse of primordial gas clouds (Volonteri et al. 2008). Recent simulations (e.g., Overzier et al. 2009; Costa et al. 2014; Barai et al. 2018) suggest that the most massive SMBHs at $z \sim 6$ can only form within the densest regions of the Universe that would possibly later evolve into local massive galaxy clusters. The regions around early QSOs should then feature on average galaxy overdensities, but current observations with narrow field instruments, limited to distances of $0.5 - 1$ physical Mpc (pMpc) from the QSO, did not prove conclusive (see Habouzit et al. 2016). Assessing the cosmic evolution and environment of the AGN population up to very high redshifts is a key factor to understand and constrain the early growth of SMBHs, but it requires the collection of large samples of AGN.

The majority of the quasar luminosity due to accretion processes is emitted in the optical, and ultra-violet (UV) bands. For this reason, in order to determine the quasar accretion properties, wide-area optical surveys (e.i., the Sloan Digital Sky Survey, and the Pan-STARRS Survey) have been carried out to select a large sample of QSOs. In recent years, wide-area near-IR surveys (e.i., the United Kingdom Infrared Telescope Infrared Deep Sky Survey, the VISTA Kilodegree Infrared Galaxy survey, and the Hyper Suprime-Cam survey) are pushing the QSO redshift frontier above $z = 6$, allowing the detection of the most distant QSOs discovered so far: ULAS J1120+0641 at $z \sim 7.1$ (Mortlock et al. 2011), and ULAS J1342+0928 at $z \sim 7.5$ (Bañados et al. 2018). In addition, deep X-ray surveys, such as the 7 Ms *Chandra* Deep Field South (CDF-S; Luo et al. 2017), the 2 Ms *Chandra* Deep Field North (CDF-N; Xue et al. 2016), and the AEGIS-X survey (Nandra et al. 2015), are a primary source of information regarding the accretion mechanism of the compact objects, providing a highly efficient method

of pinpointing growing black holes in active galactic nuclei (AGN) across a wide range of redshifts and luminosities, and offering insights about the demographics, physical properties, and interactions with the environments of the SMBHs. In particular, deep X-ray surveys are able to investigate the accretion of SMBHs even at very high-z, allowing us to study even the very obscured sources that are difficult to detect with optical/NIR surveys.

The X-ray emission of optically selected, unobscured QSOs at high-redshift ($z \sim 6$) has been presented in previous works for a limited number of sources. In this thesis work we provide a systematic analysis and study of all the X-ray data available for $z \sim 6$ QSOs in order to derive the general properties of accretion of SMBHs in the early Universe (Nanni et al. 2017). To this purpose, we selected and studied all QSOs with spectroscopic redshifts $z > 5.5$ and observed in the X-ray band to date, including the deepest ($\sim$ 500 ks) *Chandra* observation ever obtained for a $z \sim 6$ QSO, SDSS J1030+0524. Comparing the results obtained from this X-ray analysis with those derived from past X-ray observations, we discovered the first example of an X-ray variable QSO at $z > 6$ (Nanni et al. 2018).

Deep and wide imaging observations of a 8×8 physical-Mpc^2 region around SDSS J1030+0524 showed that this field features the best evidence to date for an overdense region around a $z \sim 6$ QSO (Morselli et al. 2014; Balmaverde et al. 2017). In the last few years, our group has obtained data at different wavelengths (including the $\sim$ 500 ks *Chandra* observation) to further investigate and confirm the presence of the putative galaxy (and AGN) overdensity. We indeed used our deep *Chandra* observations to build a catalog of X-ray detected sources (Nanni et al. in prep.) with multi-wavelength information that will be used in future works to search and find possible obscured/faint AGN at the QSO redshift.

This quest for overdense regions around early SMBHs was also complemented by an optical/NIR search for large-scale (up to $\sim$ 20 physical-Mpc away) QSO companions around 75 known $z \sim 6$ QSOs discovered in the Pan-STARRS survey (Bañados et al. 2016). From this study we found 25 good QSO companion candidates that will be followed-up with future spectroscopic observations.

Chapter 1

Introduction

1.1 What are Active Galactic Nuclei?

Active Galactic Nuclei (AGN) are a heterogeneous class of extragalactic sources in which the emission from the galactic nuclear region is so powerful that cannot be ascribed to stellar emission processes. About $1 - 10\%$ of all galaxies contain an AGN and are characterized by very large luminosities (up to $L_{bol} \approx 10^{48}$ erg/s, e.g., Wu et al. 2010), much larger than ordinary galaxies, that are produced in a small center region (within 1 pc[3]).

From a historical point of view, E. A. Fath was the first scientist that observed in 1908 the presence of strong broad emission lines in the optical spectrum of a galaxy, without knowing they were emitted by an AGN. Later, V. M. Slipher got a higher resolution spectrum of the same object, discovering that the line broadening corresponded to fast velocities of >100 km/s. In 1937 C. Seyfert was the first to detect strong high-excitation emission lines in spiral galaxies. This new category of sources was then classified as Seyfert galaxies. In 1959, Woltjer tried to extrapolate the physical properties of Seyfert galaxies. In particular, he found that the emission was coming from the central part of the galaxies ($r < 10$ pc). Assuming the virial equilibrium and using the dispersion velocities derived from the broadening of the emission lines ($v \sim 10^3$ km/s), he estimated the mass at the galaxy center:

$$M \approx \frac{v^2 r}{G} \approx 10^9 M_\odot \tag{1.1}$$

Following this idea, Zel'dovich e Novikov suggested in 1964 that the huge measured luminosities are related to accreting processes on a super massive black hole (SMBH), that acts as a central engine. This was recently confirmed with the publication of the first image of a SMBH powering the AGN at the center of M87 galaxy by the Event Horizon Telescope (EHT) Collaboration (2019).

In later times, a complex taxonomy was developed in order to classify AGN mainly on the basis of optical or radio emission characteristics. To first order, AGN are divided into Type 1 and Type 2 AGN depending on the broadening (a full width half maximum of $FWHM \sim 10^4$ km/s for Type 1 and $FWHM \sim 1000 - 2000$ km/s for Type 2) of the emission lines in the optical spectra, and into radio-loud (RL) and radio-quiet (RQ) AGN on the basis of the radio emission power. The effort to explain the different properties of the numerous classes of AGN led to the development of the so called "unified model for AGN" (e.g., Antonucci 1993; Urry & Padovani 1995; Chiaberge et al. 2000). The basic idea is that AGN belonging to different classes are powered by the same engine seen at different orientations, although, in some cases, intrinsic physical diversities must be taken into account. According to that, the main elements of a typical AGN (shown in Fig. 1.1) are:

- A central super massive black hole with mass $M = 10^{6-10}\ M_{\odot}$, that is working as a central engine of the AGN.

- A rotating, viscous accretion disk of gas falling towards the black hole. The temperature of the disk (up to $T \sim 10^6$ K) depends on the distance from the black hole (outer layers are cooler than inner ones) and on the black hole mass. This could explain the emission in optical/UV as a multicolor black-body, a sum of different temperature black-body spectra, with brightness:

$$B_{\nu}(T) = \frac{2h\nu^3}{c^2} \frac{1}{e^{\frac{h\nu}{kT}} - 1} \tag{1.2}$$

  where ν is the emitted frequency. The sum of the black body spectra produced by the different layers of the accretion disk produces a power-law spectrum with $F_{nu}\ \alpha\ \nu^{\frac{1}{3}}$.

- A gaseous, rarefied and highly ionized hot corona located in proximity of the disk having a diffuse or clumpy structure depending on the models and a temperature $T \sim 10^9$ K. The hot corona is necessary to explain the high-energy X-ray emission through Inverse Compton (IC) interactions of the low-energy thermal photons emitted by the disk with the relativistic electrons of the corona. However, the heating mechanism of the corona is not known yet (Lusso & Risaliti 2017).

- The Broad Line Region (BLR), probably made by gaseous clouds close to the central engine (up to 100 light days) having a density $n_e \sim 10^{10-11}$ cm^{-3}, too high to emit forbidden lines, and a temperature $T \sim 10^4$ K. The emission lines (like the hydrogen Balmer series) have a large width, typically 10^{3-4} km s^{-1}. The principal broadening mechanism is Doppler motion of

individual clouds, being the thermal broadening $\Delta v \sim \left(\frac{kT}{n_p}\right)^{0.5} \sim 10$ km s^{-1} for a $T \sim 10^4$ K gas.

- A dusty cool torus surrounding the central regions at a distance $R \sim 0.3 - 3$ pc. This torus is optically thick: its temperature must be lower than the dust sublimation temperature, which can vary for different dust composition (e.g., $T_{subl} \sim 900$ K for silicates, $T_{subl} \sim 1800\,K$ for graphite). The presence of the torus is necessary to explain why Type 2 AGN are obscured, but its structure and geometry are still not well known: several models were developed proposing a homogeneous or clumpy distribution with different density and temperature profiles (e.g., Jaffe et al. 2004; Burtscher et al. 2013). The torus emits thermally in the infrared (IR) band. From the observational point of view, the higher is the AGN luminosity, the more distant is the torus from the central BH. This can be explained by the so called "Receding Torus Model" (e.g., Lawrence 1991; Simpson 2005), that links the AGN luminosity to the radiative pressure that is pushing the torus farther away (e.g., Ricci et al. 2017; but see Lusso et al. 2013).

- The Narrow Line Region (NLR), made by gaseous clouds beyond the BLR (up to 100 - 1000 pc from the central BH), with a density $n_e \sim 10^{3-4}$ cm^{-3} and a temperature $T \sim 10^3$ K. Thanks to its low density the lines emitted in this region have a typical width of a few 10^2 km/s, and forbidden lines, like the [OIII] at 5007 Å and 4959 Å, can be emitted under these physical conditions: the low density of the gas decreases the probability that collisional de-excitation occurs before the radiative de-excitation which, for forbidden lines, has very long time scales.

- Relativistic jets, perpendicular to the torus plane, which emit mostly through synchrotron mechanism from the radio band to the γ-rays. These structures may extend up to $R \sim 1$ Mpc. The mechanism originating them is not completely understood, but it seems related to the black hole rotation-driven magnetic field (e.g., Pudritz et al. 2012). The interaction between the jets and the ambient medium causes the formation of the hot spots and the lobes. Only radio-loud AGN (that constitute 1-10% of the whole AGN population) show the presence of prominent jets.

The different features of the several classes of AGN can then be explained in terms of the AGN structure and orientation, as shown in Fig. 1.1. First, the presence or absence of the jets determines the main distinction between radio-loud and radio-quiet AGN, respectively. Regarding radio-loud AGN, the radio emission becomes more and more important as the line of sight (l.o.s) approaches the jet axis. This is easily explained by the relativistic beaming affecting the synchrotron

emission. Thus radio galaxies, i.e. radio-loud AGN for which the l.o.s. forms a wide angle with the jet axis, are weaker radio sources than blazars, for which that angle is close to zero. The orientation does not affect the mid-IR luminosity (mainly emitted by the dusty torus itself) which indeed is similar for the two classes. Type 2 AGN are obscured by the molecular torus, hence the BLR is not visible and their spectra do not show broad lines. Type 1 AGN, for which the l.o.s. does not intercept the torus, show both narrow and broad lines. Blazar spectra are characterized by a very blue and featureless continuum.

The demonstration of the unification between Type 1 and 2 AGN is coming from the observation of the broad polarized emission lines found in Type 2 Seyfert galaxies (Antonucci 1993): these polarized lines have the same wavelength and intensity of those observed in Type 1 AGN, and can be interpreted as emission lines coming from the BLR that are scattered from the central regions (dusty particles or electrons) of the AGN. This scattering polarizes the broad emission lines and diffuses them in different directions, allowing us to observe them despite the obscuration of the BLR from the dusty torus. However, not all the differences between the different classes of AGN can be ascribed to the different torus orientation. In fact, the difference between the RL FRI (in which the jet emission dominates over the lobes one) and the RL FRII (in which the emission of the hot spots and lobes are dominant) seems to be related to a difference in the accretion mechanism (Ghisellini & Celotti 2001; Padovani 2017). Furthermore, the unification between Type 1 and 2 AGN is demonstrated for low-redshift, low-luminosity sources but it may not be valid for higher redshifts, where Type 1 and 2 AGN can be just different phases in the evolutionary scenario of the AGN (see §1.6).

1.2 The Black Hole paradigm

As explained in §1.1, the main element that is responsible for the AGN emission is a SMBH, surrounded by an accretion disk, that works as central engine capable to produce high luminosities in a very small volume (1 pc^3). According to the current paradigm, the viscous material falling inwards heats up to $T = 10^6$ K giving rise to thermal emission. The source of energy is thus the conversion of gravitational potential energy to radiation (optical and ultraviolet) and thermic energy of the falling gas. Assuming that the rate of energy emission is supplied by accretion, the luminosity (L) is:

$$L = \eta \dot{M} c^2 \tag{1.3}$$

where η is the efficiency of the process and $\dot{M}$ is the mass accretion rate. Inverting the equation, the mass accretion rate can be derived from the source luminosity:

$$\dot{M} = \frac{L}{\eta c^2} \approx 1.8 \times 10^{-3} \frac{L_{44}}{\eta} \quad \frac{M_\odot}{yr} \tag{1.4}$$

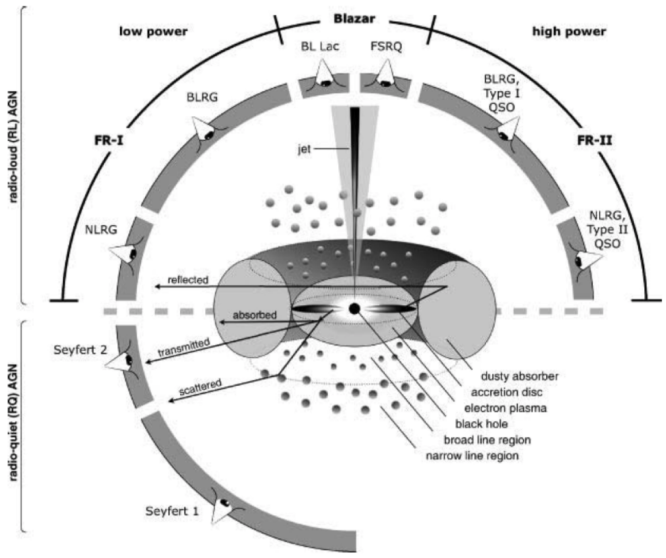

Figure 1.1: The typical AGN structure. Black lines indicate the AGN main components according to the unified model while the different AGN classes are labelled in the figure. Radio-loud AGN are shown in the upper part of the figure, radio-quiet AGN in the lower one. The sizes are not scaled. Adapted from Beckmann & Shrader (2012).

where L_{44} is the the bolometric luminosity in units of 10^{44} erg/s. The potential energy U of a mass particle m at a distance r from the central object of mass M is:

$$U = \frac{GMm}{r} \tag{1.5}$$

thus, we can derive the conversion rate of potential energy into radiation:

$$L \approx \frac{dU}{dt} = \frac{GM\dot{M}}{r} \tag{1.6}$$

From (1.3) and (1.6) we obtain $\eta \ \alpha \ M/r$, i.e. the "compactness" of the system which is maximized in case of black holes, resulting in a very high efficiency value. The size of a black hole (the event horizon) can be defined in terms of the Schwarzschild radius R_S that is, in the case of a non-rotating black hole:

$$R_S = \frac{2GM}{c^2} \approx 3 \times 10^{13} M_8 \quad cm \tag{1.7}$$

where M_8 is the mass of the black hole in units of $10^8 M_\odot$, We can estimate η in the classical limit considering the simplified case of a particle of mass m at $5R_S$. From (1.5) and (1.7) we derive:

$$U = \frac{GMm}{5R_S} = 0.1mc^2 \tag{1.8}$$

resulting in $\eta \approx 0.1$, namely the second most efficient energy production mechanism in the Universe (as the first one is the matter-antimatter interaction with $\eta = 1$, while the third is the thermonuclear fusion of the hydrogen in stars with $\eta \approx 0.007$). On the basis of such a high efficiency, even a modest accretion rate can easily explain the high AGN luminosities. In fact, from equation (1.4), with $\eta = 0.1$ and $\dot{M} = 0.1\ M_{\odot}/yr$, we get $L_{bol} \approx 10^{45}\ erg/s$, that is consistent with what we observe for luminous AGN (e.g., Brandt & Alexander 2015).

1.3 The Eddington Luminosity

The Eddington luminosity (L_E) represents the theoretical maximum luminosity that an AGN can emit without blowing away the accreting material through radiation pressure. It is defined as the luminosity at which the radiative pressure equals the gravitational one so, at high luminosities, the AGN might be able to blow away the accreting material. Even in the case of spherical accretion of fully ionized gas, the L_E of a SMBH of mass M can be obtained balancing the radiative pressure with the gravitational one:

$$L_E = \frac{4\pi G c m_p M}{\sigma_T} \approx 1.26 \times 10^{38} \frac{M}{M_{\odot}}\, erg\, s^{-1} \tag{1.9}$$

where $m_p = 1.67 \times 10^{24}$ g is the proton mass and $\sigma_T = 6.65 \times 10^{-25}\ cm^2$ is the Thomson cross-section. The Eddington luminosity can be used to derive estimate of the mass of the central SMBH: putting the observed luminosity of an AGN in equation (1.9) we can derive a lower limit on the mass of the SMBH (the so called Eddington mass or M_E):

$$M_E \approx 8 \times 10^5 L_{44} \quad M_{\odot} \tag{1.10}$$

Considering the typical luminosities of the known AGN we obtain a typical mass range for the SMBHs of $10^6\ M_{\odot} < M < 10^{10}\ M_{\odot}$.

However, it is important to notice that some AGN can emit in a super-Eddington regime (i.e., $L > L_E$). This happens because one or more of the assumptions are wrong, particularly the spherical geometry. In the case of a spherical geometry, the AGN can emit at $L > L_E$ during particular phases of AGN activity, although for short period of time (like several bursts of super-Eddington accretion followed by quiescent phases; e.g., Pezzulli et al. 2017).

1.4 The Black Hole Spin

According to the "no hair theorem", BHs can be described by three main parameters: the BH mass M, the angular momentum J, and the electric charge Q (neutral

BHs have $Q = 0$). In the case of non-rotating BHs ($J = 0$), the space-time around them can be described using the Schwarzschild metric; in the case of rotating BHs the Kerr metric is needed. Defining the gravitational radius (r_g) as:

$$r_g \ = \ \frac{GM}{c^2} \tag{1.11}$$

and the adimensional angular momentum or spin (a) as:

$$a \ = \ \frac{Jc}{GM^2} \tag{1.12}$$

we can compute the event horizon in units of r_g as:

$$R_h \ = \ 1 + (1 - a^2)^{\frac{1}{2}} \tag{1.13}$$

from which we can deduce that $-1 < a < 1$ (negative values of a indicate BHs that are counter-rotating wrt the accretion disk). For a non-rotating BH ($a = 0$, the Schwarzschild metric case) $R_h = 2$ and the innermost stable circular orbit (ISCO) is $R_{ISCO} = 6r_g$, while for a maximally rotating BH ($|a| = 1$, the Kerr metric case) $R_h = 1$ and $R_{ISCO} = 1.23r_g$. In §1.5.4 is shown that the value of a can have important consequences on the iron emission line that is observed at 6.4 keV.

1.5 Continuum emission from AGN

AGN are capable to emit, with high intrinsic luminosities, virtually at all wavelengths. In this section are described both the different types of emission from the radio to the gamma bands and the physical processes involved. In Fig. 1.2 we show a typical broadband spectral energy distribution (SED) for three classes of AGN. The main features that are labelled in the figure are described in detail below.

However, it is important to consider that generally AGN are variable objects from the IR to the X-rays, with timescales spanning from few days (for IR/optical bands) to few hours/minutes (in the X-rays). Consequently, it is challenging to compare and derive common information from spectra of the same AGN that have been observed in different times. Furthermore, AGN IR/optical and X-ray spectra can be modified by absorption processes related to the dusty torus or to the interstellar medium (ISM) present in the host galaxy or in the Milky Way.

1.5.1 Radio emission

AGN radio emission is non-thermal and is originated by the synchrotron mechanism, resulting in a power-law spectrum (e.g., Risaliti & Elvis 2004):

$$F_\nu \ \alpha \ \nu^{-\alpha} \tag{1.14}$$

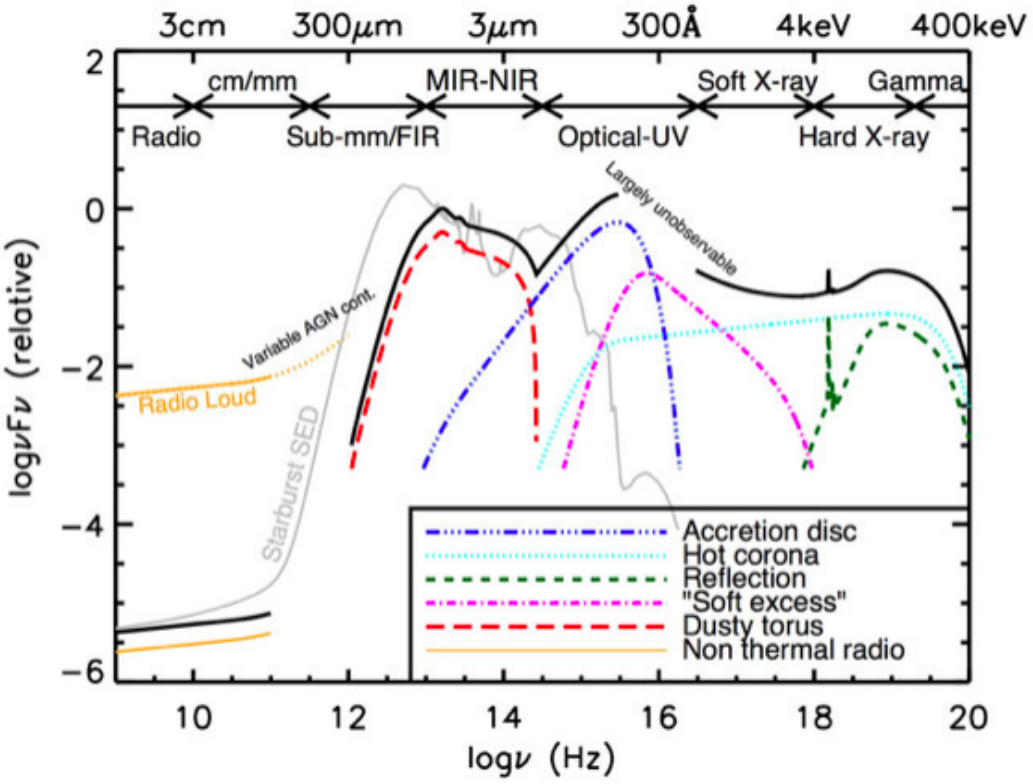

Figure 1.2: Schematic representation of the broadband continuum spectral energy distribution seen in the different types of AGN. The main features are labelled in the figure and described in §1.5. From Harrison (2014).

where F_ν is the flux at frequency ν and α is the power-law spectral index. In synchrotron emission, the relativistic electrons having a Lorentz factor γ and a mass m_e are accelerated by magnetic fields of intensity B and emit at a characteristic frequency $\nu\ \alpha\ BE^2$, where $E = \gamma m_e c^2$. Given a power-law energy distribution for the electron population of:

$$N(E)dE\ \alpha\ E^{-\delta}dE \tag{1.15}$$

where $N(E)$ is the number of electrons with energy within E and $E + dE$, the emission spectrum is a power-law in the form of equation (1.14), where $\alpha = \frac{\delta-1}{2}$, at least for frequencies larger than a critical (or "break") value ν_B, which depends on the medium density and the linear dimension of the emitting region. Below ν_B the spectrum is self-absorbed and $F_\nu \propto \nu^{2.5}$. Radio emission is only a small part of the bolometric luminosity for radio-loud AGN, and is even smaller for radio-quiet ones.

The radio emission is manly coming from the jets, the hot spots and the lobes.

The jets are a plasma of relativistic particles accelerated by the magnetic field in the innermost regions of the AGN, and ejected in polar directions up to Mpc scales, where they can interact with the external medium. In some AGN the jet-medium interactions produces large radio-lobes and hot spots, that are regions where the jets collide and interact with the external medium, producing shocks and strong synchrotron emission.

1.5.2 IR emission

The AGN IR emission has a thermal origin and is produced by the dusty torus that surrounds the central region. The dust grains absorb the UV photons emitted by the accretion disk and re-emit the radiation in the near and mid-IR bands. The spectral shape shows a maximum, the "IR bump", at a $\lambda = 10 - 30\mu m$, corresponding to a temperature $T \sim 1000$ K. Since the temperature of the dusty torus is ten times higher than the one of the ISM dust heated by starlight, the peak of the AGN IR emission falls in a region of the host-galaxy SED where no other significant component is present, while in the near-IR bands a significant contribution from stars is expected and the galactic cold dust emission dominates in the far-IR.

However, there are also hints of non-thermal IR emission for FRI radiogalaxies, which show a correlation among near IR, optical and radio nuclear luminosity suggesting the same synchrotron origin for the emission in those bands and the absence or a small contribution from the torus (Chiaberge et al. 1999).

1.5.3 Optical/UV emission

The optical/UV emission is dominated by an excess of energy emitted at wavelengths shorter than 4000 Å called "Big Blue Bump", originated by the sum of multi-color black body emission from the accretion disk, as described in §1.2. The high-energy decreasing wing of the blue bump is absorbed by cold gas in the interstellar medium in the Milky Way that prevents observation below 0.3 keV. In the optical band it is also possible to observe the presence of both broad and forbidden narrow emission lines coming from the BLR and the NLR, respectively.

1.5.4 X-ray emission

The X-ray emission is characterized by a main power-law component (see Fig. 1.3) produced by inverse Compton processes (IC) inside a hot plasma ($T \sim 10^9$ K) called "Hot Corona". The variability on short timescales suggests that the hot corona reside in the innermost region of the AGN ($r << 10^4\ R_S$), however the spatial distribution and the geometry of the corona are still unknown (e.g.,

Chartas et al. 2016; (2017)). From the physical point of view, low-energy thermal photons emitted by the disk are up-scattered in the X-ray band by hot-thermal electrons in the corona. The resulting spectrum is a power-law resulting from the superposition of many scattering orders of the intrinsic black body:

$$F_E \; \alpha \; E^{-\Gamma} \tag{1.16}$$

where Γ is the photon index of the power-law and is defined as $\Gamma = \alpha + 1$, where $\alpha = \frac{-ln\tau}{lnA}$ is the spectral index, τ is the optical depth, $A = e^y$ is the average energy gain in each scattering, and $y = \frac{4kT}{m_e c^2}\tau$ is the Comptonization parameter (e.g., Lanzuisi et al. 2019). The spectrum shows a high energy cut-off at $\sim 100-300$ keV, corresponding to the temperature at which electrons and photons are thermalized. The X-ray spectrum also shows a "soft excess" (cyan line in Fig. 1.3) red-ward of 1 keV whose origin is still uncertain (Done et al. 2012).

The primary power-law component is reflected by the Compton thick ($N_H >> 1.5 \times 10^{24}$ cm^{-2}) disk. This reflection component (green line in Fig. 1.3) creates a hardening of the spectrum, the third bump (after the IR bump and the "Big Blue Bump" described in §1.5.2 and §1.5.3, respectively) in AGN SEDs, known as Compton or Reflection Bump, which peaks at ~ 30 keV. The intensity of this secondary component depends on many factors, such as the geometry and the ionization state of the reflecting material. Reflection from the torus can also be present.

Besides all of these components, several X-ray spectra present absorption features at 1 keV (purple line in Fig. 1.3), due to ionized gas having an equivalent hydrogen column density of $N_H \sim 10^{22}\ cm^{-2}$, a ionization parameter $log\xi \sim (0-2)$, and $T \sim 10^{4-5}\ K$ (Kaastra et al. 2000; Kaspi et al. 2000). These warm absorbers could be also responsible for absorption features in the UV spectrum that are blueshifted relatively to the broad emission lines. The blueshift suggests that the absorbing gas is outflowing from the central regions and, possibly, concides with the wind responsible for the absorption features in the Broad Absorption Lines (BAL) quasars, if high velocities are involved (Tombesi et al. 2013).

The Iron K_α line at 6.4 keV

One of the most important features in X-ray spectrum is the iron (Fe) K_α emission line at 6.4 keV for neutral or lowly ionized iron (red line in Fig. 1.3) produced through fluorescence (Fabian et al. 2000) in the accretion disk, the BLR and/or the dusty torus. This process can happen if the neutral iron is in an excited state due to the ionization of the K shell produced by a photon with energy > 7.1 keV. The de-excitation transition lead a higher energy state electron to occupy the free K shell, emitting a K_α (6.4 keV) photon $\sim 90\%$ of the time (when the electron is coming from the L shell), or a K_β (7.06 keV) photon (when the electron is coming

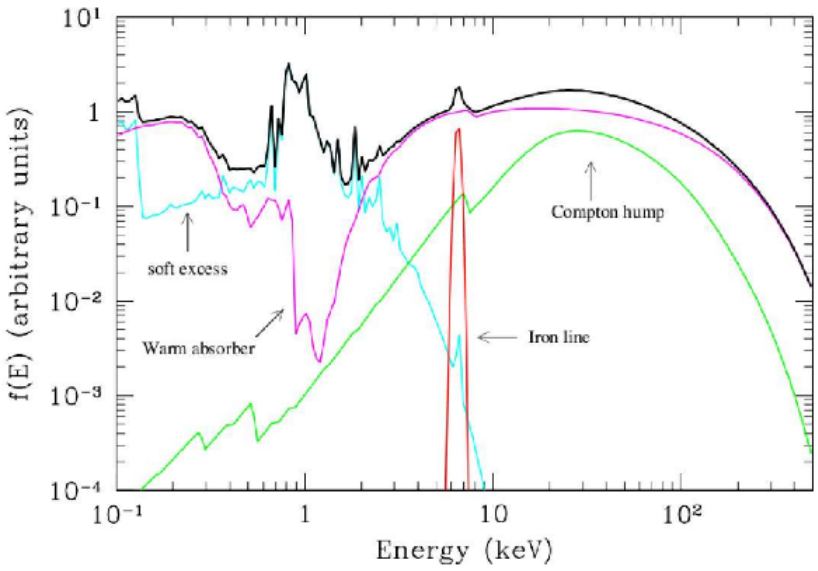

Figure 1.3: X-ray spectrum of a typical Type 1 AGN in arbitrary units, from Risaliti & Elvis (2004). The black line is the total spectrum, sum of the several components shown in different colors. The purple line is the main power-law with a high energy cut-off at 100-300 keV and the absorption caused by the warm absorbers at 1 keV. The green line shows the reflection component, the Compton Hump. The cyan line represents the soft excess. The red gaussian line represents the emitted iron line (K_α) at 6.4 keV.

from the M shell). In some cases, the emitted photon can in principle be absorbed by an outer electron which is in turn ejected (Auger mechanism). If the Fe atom was previously ionized, there would be less electrons screening the K shell from nuclear attraction and the fluorescent photon energy would be slightly larger (up to 7 keV for the H-like iron transition). The probability for having a fluorescent emission rather than the Auger mechanism is called "fluorescent yield" (Y), and is defined as:

$$Y \sim \frac{Z^4}{Z^4 + 33^4} \tag{1.17}$$

where Z is the atomic number. From equation (1.17) it is clear that the maximum value of Y is reached by iron (since $Z_{Fe} = 26$ and is more abundant than the heavier elements), and that explains why the K_α is the most prominent line in the X-ray spectrum.

If the Fe K_α is emitted in the innermost layers of the accretion disk, it will be affected by relativistic effects due to the presence of the black hole, in addition to the classic Doppler effect given by the disk rotation (Fabian et al. 2000). The sum of classic and relativistic transverse Doppler effect and relativistic gravitational redshift results in a red-shifted double-peaked broadened line profile, having the

blue peak enhanced and a large red wing (Fig. 1.4). Several other variables, such as the inclination angle (Fig. 1.5 left), the disk ionization state and the emissivity profile of the disk emission, contribute in shaping the line profile.

Since the relativistic effects on the Fe K_α depend on the distance from the central SMBH, it is possible to derive an upper limit for the R_{ISCO} and, hence, study the spin of the BH. As explained in §1.4, the R_{ISCO} depends on the spin of the BH: for a non-rotating BH (Schwarzschild metric) $R_{ISCO} = 6r_g$, while for a maximally rotating one (Kerr metric) $R_{ISCO} = 1.23r_g$. Assuming that the Fe K_α line is produced at R_{ISCO}, its shape is different depending on the two cases (Kerr or Schwarzschild case, see Fig. 1.5 right).

Also the intensity of the line depends on several variables such as the geometry of the system, the inclination angle, the Fe abundance, and the disk ionization state. In particular, it was observed that more luminous AGN show Fe K_α lines with lower intensity (Iwasawa & Taniguchi 1993). That can be related to the complete ionization of the disk produced by the higher luminosities with a consequent intensity fading of the line.

1.5.5 γ-ray emission

γ-ray emission is generally observed in blazar that show a peak of emission in this band. The γ-ray luminosity is very high for these objects ($L \sim 10^{46-48}$ erg/s) and the emission is due to IC processes of the relativistic electrons coming from the jets with the radio photons either produced by synchrotron processes by the electrons themself or photons coming from the disk. The particular emission process that produces both radio photons (synchrotron radiation) and γ-rays (IC radiation) is called "Synchrotron Self Compton" (SSC).

1.6 AGN Demography and Evolution

Several X-ray studies have been performed to trace the AGN evolution since $z \sim 5$ (Miyaji et al. 2000; Ueda et al. 2003; Hasinger et al. 2005; La Franca et al. 2005; Aird et al. 2008; Silverman et al. 2008; Gilli et al. 2011; Ueda et al. 2014; Aird et al. 2015; Buchner et al. 2015). In particular, these works showed that the comoving AGN space density is not constant over time. It is shown in Fig. 1.6 that the comoving space density of luminous QSOs (green line) is particularly low at $z \sim 6$ ($1\,Gpc^{-3}$), then increases toward lower redshifts, and decreases again at $z < 2$. The space density of high-luminosity ($L_{bol} > 10^{45}$ erg s^{-1}) AGN has a peak at $z \sim 2-3$ and then exponentially decreases up to $z \sim 6$, while the space density of low-luminosity AGN peaks at $z \sim 0.5-1$ and decreases up to $z \sim 4$. This effect is known as "AGN downsizing" and is similar to the cosmic downsizing

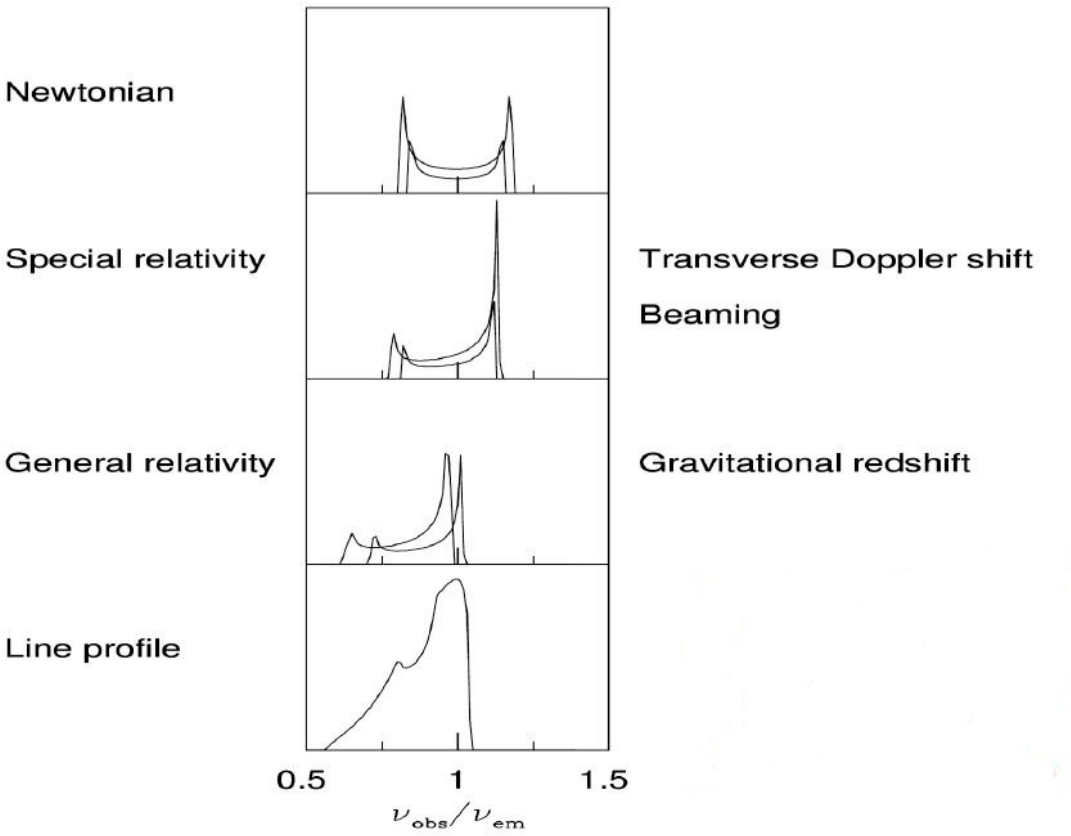

Figure 1.4: Main contributions to the Fe K_α line profile (from Fabian & Miniutti 2005). From top to bottom, the classic Doppler split of a line emitted by an edge-on rotating disk, with the blue peak corresponding to the approaching part and the red one to the receding; the relativistic beaming enhancing the blue peak and the relativistic transverse Doppler effect are added; the gravitational redshift broadening the red wing and shifting the line to lower energies is added. The profiles at two different radii are represented in these panels. The last panel shows the line resulting as the sum of all the effects integrated over the entire disk.

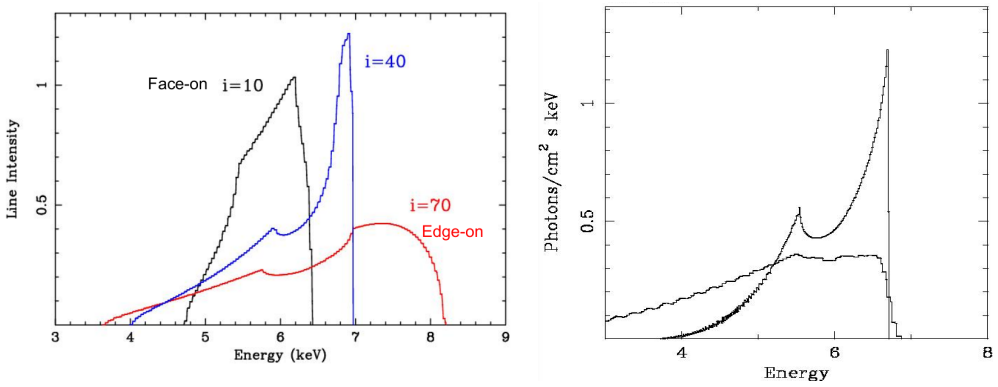

Figure 1.5: Left panel: Fe K_α line profile for non-rotating (Schwarzschild) BH observed at different inclination angles (i). The broadening of the line increases with increasing inclination angle and the double peak is more prominent. Right panel: Fe K_α line profile for a non-rotating (Schwarzschild) BH (the one with a prominent double peak) and for a rotating (Kerr) BH (the broader line), assuming that the emission is coming from R_{ISCO}. The Kerr BH is more influenced by the gravitational relativistic effect since it is produced closer to the central BH ($R_{ISCO} = 1.23 r_g$). This effect broadens and extends the emission line at lower energies than the one produced by a Schwarzschild BH. Figures taken from Fabian et al. (2000).

of galaxies (e.g., Cowie et al. 1996; Fontanot et al. 2009, and references therein), implying that the most massive BHs formed and grew at earlier time compared to the low mass ones. In particular, it has been observed that the space density of $logL_X > 44.1$ AGN decreases by a factor of ten in the range $3 \leq z \leq 5$ (Vito et al. 2014), and by a factor of 20 in the range $3 \leq z \leq 6.2$ (Marchesi et al. 2016).

Several analytical models were proposed in order to parametrize this behavior. The two most popular models are the Luminosity Dependent Density Evolution model (LDDE; Miyaji et al. 2000; Ueda et al. 2003; La Franca et al. 2005; Hasinger et al. 2005; Silverman et al. 2008; Ueda et al. 2014), originally proposed by Schmidt & Green (1983) to describe the evolution of optically-selected AGN, in which the space density of AGN evolves differently for different luminosities and there is no actual evolution in luminosity, and the Luminosity And Density Evolution (LADE) model (Aird et al. 2010), which assumes that the AGN population evolves independently in luminosity and density with cosmic time.

A possible evolutionary scenario emerging from past works (e.g., Hopkins et al. 2008; Hickox et al. 2009) suggests that the activity of luminous ($L_{2-10\,keV} \geq 10^{44}$ erg/s) AGN, triggered by major gas-rich mergers (e.g., Di Matteo et al. 2005; Menci et al. 2008), occurs in short bursts (with timescales of the order of ~ 0.01 Gyr; e.g., Alexander et al. 2005). In this case, the gas accretion is chaotic (Hopkins et al. 2008) and may produce a large covering factor and column densities. This phase of strong accretion is hidden by the Compton-thick material, until it is blown away by the radiation and the gas outflows emitted by the AGN (feedback),

and the AGN shines as an unobscured quasar until a new gas-rich merger event occurs. Since the merging rate (Kartaltepe et al. 2007) and, most importantly, the gas fraction (Carilli & Walter 2013) increases with redshift, the fraction of obscured AGN may then increase as well (e.g., Treister & Urry 2006; Vito et al. 2013). This feedback scenario is also invoked to explain the observed correlations between the mass of the central BH and the properties of the host galaxy, such as the stellar velocity dispersion in the bulge, the mass and luminosity of the bulge (e.g., Magorrian et al. 1998; Ferrarese & Merritt 2000; Marconi & Hunt 2003; Häring & Rix 2004; McConnell & Ma 2013; Kormendy & Ho 2013, and references therein). According to this scenario, which is at the basis of the so called BH-galaxy co-evolution, when a wet merger event occurs, it may provide new gas to the central SMBH and triggers the accretion process obscuring the AGN emission (Hopkins et al. 2008). This large amount of accreting gas can also trigger the star formation in the host galaxy until the AGN is powerful enough to produce a negative radiative/kinetic feedback that halts the star formation and blows away the obscuring gas. In Fig. 1.7 we report a schematic summary of the different phases of the BH-galaxy co-evolution model described above.

Beside the evolution of the whole AGN population, it is important to assess the evolution of the obscured AGN fraction, usually defined as the fraction of AGN obscured by a column density $N_H > 10^{22}$ cm^{-2} with respect to the total number of AGN. The obscured AGN fraction is found to increase at least up to $z = 2 - 3$ (e.g., La Franca et al. 2005; Tozzi et al. 2006; Treister & Urry 2006; Hasinger 2008; Treister et al. 2009; Merloni et al. 2014; Ueda et al. 2014), while the obscured AGN fraction at high-redshift is still unconstrained. Even though X-rays are less biased towards obscuration than optical/NIR bands, obscured AGN are difficult to be detected at high-redshift, since they are typically fainter and hard to identify in optical surveys than unobscured objects. Therefore, computing the obscured AGN fraction at high-redshift, where the available samples of AGN are small, is not an easy task. Moreover, there is no estimate on the fraction of obscured, low-luminosity AGN at high-redshift.

1.6.1 The origin of the first SMBHs

The discovery of $z > 6$ QSOs with SMBHs with $M = 10^{8-10}$ $M_\odot$ (e.g., De Rosa et al. 2011; Fan 2012, Wu et al. 2015; Bañados et al. 2017), when the Universe was less than 1 Gyr, poses a great challenge for theory: models of SMBH formation and growth must face the challenge represented by the presence of these massive objects when the Universe was so young (e.g., Mortlock et al. 2011; Bañados et al. 2018; Onoue et al. 2019). Eddington-limited or even super-Eddington accretion is usually required by models of BH seed formation to reach such masses in a few hundreds million years. Different scenarios have been proposed to explain

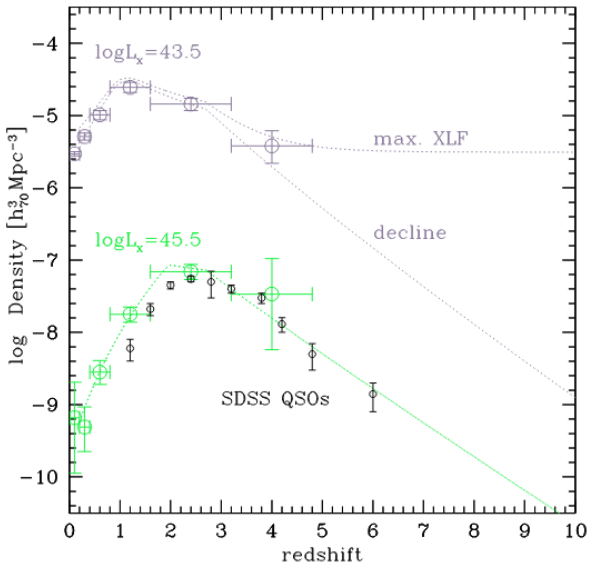

Figure 1.6: Comoving spatial density versus redshift for $logL_X = 43.5$ (purple line and dots) and $logL_X = 45.5$ (green line and dots) unobscured AGN (from Gilli et al. 2011). The comoving spatial density of the more luminous AGN ($logL_X = 45.5$) peaks $z \sim 2-3$ and then exponentially decreases up to $z \sim 6$. The density of lower-luminosity AGN peaks at $z \sim 0.5 - 1$ and then decreases at least up to $z \sim 4$. Black dots represent the comoving space density derived from luminous QSOs of the Sloan Digital Sky Survey (SDSS; Richards et al. 2006).

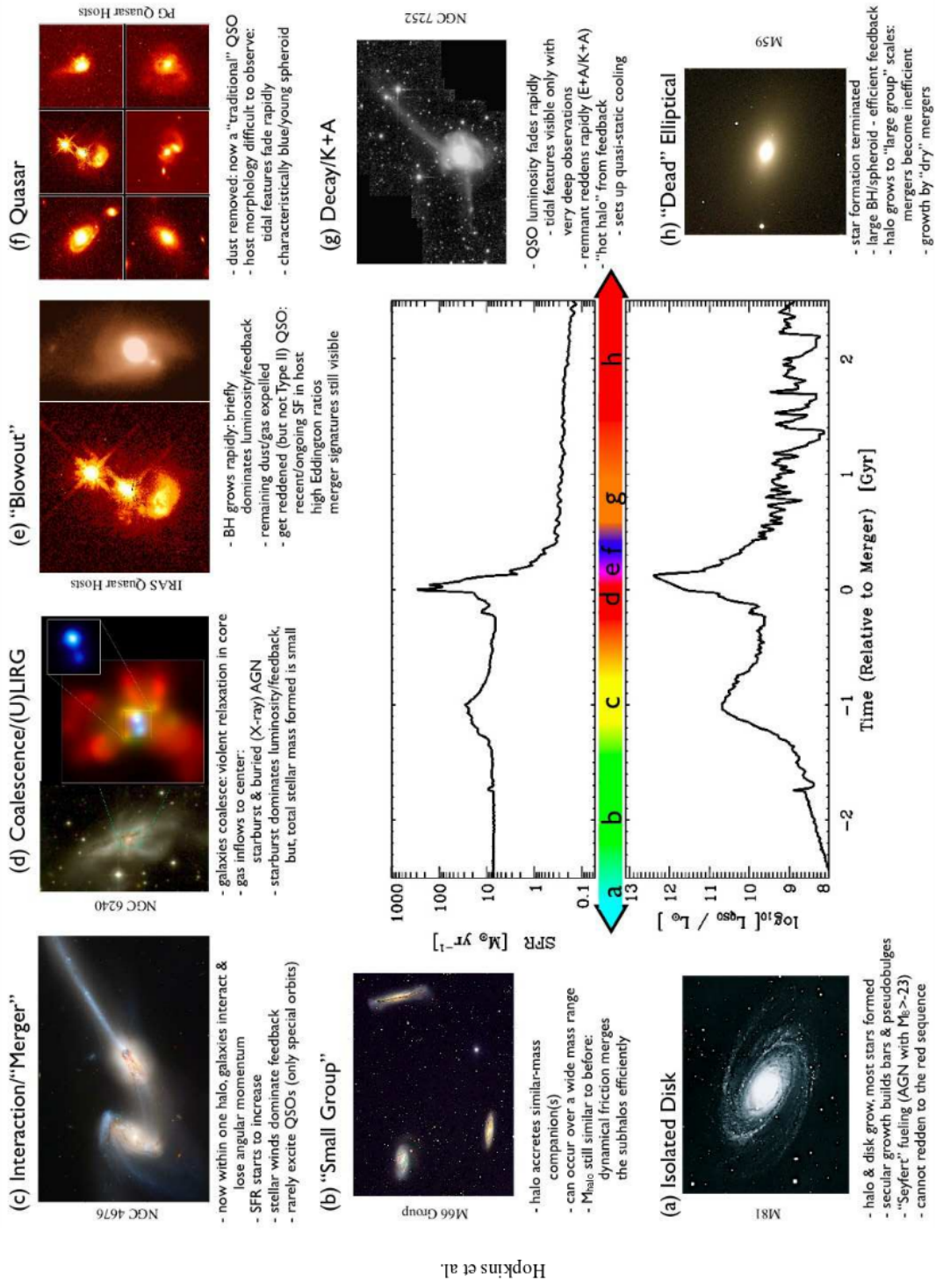

Figure 1.7: Schematic figure of the different evolutionary phases of a primordial galaxy after a wet merger event, according to the BH-galaxy co-evolution model (taken from Hopkins et al. 2008). The scheme should be read clockwise from (a) to (h). The big central panel shows the temporal evolution of the star formation rate (upper part), and luminosity of the quasar (lower part). During the supply of gas in the central part of the galaxy ($d - e$ phases) there are both the peaks of star formation and quasar emission. On later stages, the QSO quenches the SFR and expels the gas from the central region. Then, also the QSO luminosity fades away and the host galaxy turns into a passive one.

the formation of the BH seeds that eventually became SMBHs by $z \sim 6$. The two most promising ones involve either the remnants of PopIII stars (100 $M_{\odot}$; e.g., Madau & Rees 2001; Volonteri & Rees 2006; see Fig. 1.8 upper panel), or more massive (10^{4-6} $M_{\odot}$) BHs formed through the direct collapse of primordial gas clouds (e.g., Volonteri et al. 2008; Agarwal et al. 2014; Valiante et al. 2016; see Fig. 1.7 lower panel). In the case of low-to-intermediate mass ($M \leq 10^4$ $M_{\odot}$) seeds, super-Eddington accretion and low radiative efficiency are required to form the black-hole masses observed at $z > 6$ (see Fig. 1.7 left; e.g., Volonteri & Rees 2006; Madau et al. 2014; Volonteri et al. 2016; Pezzulli et al. 2017).

From the theoretical point of view, from equations 1.3 and 1.9 it is possible to derive the BH mass grow rate:

$$\frac{dM}{M} = \frac{4\pi G m_p}{c\sigma_T \eta} dt = \frac{dt}{\tau \eta} \tag{1.18}$$

where $\tau = \frac{4\pi G m_p}{c\sigma_T} = 4.6 \times 10^8$ yr. Assuming that η is time independent, it is possible to derive the BH mass (M) at a certain time (t):

$$M = M_0 e^{\frac{(1-\eta)t}{\tau\eta}} \tag{1.19}$$

where M_0 is the initial mass of the BH seed. Equation 1.9 shows that it is possible to grow a BH up to $M \sim 10^8$ $M_{\odot}$ in 5×10^8 yrs starting from a BH seed of $M_0 = 10^4$ $M_{\odot}$ However, this computed mass should be treated as an upper limit, since we assumed that the AGN is continuously accreting at Eddington rate for the entire growth phase. In reality, SMBHs rarely emit at such high luminosity and the accretion rate is not constant through time. How these SMBHs formed in the early Universe is still an open issue (Mazzucchelli et al. 2017).

There is general agreement that early massive BHs form in overdense environments, that may extend up to 10 physical Mpc (pMpc), and host large gas quantities (Overzier et al. 2009; Dubois et al. 2013; Costa et al. 2014; Barai et al. 2018). According to simulations, the fields around high-redshift QSOs are expected to show galaxy overdensities, which probably represent the progenitors of the most massive clusters in the local Universe (Springel et al. 2005). In the past decade, large efforts have been made to find overdense regions in fields as large as 2x2 pMpc^2 around $z \sim 6$ QSOs (e.g., Stiavelli et al. 2005; Husband et al. 2013; Bañados et al. 2013; Simpson et al. 2014; Mazzucchelli et al. 2017), but the results were inconclusive. Some of them ascribed the lack of detection of overdensities at very high-z to the strong ionizing radiation from the QSO that may prevent star formation in its vicinity. The presence of strong gas jets and/or radiation feedback extending up to few hundreds of kpc at $z = 6$ is, in fact, predicted in modern simulations of BHs formation (Costa et al. 2014; Barai et al. 2018). In particular, in Fig. 1.8 (bottom panel) it is shown that the evolution with redshift of BH mass in

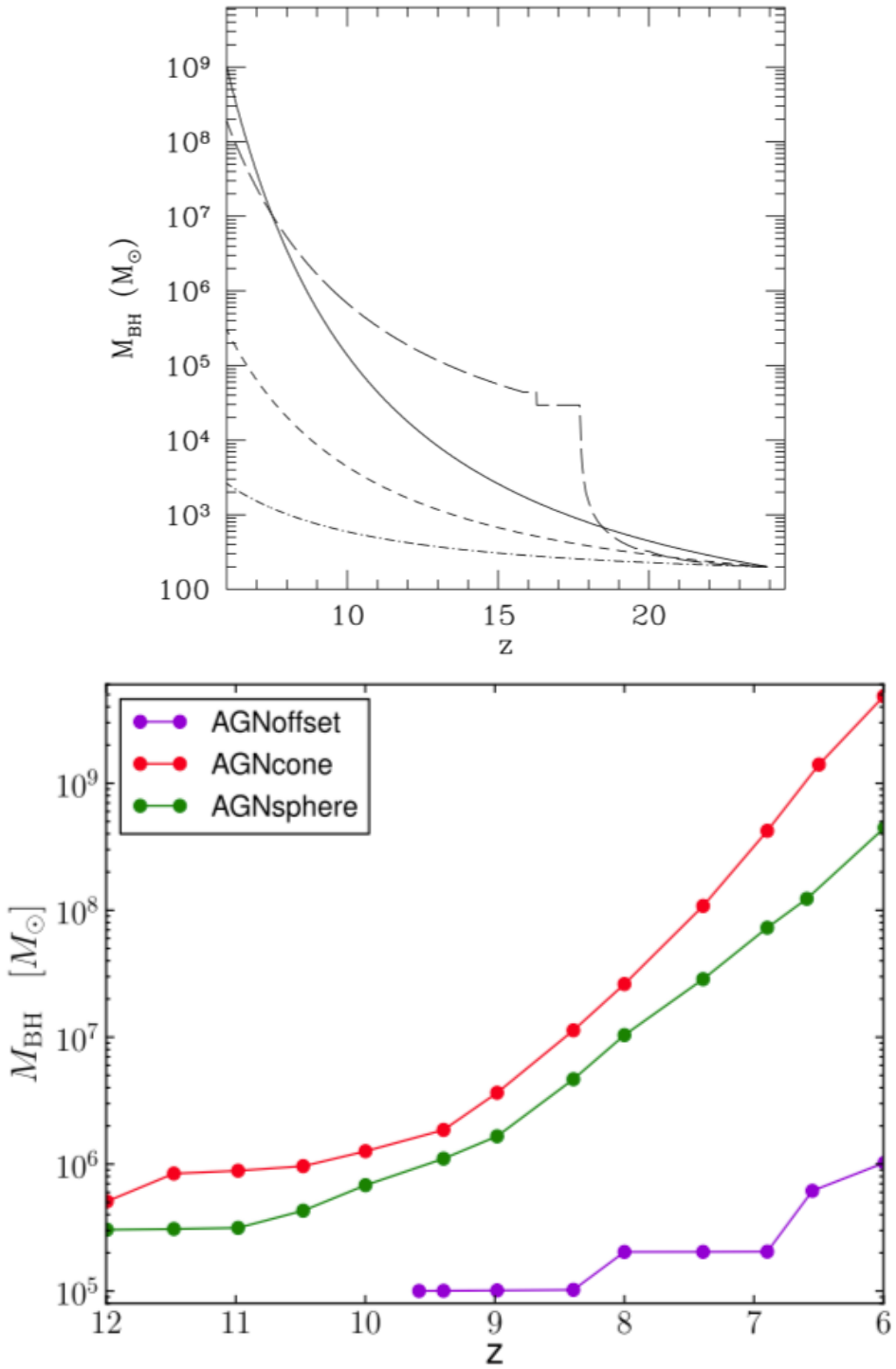

Figure 1.8: Upper panel: Evolution with redshift of BH mass in the early Universe under different assumptions for the accretion rate and efficiency (from Volonteri & Rees 2006). Eddington-limited accretion with $\eta = 0.1$ (solid line), $\eta = 0.2$ (dashed line), $\eta = 0.4$ (dot-dashed line), and super-Eddington accretion (long-dashed line). Only in the cases with low radiative efficiency (solid line) or super-Eddington accretion (long-dashed line) it is possible to form the observed BH masses at $z \sim 6$. Lower panel: Evolution with redshift of BH mass in the early Universe under different assumptions for the environment and feedback geometry (from Barai et al. 2018): bi-cone kinetic feedback from the central QSO (red line), spherical kinetic feedback (green line), and the case in which the BH is not formed at the center of the dark matter halo (purple line). In this simulation a radiative efficiency of $\eta = 0.1$ is assumed, while the accretion rate is evolving with time, reaching its maximum (Eddington accretion) at $z \sim 8 - 9$ in the feedback cases.

the early Universe changes under different assumptions for the environment and feedback geometry: assuming an asymmetric, bi-cone kinetic feedback from the central QSO (red line), the BH mass can easily grow to $M_{BH} > 10^9\ M_\odot$ at $z = 6$, while for a symmetric, spherical kinetic feedback (green line) the BH mass stops at $M_{BH} \sim 10^8\ M_\odot$ at $z = 6$. In the case in which the BH is not formed at the center of the dark matter halo (purple line), it can not even reach the lowest masses ($M_{BH} \sim 10^8\ M_\odot$) observed at $z \sim 6$.

Chapter 2

X-ray properties of z∼6 luminous QSOs

In this chapter we provide a systematic analysis of all X-ray data available in 2016 for 29 $z \geq 5.5$ QSOs that were observed either by *Chandra*, XMM-*Newton*, or *Swift*-XRT, in order to derive the general properties of accretion onto SMBHs at very high-redshift. The results of this chapter have been published in Nanni et al. (2017), but see also Vito et al. (2019) and Salvestrini et al. 2019 for a more up-to-date analysis that includes new observed X-ray QSOs at $z \geq 6$.

Multi-wavelength observations showed that these QSOs are evolved systems with large black hole masses ($10^8 - 10^{10}$ $M_\odot$; Mortlock et al. 2011; Wu et al. 2015; but see also Fujimoto et al. 2019), and large amount of gas and dust, and intense star formation in their host galaxies ($M_{gas} \sim 10^{9-10}$ $M_\odot$, $M_{dust} \sim 10^{8-9}$ $M_\odot$, SFR up to 1000 $M_\odot$/yr; e.g., Calura et al. 2014; Venemans et al. 2016; Venemans et al. 2017; Gallerani et al. 2017*a*; Decarli et al. 2018). Optical and NIR observations showed that the broad-band spectral energy distributions (SEDs) and the rest-frame NIR/optical/UV spectra of QSOs have not significantly evolved over cosmic time (e.g., Mortlock et al. 2011; Barnett et al. 2015).

As of today, $\sim$ 300 QSOs have been discovered at redshift $z > 5.5$ with wide-area optical and IR surveys (e.g., Fan et al. 2006; Willott et al. 2010; Venemans et al. 2013; Matsuoka et al. 2016; Bañados et al. 2016; Yang et al. 2017; Bañados et al. 2018; Matsuoka et al. 2018; Matsuoka et al. 2019, and reference therein). In particular, wide-area near-IR surveys are now pushing the QSO redshift frontier to $z > 6.4$. Only a limited fraction of these $\sim$ 300 QSOs have been studied through their X-ray emission (e.g., Brandt et al. 2002; Farrah et al. 2004; Vignali et al. 2005; Shemmer et al. 2006; Moretti et al. 2014; Page et al. 2014; Ai et al. 2016; Nanni et al. 2017; Nanni et al. 2018; Vito et al. 2019; Pons et al. 2019). These studies showed that the X-ray spectral properties of high-redshift quasars do not differ significantly from those of AGN at lower redshift. This is generally

consistent with observations showing that the broad-band SEDs and the rest-frame IR/optical/UV spectra of quasars have not significantly evolved over cosmic time (e.g., Mortlock et al. 2011; Barnett et al. 2015), with a few notable exceptions for the IR band (e.g., Jiang et al. 2010).

In §2.1 we describe the X-ray archival data used in Nanni et al. (2017), and their reduction procedure. The data analysis is presented in §2.2, where we also provide a detailed spectral study for those sources with higher photon statistics ($>$ 30 net counts, i.e., background-subtracted, in the 0.5-7.0 keV energy band). In §2.3 we discuss the mean X-ray properties of our sample, and in §2.4 we provide estimates of the optical-X-ray spectral slope. Finally, in §2.5 we give a summary of our results.

Throughout this work we assume $H_0 = 70$ km s^{-1} Mpc^{-1}, $\Omega_\Lambda = 0.7$, and $\Omega_M = 0.3$ (Bennett et al. 2013), and errors are reported at 68% confidence level if not specified otherwise. Upper limits are reported at the 3σ confidence level.

2.1 Sample selection and data reduction

To study the X-ray properties of the population of AGN at high-redshift ($z > 5.5$) we started from the most updated compilation available in 2016 of 198 luminous high-redshift quasars (181 from Bañados 2015 & Bañados et al. 2016; eight from Reed et al. 2017*a*; nine from Yang et al. 2017) and cross-correlated it with all the available archival data from *Chandra*, XMM-*Newton*, and *Swift*-XRT. The majority of these 198 AGN were found with optical and NIR surveys and are classified as Type 1 AGN. From the cross-correlation we found that 29 sources have archival X-ray observations: 21 QSOs have been observed by *Chandra*, while 12 have XMM-*Newton* observations; J0100+2802, J1030+0524, J1120+0641, J1148+5253 and J1148+5251 were observed by both telescopes. One additional source has been observed by *Swift*-XRT with a relatively deep exposure. We also note that a further ten objects fall within *Swift*-XRT fields observed for only ∼5 ks each. We did not consider them in our work, as no useful constraints can be derived on their X-ray properties. None of these 29 sources come from either the Chandra Deep Field North (Xue et al. 2016) or South (Luo et al. 2017) or from the COSMOS survey (Civano et al. 2016). These three deep fields have no sources with spectroscopic redshift above 5.5 (see Vito et al. 2013 and Vito et al. 2016 for the Chandra Deep Fields, and Marchesi et al. 2016 for the COSMOS survey). More generally, there are no X-ray selected sources with spectroscopic redshift > 5.5.

We reprocessed all the 21 *Chandra* sources using the *Chandra* software CIAO v. 4.8 with *faint* or *vfaint* mode for the event telemetry format according to the corresponding observation. Data analysis was carried out using only the events with ASCA grades 0, 2, 3, 4 and 6. We extracted the number of counts from

circular regions centered at the optical position of every source. We used a radius of 2", corresponding to 95% of the encircled energy fraction (EEF) at 1.5 keV for the on-axis cases ($\theta < 1$'), and of 10" for the off-axis extractions, corresponding to at least 90% of the EEF at 1.5 keV. Fifteen of the 21 *Chandra* QSOs were the targets of the X-ray observations, while the other six were serendipitously observed at large off-axis angles ($\theta > 1$'). The background spectra were extracted from adjacent circular regions, free of sources, with an area ten times larger. In order to assess if a source could be considered detected in the X-ray band we computed the Poisson probability (P_P) of reproducing a number of counts equal to or above the value extracted in the source region (in the 0.5-7.0 keV energy range) given the background counts expected in the source area. We considered as detected those sources showing a detection probability of $> 99.7\%$ ($> 3\sigma$). We found that the 15 on-axis QSOs are detected ($P_P > 3\sigma$) in the 0.5-7.0 keV band. One of the six off-axis sources (RD J1148+5253) is also detected in the X-ray band with low-statistics ($\sim$3 counts; see §3.2 of Gallerani et al. 2017*b* for detailed investigation of the detection significance) so, in the end, we found that 16 out of 21 sources (including J1148+5253) are detected.

The XMM EPIC data were processed using the Science Analysis Software (SAS v. 15) and filtered for high-background time intervals; for each observation and camera we extracted the 10-12 keV light curves and filtered out the time intervals where the light curve was 3σ above the mean. For the scientific analysis we considered only events corresponding to patterns 0-12 and patterns 0-4 for the MOS1/2 and pn, respectively. Because of the higher background level of XMM, we extracted the counts from circular regions centered at the optical position of the QSOs with radius of 10" for on-axis sources, corresponding to 55% of EEF at 1.5 keV, and of 30" for off-axis positions, corresponding to at least 40% of the EEF at 1.5 keV. The background was extracted using the same approach adopted for *Chandra* data. We then computed the Poisson detection probability, as we did for the *Chandra* quasars, for all the sources. In this case we found that the five on-axis sources (the targets of the corresponding observations) were detected in the X-ray band at $> 3\sigma$, while seven sources were observed with large off-axis angles and are undetected in the X-ray band (they were observed serendipitously).

For the source observed by *Swift*-XRT, data reduction and spectrum extraction were performed using the standard software (HEADAS software v. 6.18) and following the procedures described in the instrument user guide.[1] Given the limited number of photons, in order to optimize the ratio between signal and background we restricted our analysis to a circular region of 10" radius, including $\sim$50% of the flux according to the instrumental point spread function (PSF) full width half maximum (FWHM) (Moretti et al. 2005). The ancillary response file (ARF) has

[1] http://heasarc.nasa.gov/docs/swift/analysis/documentation

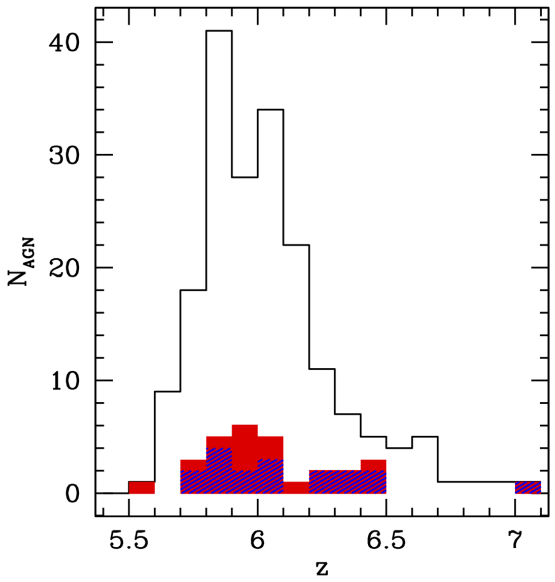

Figure 2.1: Redshift distribution of the 198 known QSOs at $z > 5.5$ (black histogram) and of the 29 QSOs observed in the X-rays (red shaded histogram). The blue shaded histogram shows the distribution of the 18 sources detected at $> 3\sigma$.

been calculated accordingly by the *xrtmkarf* task. In Table 2.1 we report all the information linked to the X-ray observations of the 29 QSOs. We show in Fig. 2.1 the redshift distribution of all the 198 QSOs known at $z > 5.5$ (black histogram) and the distribution of those observed in the X-rays (red shaded histogram), and discussed in Nanni et al. (2017). The blue shaded histogram shows the redshift distribution of the 18 QSOs detected. We display the X-ray cutouts of the 18 detected sources in Fig. 2.2.

2.2 X-ray data analysis

In Table 2.2 we present the number of counts in the total (0.5-7.0 keV), soft (0.5-2.0 keV), and hard (2.0-7.0 keV) bands for all the sources; for the undetected QSOs we provide upper limits to the number of counts at the 3σ confidence level. For *Chandra* sources, these upper limits were computed using the *srcflux* tool of CIAO, that extracts source and background counts from a circular region, centered at the source position, that contains 90% of the PSF at 1 keV. For the XMM undetected sources we used the *sosta* command of the XIMAGE software, extracting source and background counts from circular regions with radius r=10" and r=30", respectively. Table 2.2 also includes the hardness ratio (HR), computed as $HR = \frac{H-S}{H+S}$ where H and S are the net counts in the hard (2-7 keV) and soft (0.5-2.0 keV)

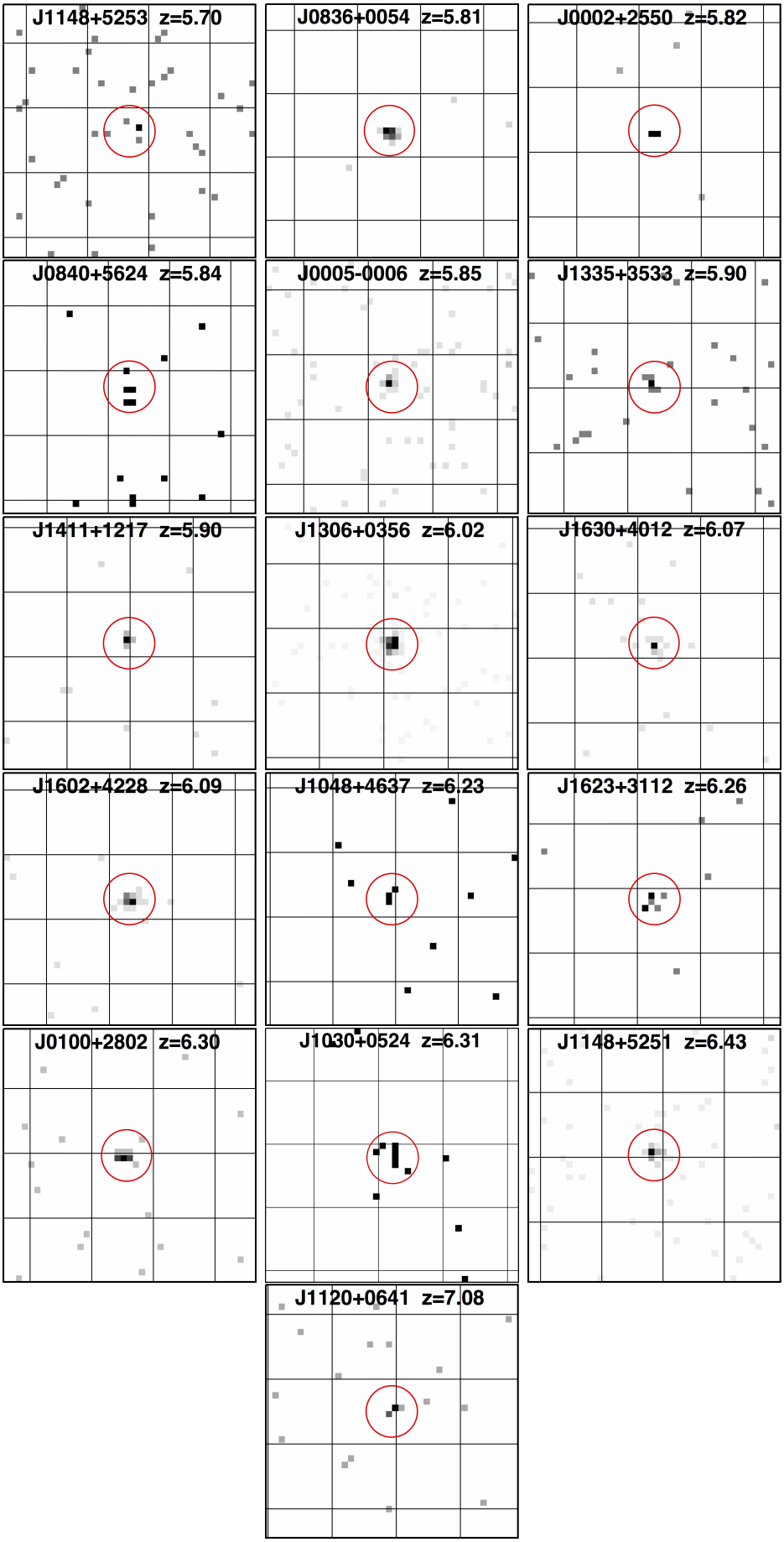

Figure 2.2: Continues on the next page.

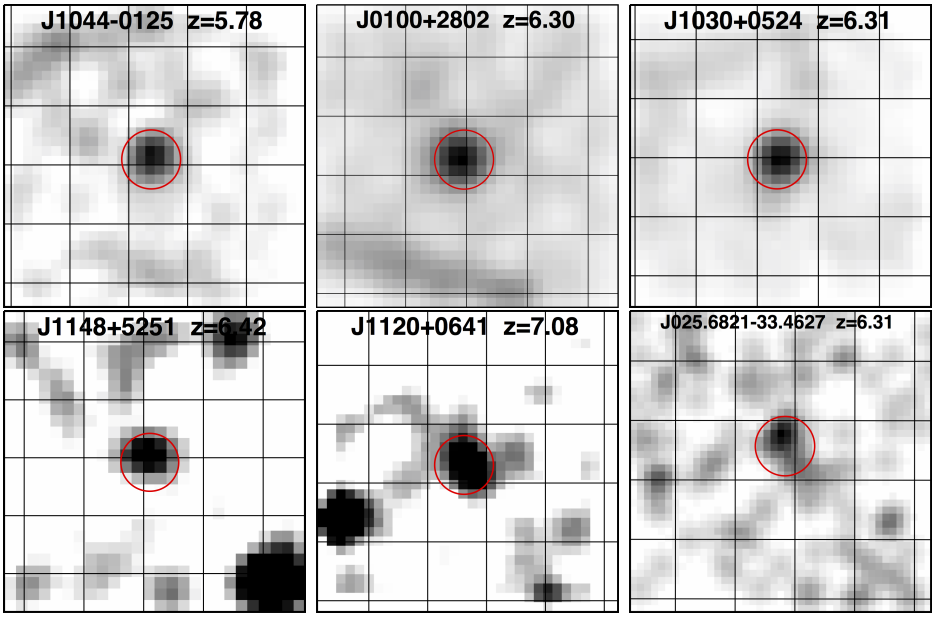

Figure 2.2: Full-band (0.5-7 keV) cutouts of the 18 detected sources (the first 16 images from *Chandra*, the following five from XMM and the last one from *Swift*). The XMM images are obtained summing data from the three detectors (pn, MOS1, MOS2). Red circles represent our extraction regions (2" and 10" radius for *Chandra* and XMM/*Swift*, respectively). The grid separations are 5" and 20" for *Chandra* and XMM/*Swift* QSOs, respectively. Each panel spans 20"x20" and 100"x100" on the sky for *Chandra* and XMM/*Swift* QSOs, respectively. For clarity the XMM/*Swift* images have been smoothed with a three pixel radius Gaussian function. The XMM cutout of J1148+5251 is shown in the 0.2-12 keV band.

Table 2.1
X-ray observations log for $z > 5.5$ quasars with X-ray data

Object	z	R.A.	Decl.	C/X[a]	X-ray obs. date C/X	Chip-id C[b]	t_{exp} C/X[c] [ks]	θ C/X[d] [arcmin]	N_H^g [10^{20} cm^{-2}]	Ref.[h]
NDWFS J142729.7+352209.0	5.53	14:27:29.70	+35:22:09.00	C	2004 Mar 31	AI(1)	4.7	7.9	1.3	...
RD J114816.2+525339.3†	5.70	11:48:16.21	+52:53:39.30	C/X	2015 Sep 2/2004 Nov 4	AS(7)	77.8/3.8	1.8/1.5	1.5	1/...
SDSS J012958.5−003539.7‡	5.78	01:29:58.51	−00:35:39.70	X	2015 Jan 27	...	1.7	15.7	3.0	...
SDSS J104433.0−012502.2†	5.78	10:44:33.04	−01:25:02.20	X	2000 May 28	...	31.5	0.0	4.1	2/3
SDSS J083643.8+005453.2	5.81	08:36:43.86	+00:54:53.26	C	2002 Jan 29	AS(7)	5.7	0.6	4.4	2/...
SDSS J000239.4+255034.9	5.82	00:02:39.39	+25:50:34.96	C	2005 Jan 24	AS(7)	5.9	0.6	3.2	4/...
SDSS J084035.1+562420.2‡	5.84	08:40:35.10	+56:24:20.22	C	2005 Feb 3	AS(7)	15.8.	0.6	4.2	4/...
SDSS J000552.3−000655.8◇	5.85	00:05:52.34	−00:06:55.80	C	2005 Jul 28	AS(7)	16.9	0.6	3.0	4/...
NDWFS J142516.3+325409.3	5.89	14:25:16.33	+32:54:09.54	C	2003 Mas 26	AI(0)	4.7	3.2	1.0	...
SDSS J133550.8+353315.8‡	5.90	13:35:50.81	+35:33:15.82	C	2008 Mar 10	AS(7)	23.5	0.3	1.0	...
SDSS J141111.3+121737.3	5.90	14:11:11.29	+12:17:37.28	C	2005 Mar 17	AS(7)	14.3	0.6	1.8	4/...
PSO J328.7339−09.5076	5.92	21:54:56.16	−09:30:27.46	X	2004 Nov 1	...	23.5	8.2	3.8	...
SDSS J205321.8+004706.8‡	5.92	20:53:21.77	+00:47:06.80	C	2014 Dec 20	AI(0)	9.9	8.6	4.0	...
ULAS J014837.6+060020.1†	5.98	01:48:37.64	+06:00:20.06	X	2002 Jul 14	...	9.3	7.6	4.7	...
PSO J007.0273+04.9571‡	5.99	00:28:06.56	+04:57:25.64	C	2001 Dec 7	AS(6)	66.4	8.3	2.9	...
CFHQS J021627.8−045534.1	6.01	02:16:27.81	−04:55:34.10	X	2002 Aug 12	...	33.1	4.5	2.0	...
SDSS J130608.3+035626.4	6.02	13:06:08.27	+03:56:26.36	C	2004 Dec 11	AS(7)	118.2	1.0	2.0	2/...
" [e]	6.02	13:06:08.27	+03:56:26.36	C	2002 Feb 5	AS(7)	8.2	0.6	2.0	2/...
SDSS J163033.9+401209.7	6.07	16:30:33.90	+40:12:09.69	C	2005 Nov 4	AS(7)	27.4	0.1	1.0	4/...
SDSS J030331.4−001912.9◇	6.08	03:03:31.40	−00:19:12.90	C	2011 Nov 27	AS(7)	1.5	4.8	6.9	...
SDSS J160253.9+422824.9	6.09	16:02:53.98	+42:28:24.94	C	2005 Oct 29	AS(7)	13.2	0.2	1.2	4/...
HSC J221644.5−001650.1†	6.10	22:16:44.47	−00:16:50.10	X	2011 Dec 7	...	3.7	13.9	4.9	...
SDSS J104845.1+463718.6†	6.23	10:48:45.07	+46:37:18.55	C	2005 Jan 10	AS(7)	15.0	0.6	1.4	4/...
SDSS J162331.8+311200.5	6.26	16:23:31.81	+31:12:00.53	C	2004 Dec 29	AS(7)	17.2	0.6	1.8	4/...
SDSS J010013.0+280225.9‡	6.30	01:00:13.02	+28:02:25.92	C/X	2015 Oct 16/2016 Jun 29	AS(7)	14.8/46.3	0.3/0.0	5.8	5/...
ATLAS J025.6821−33.4627	6.31	01:42:43.73	−33:27:45.47	S	2007 Sep 11 & 2007 Oct 3	...	193.6 [f]	4.7 [f]	4.3	...
SDSS J103027.1+052455.1	6.31	10:30:27.11	+05:24:55.06	C/X	2002 Jan 29/2003 May 22	AS(7)	8.0/51.1	0.6/0.0	2.6	2/6
SDSS J114816.7+525150.4	6.42	11:48:16.65	+52:51:50.39	C/X	2015 Sep 2/2004 Nov 4	AS(7)	77.8/3.8	0.3/0.0	1.5	1/...
CFHQS J021013.2−045620.9	6.43	02:10:13.19	−04:56:20.90	X	2012 Jul 10	...	5.0	6.3	1.9	...
ULAS J112001.5+064124.3	7.08	11:20:01.48	+06:41:24.30	C/X	2011 Feb 4/2012 May 23	AS(7)	15.8/183.6	0.3/0.0	5.1	.../7,8

Notes - For the XMM exposure time and off-axis angle we provide only the information about the EPIC pn camera.

(a) Public data from *Chandra* (C) and/or XMM (X) or *Swift*-XRT (S).

(b) *Chandra* chip identification in which the source is observed. AI stands for ACIS-I (the aimpoint is on the chip ID 3) and AS stands for ACIS-S (the aimpoint is on the chip ID 7).

(c) Exposure time filtered from high-energy time intervals after flare removal.

(d) Off-axis angle of the source.

(e) J1306+0356 has two data-sets taken from two different observations.

(f) This information refers to *Swift*-XRT observations.

(g) Galactic column density calculated using the *nh* FTOOL (N_H values from Kalberla et al. 2005).

(h) References for objects previously published in X-rays: (1) Gallerani et al. (2017*b*); (2) Brandt et al. (2002); (3) Brandt et al. (2001); (4) Shemmer et al. (2006); (5) Ai et al. (2016); (6) Farrah et al. (2004); (7) Moretti et al. (2014); (8) Page et al. (2014);.

† BALQs; ‡ WLQs; ◇ Weak-IR QSOs found in the literature. See §2.4.2.

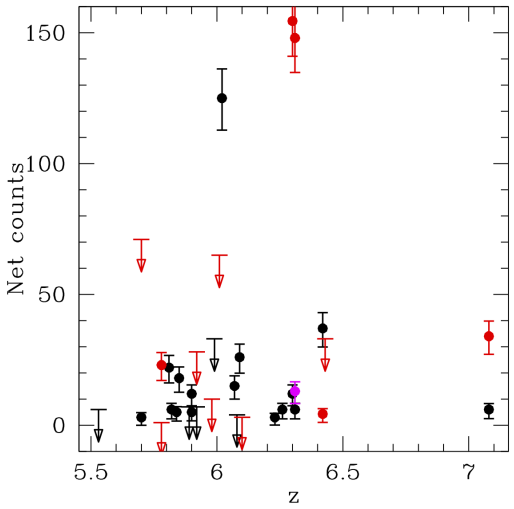

Figure 2.3: Net counts vs. redshift. Black points represent the 21 QSOs observed with *Chandra*, red points indicate the 12 QSOs observed with XMM (five sources are in common with *Chandra*) and the magenta point represents the QSO observed with *Swift*-XRT. Detected sources are shown as full dots, while arrows represent 3σ upper limits.

bands, respectively. In Fig. 2.3 we report the redshift distribution of the net counts from all sources; upper limits correspond to undetected QSOs. It is evident that the majority of the detected sources have < 30 net counts.
For the 12 sources with > 10 counts we attempted an X-ray spectral fit, while we use the tool PIMMS for those QSOs detected with < 10 net counts and those undetected in order to derive the basic X-ray properties. We "grouped" the spectra ensuring a minimum of one count for each bin, and the best fit was calculated using the Cash statistic[2], except for J1306+0356 for which we used a grouping of 20 counts per bin and the χ^2 statistic because of its large number of net counts ($\sim$125). We modeled these spectra with an absorbed power-law, using XSPEC v. 12.9 (Arnaud 1996). The absorption term takes into account both the Galactic absorption (shown in Table 2.1) and the source intrinsic obscuration. In the fit we fixed the value of the photon index to $\Gamma = 1.9$, which is a typical value found for Type 1 AGN at lower redshift (e.g., Piconcelli et al. 2005). We list in Table 2.3 the basic parameters derived from spectral fits. Errors are reported at 90% confidence level if not specified otherwise.

We also fit the five spectra of the sources with highest counting statistics (> 30 net counts) using the same model described above but with Γ free to vary. We

[2]With a binning of one count for each bin the empty channels are avoided and so the C-stat value is independent of the number of counts. Consequently, the distribution of the C-stat/d.o.f. is centered at $\sim$1. See Appendix A of Lanzuisi et al. (2013).

present these results in the next sub-section.

2.2.1 Analysis of the five QSOs with the best photon statistics

In this section we show the results obtained from our analysis of the five quasars with the best counting statistics (> 30 net counts): J0100+2802, J1030+0524, J1120+0641, J1148+5253 and J1306+0356. In all the fit models we included a Galactic-absorption component, which was kept fixed during the fit.

SDSS J1306+0356 ($z = 6.02$). This is the only quasar detected by *Chandra* with more than 100 net counts in the 0.5-7.0 keV band. The target was observed in two different periods and has two different data-sets. In order to improve the fit quality we combined the two data-sets obtaining a spectrum with ∼125 net counts. In the fit we used a grouping of 20 counts per bin in order to use the χ^2 statistic and we were able to fit its spectrum with a model in which the photon index Γ was left free to vary. We fit the spectrum with a power-law model at the redshift of the quasar. The spectrum and its best-fit model and residuals are shown in Fig. 2.4 (a). Throughout the chapter, residuals are in terms of sigmas with error bars of size one. In the case of the Cash statistic, they are defined as the (data−model)/error, where error is calculated as the square root of the model predicted number of counts. The best fit photon index is $\Gamma = 1.72^{+0.53}_{-0.52}$ with $\chi^2 = 2.2$ for 3 degrees of freedom. Such a value of Γ is consistent with the others found for luminous AGN at lower redshift ($1 \leq z \leq 5.5$; e.g., Vignali et al. 2005; Shemmer et al. 2006; Just et al. 2007). We then added an absorption component at the redshift of the quasar and obtained an upper limit of $N_H < 2.2 \times 10^{23}$ cm^{-2}.

SDSS J1030+0524 ($z = 6.31$). This quasar was observed by both *Chandra* and XMM. The short *Chandra* exposure detected this source with ∼6 net counts, while the much longer XMM observation (see Table 2.1) detected this source with ∼148 net counts. We used a grouping of 1 count for each bin for all spectra of the three cameras and we fit the three EPIC spectra (pn, MOS1 and MOS2) with a power-law model and an intrinsic-absorption component at the redshift of the quasar. The spectrum and its best-fit model and residuals are shown in Fig. 2.4 (b). The best-fit photon index is $\Gamma = 2.39^{+0.55}_{-0.46}$ with C-stat = 21.6 for 18 degrees of freedom. This value of Γ is consistent with the one found by Farrah et al. (2004; $\Gamma = 2.27^{+0.31}_{-0.31}$). We also found an upper limit to the column density $N_H < 1.9 \times 10^{23}$ cm^{-2}.

SDSS J1148+5251 ($z = 6.42$). This quasar was observed by both observatories; *Chandra* detected this source with ∼37 net counts, thus allowing us to fit its data. We used a grouping of 1 count for each bin, and we fit the spectrum with a simple

power-law model. The spectrum and its best-fit model and residuals are shown in Fig. 2.4 (c). The best-fit photon index is $\Gamma = 1.59^{+0.61}_{-0.57}$ with C-stat = 20.9 for 33 degrees of freedom. This value of Γ is consistent with the one found by Gallerani et al. (2017; $\Gamma = 1.6^{+0.49}_{-0.49}$).

SDSS J0100+2802 ($z = 6.30$). This is the latest quasar observed by both *Chandra* and XMM. The *Chandra* exposure detected this source with ∼12 net counts, while a total of ∼155 net counts were collected by XMM. Fitting a power-law to the *Chandra* spectrum, we obtained $\Gamma = 3.0^{+1.2}_{-0.8}$ which is consistent with the one found by Ai et al. (2016; $\Gamma = 3.03^{+0.78}_{-0.70}$), but this measurement is uncertain with very large errors. For the XMM spectrum, we used a grouping of 1 count for each bin for all spectra of the three cameras and we fit the three EPIC spectra (pn, MOS1 and MOS2) with a power-law model and an intrinsic-absorption component at the redshift of the quasar. The spectrum and its best-fit model and residuals are shown in Fig. 2.4 (d). The best-fit photon index is $\Gamma = 2.33^{+0.32}_{-0.29}$ with C-stat = 233.5 for 254 degrees of freedom. This value of Γ is consistent with the one found by Ai et al. (2016) and the one we derived from the *Chandra* analysis, but is less uncertain. We also found an upper limit to the column density $N_H < 2.1 \times 10^{23}$ cm^{-2}.

ULAS J1120+0641 ($z = 7.08$). This is another quasar observed by both *Chandra* and XMM (which observed it in three different orbits). We summed together the six MOS and the three pn spectra and then we summed the two combined MOS, so as to increase the fit quality, and used a binning of 1 count per bin. *Chandra* detected this source with ∼6 net counts and we were not able to fit its data, while XMM detected this source with ∼34 net counts. We fit the two EPIC spectra with a power-law model and compared our result with those available in the literature (Moretti et al. 2014; Page et al. 2014). The spectrum and its best-fit model and residuals are shown in Fig. 2.4 (e). The best-fit photon index is $\Gamma = 2.24^{+0.55}_{-0.48}$ with C-stat = 391.1 for 364 degrees of freedom. Such a value of Γ is half way between those found by Page et al. (2014; $\Gamma = 2.64^{+0.61}_{-0.54}$) and Moretti et al. (2014; $\Gamma = 1.98^{+0.46}_{-0.43}$) and consistent with both of them within the errors.

2.3 Mean X-ray properties of the most distant quasars

Obtaining accurate values of the X-ray spectral properties, such as the power-law photon index and the intrinsic absorption column density, for most individual sources in this work is hindered by the small numbers of detected photons. To date, only five QSOs at $z > 5.5$ (the five presented in §2.4) have sufficient counting statistics that allow accurate measurements of the X-ray spectral properties (Far-

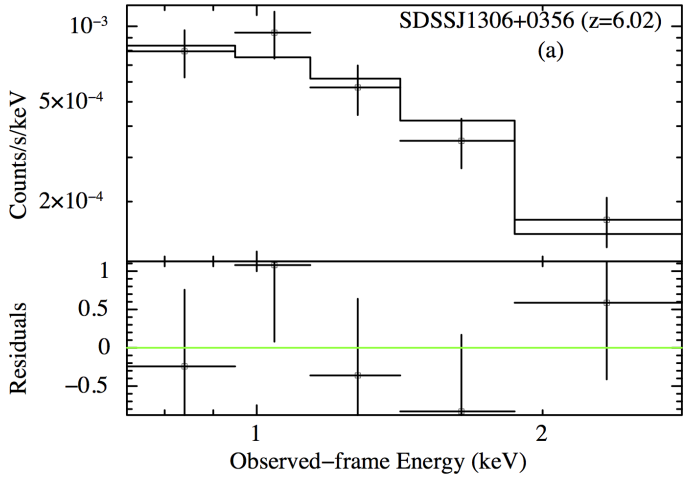
SDSSJ1306+0356 (z=6.02)
(a)
Counts/s/keV
Residuals
Observed−frame Energy (keV)

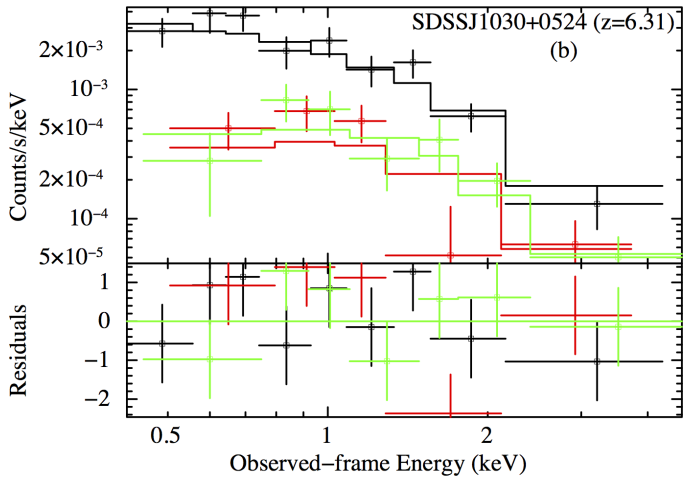
SDSSJ1030+0524 (z=6.31)
(b)
Counts/s/keV
Residuals
Observed−frame Energy (keV)

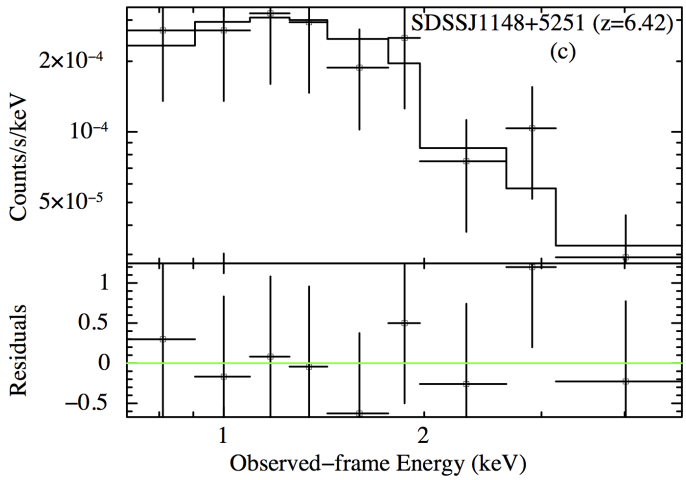
SDSSJ1148+5251 (z=6.42)
(c)
Counts/s/keV
Residuals
Observed−frame Energy (keV)

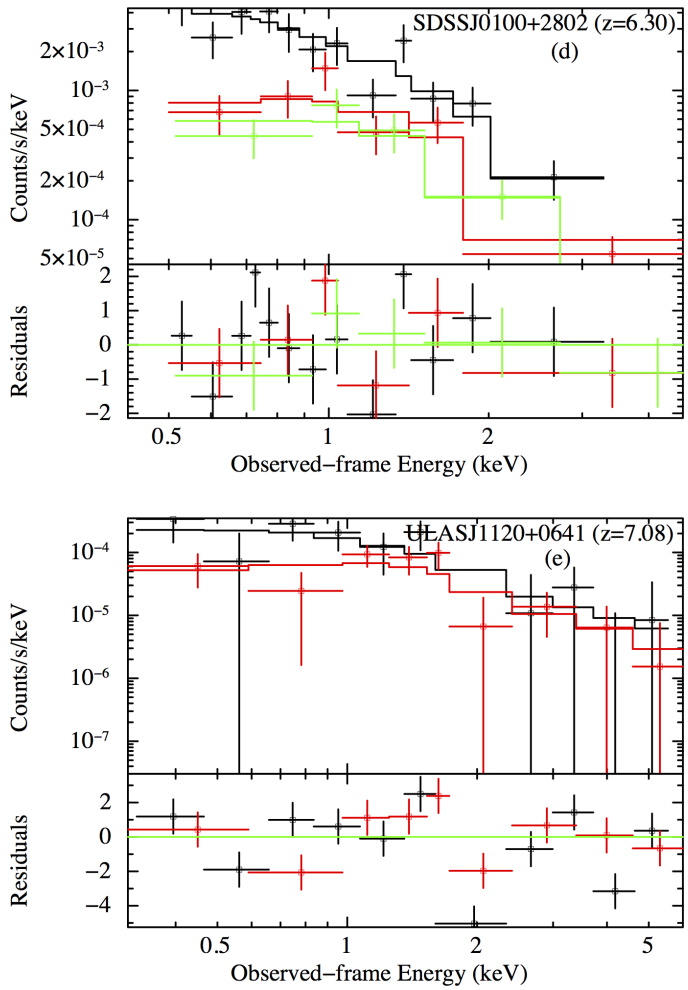

Figure 2.4: Spectra of the five AGN with the best counting statistics (34 $\leq$ net counts $\leq$ 148). Spectra in panels *a* and *c* are extracted from *Chandra*, while spectra in panels *b*, *d* and *e* are from XMM-*Newton*. The *a*, *b* and *d* spectra are fit by a power-law model with Galactic and intrinsic absorption; the *c* and *e* spectra are fit by a simple power-law model plus Galactic absorption. The black, red, and green points and lines in the *b* and *d* panels correspond to pn, MOS1, and MOS2, respectively. The black and red points and lines in the *e* panel correspond to pn and combined MOS1 and MOS2, respectively. For the sake of clarity, we display the spectra using a minimum binning of 20, 15, 3, 3 and 20 counts for each bin for J0100+2802, J1030+0524, J1120+0641, J1148+5251 and J1306+0356, respectively.

rah et al. 2004; Moretti et al. 2014; Page et al. 2014; Gallerani et al. 2017*b*). Our knowledge of the X-ray spectral properties of quasars at $z > 5.5$ therefore relies mainly on the joint spectral fitting of samples of these sources (Vignali et al. 2005; Shemmer et al. 2006; Just et al. 2007). We first selected the 16 quasars detected by *Chandra* and made a joint spectral fitting analysis using 15 QSOs, excluding the data-set with ∼100 net counts of J1306+0356 (but keeping its data-set with more

limited statistics) and the spectrum of J1148+5251 due to their relatively high statistics (> 30 net counts). In all fits we used the Cash statistic and the errors are reported at the 90% confidence level. We fit these 15 spectra with a power-law model and associated its value of redshift and Galactic absorption to each source. We found a mean photon index $\Gamma = 1.93^{+0.30}_{-0.29}$ (C-stat = 223.1 for 151 d.o.f.), which is consistent with those found in previous works. As a further test, we stacked all the *Chandra* spectra from the detected sources with similar redshift, obtaining two combined spectra, one from sources with $5.7 \leq z \leq 6.1$ (10 QSOs) and one from sources with $6.2 \leq z \leq 6.5$ (5 QSOs), excluding the spectrum of J1120+0641 from the sum, because of its very high redshift, and the data-set of J1306+0356 with a high number of counts. This separation into two redshift bins limits errors caused by summing spectral channels that correspond to different rest-frame energies.

The lower-redshift stack has an average redshift of $z = 5.92$ and 130 net counts. The one at higher redshift has an average redshift of $z = 6.30$ and 66 net counts. We used XSPEC to fit the two spectra with a simple power-law[3] and derived a mean photon index of $\Gamma = 1.92^{+0.28}_{-0.27}$ (C-stat = 48.3 for 91 d.o.f.) for the lower redshift spectrum (Fig. 2.5, top panel). This value is consistent with the mean photon indices obtained by jointly fitting spectra of luminous and unobscured quasars at lower redshift ($1 \leq z \leq 5.5$; e.g., Vignali et al. 2005; Shemmer et al. 2006; Just et al. 2007) and is also consistent with the values predicted by theory (the power-law spectrum is produced by inverse Compton processes caused by interaction of hot-corona electrons with optical/UV photons from the accretion disk; typical values are $\Gamma \sim 1.8 - 2.1$; Haardt & Maraschi 1991; Haardt & Maraschi 1993). In Fig. 2.5 (bottom panel) we report the mean photon indices for QSO samples at different redshifts derived from joint fitting or stacking analysis. We did not find any significant evolution of the AGN photon index with redshift up to $z \sim 6$ and the only two values measured at higher redshift (J1030+0524 at $z = 6.31$ by Farrah et al. 2004 and J1120+0641 at $z = 7.08$ by Moretti et al. 2014) are consistent with this non evolutionary trend.

We note that, at $z \sim 6$, we are sampling rest frame energies in the range 3.5-49 keV. In this band, a hardening of AGN spectra is often observed because of the so called "Compton-reflection hump", that is, radiation from the hot corona that is reprocessed by the accretion disk, which peaks at ∼30 keV. However, the mean photon index we derived does not differ from the typical value of Type 1 AGN, suggesting that the presence of the Compton-reflection component is not significant in our sample, as indeed is observed for luminous QSOs (e.g., Page et al. 2005; Shemmer et al. 2008). The individual photon indices we derived in §2.4 for the five sources with > 30 net counts are also consistent with typical values of

[3]In these cases we included a Galactic absorption component, which was kept fixed at a mean N_H value during the fit.

luminous unobscured QSOs, again suggesting negligible Compton reflection. For the higher-redshift spectrum we obtained a photon index with poorer constraints than the previous one, $\Gamma = 1.73^{+0.43}_{-0.40}$ (C-stat = 51.0 for 55 d.o.f.), because of the smaller number of counts. This spectrum is characterized by a flatter power-law slope due to the presence of J1148+5251, that has a flatter photon index (see Gallerani et al. 2017*b*). However, this value is still consistent, within the errors, with those present in the literature. Then we fit the two spectra with an absorbed power-law model and Γ frozen to 1.9. We found that $N_H \leq 8.9 \times 10^{22}$ cm^{-2} for the former spectrum and $N_H \leq 5.0 \times 10^{23}$ cm^{-2} for the latter spectrum. The limits on the mean column densities are consistent with the values found in the literature and indicate that the population of $z > 5.5$ luminous QSOs is not significantly obscured, as expected according to their optical and NIR classification. Finally, we combined all the spectra used in the two stacking analyses, excluding J1148+5251, and fit them with a power-law model, obtaining a spectrum with 157 net counts and with $\Gamma = 1.83^{+0.25}_{-0.24}$ (C-stat = 62.7 for 108 d.o.f.), fully consistent with the values previously reported.

2.4 X-ray and optical properties of the sample

In Table 2.3 we provide all the X-ray properties we derived as well as all the optical information available in the literature for our sample. The details of the Table columns are provided below.

Column (1). - The name of the quasar taken from Bañados (2015) and Bañados et al. (2016).

Column (2). - The monochromatic apparent AB magnitude at the rest-frame wavelength $\lambda = 1450$ Å taken from Bañados (2015).

Column (3). - The absolute magnitude at the rest-frame wavelength $\lambda = 1450$ Å and computed from m_{1450}.

Column (4). - The monochromatic luminosity at a rest-frame wavelength of 2500 Å , computed from the magnitudes in column (2), assuming a UV-optical power-law slope of $\alpha = -0.5$ (e.g., Vignali et al. (2005); Shemmer et al. (2006); Just et al. (2007);).

Column (5). - The Galactic absorption-corrected flux in the observed-frame 0.5-2.0 keV band. Fluxes were computed using XSPEC for detected sources with > 10 net counts and using PIMMS[4] for QSOs with < 10 net counts and for those

[4]For each *Chandra* observation we set the response to that of the corresponding observing

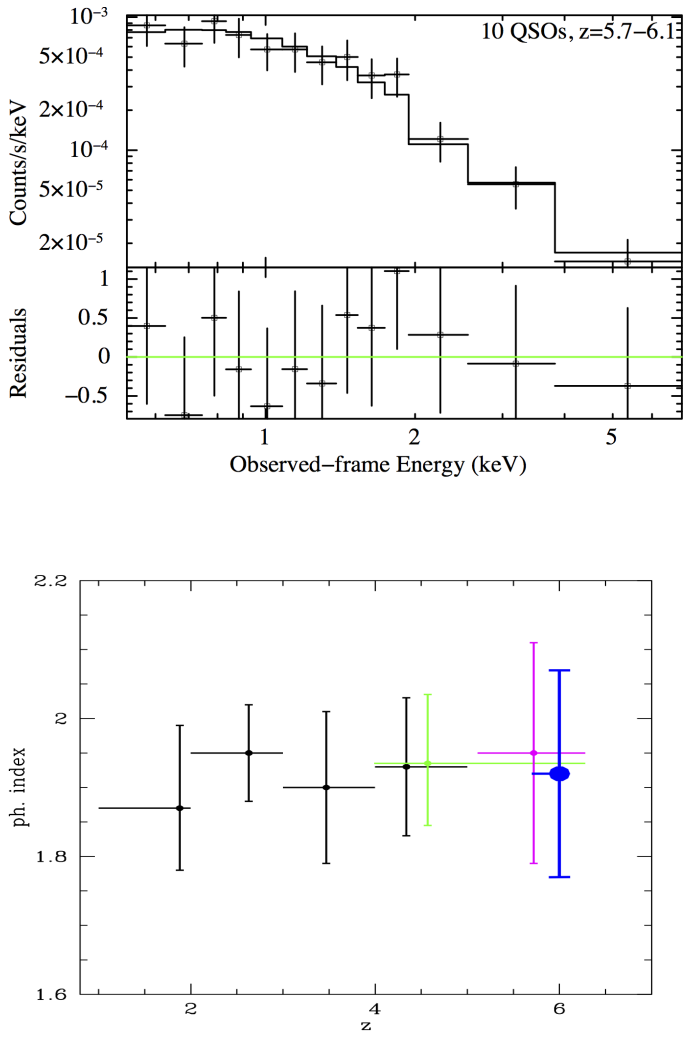

Figure 2.5: *Top panel*: stacked spectrum of the ten QSOs with $5.7 \leq z \leq 6.1$ fit with a power-law model and residuals (data−model). For clarity we adopted a minimum binning of ten counts per bin. *Bottom panel*: photon index vs. redshift. Black, green, and magenta points are the results of the Just et al. (2007), Vignali et al. (2005), and Shemmer et al. (2006) stacking analyses, respectively. The blue point is the photon index of the stacked spectrum shown in the top panel. In all cases the assumed model is a simple power-law and errors are reported at the 68% confidence level.

undetected (assuming a power-law with $\Gamma = 1.9$). Upper limits are at the 3σ level.

Column (6). - The luminosity in the rest-frame 2-10 keV band.

Column (7). - The optical-X-ray power-law slope defined as

$$\alpha_{ox} = \frac{log(f_{2\,keV}/f_{2500\,\text{Å}})}{log(\nu_{2\,keV}/\nu_{2500\,\text{Å}})}, \tag{2.1}$$

where $f_{2\,keV}$ and $f_{2500\,\text{Å}}$ are the flux densities at rest-frame 2 keV and 2500 Å, respectively. The errors on α_{ox} were computed following the numerical method described in §1.7.3 of Lyons 1991, taking into account the uncertainties in the X-ray counts and an uncertainty of 10% in the 2500 Å flux corresponding to a mean z-magnitude error of ~ 0.1.

Column (8). - Upper limits on the column density derived from the spectral fitting for sources with > 10 net counts with a power-law model with Γ frozen to 1.9.

In Fig. 2.6 we report the 0.5-2.0 keV flux versus apparent magnitude at 1450 Å.

2.4.1 Source variability

The five sources with the highest statistics (§2.4) have been observed with *Chandra* and XMM in different years, so we checked if these QSOs have varied their X-ray fluxes over the passing of time. J0100+2802, J1030+0524, J1120+0641 and J1148+5251 were observed and detected by both X-ray observatories, and we computed the variability significance using the fluxes reported in Table 2.3, while RD J1148+5253 is detected only by *Chandra*. For this source the upper limit on the flux derived from XMM data is above the flux value derived from *Chandra* (see Table 2.3), so there is no clear evidence of variability. Also J1306+0356 was observed at two different epochs by *Chandra* so, in this case, we computed the variability significance using the fluxes derived from the spectral fit of the two data-sets ($f_{0.5-2\,keV} = 2.7^{+0.4}_{-0.3}$ and $f_{0.5-2\,keV} = 4.5^{+1.0}_{-0.5}$ in units of 10^{-15} erg cm^{-2} s^{-1}). All the computed significances are below the 2σ level, so there is no clear evidence of flux variability in these five sources. These results are consistent with those found for lower redshift sources ($4.10 \leq z \leq 4.35$), with comparable X-ray luminosities, and strengthen the idea that the X-ray variability does not increase with redshift (Shemmer et al. 2017).

Cycle to account for the effective area degradation.

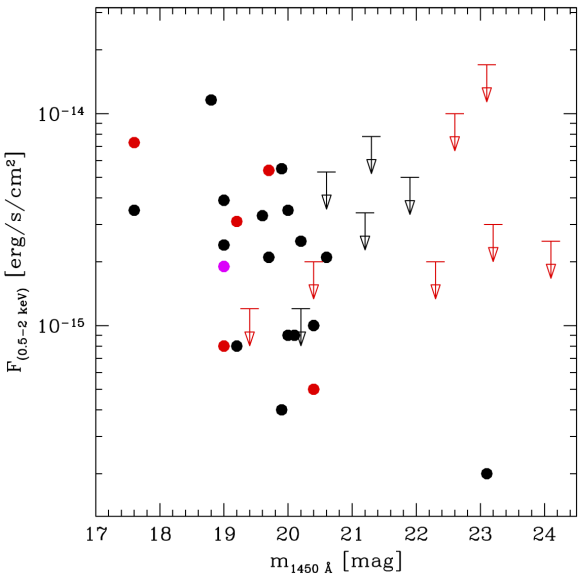

Figure 2.6: 0.5-2 keV flux vs. apparent magnitude at 1450 Å. Black points indicate the 21 QSOs observed with *Chandra*, red points represent the 12 QSOs observed with XMM and the magenta point is the source observed with *Swift*-XRT. Detected QSOs are shown as filled circles while downward-pointing arrows represent 3σ upper limits.

2.4.2 Multi-band information from the literature

QSOs with peculiar multi-band emission properties could be characterized by different emission or accretion processes that can also affect their X-ray spectra. For example, radio-loud AGN usually have X-ray spectra flatter than radio-quiet QSOs, because of the contribution from the jet (e.g., Wu et al. 2013). Thus, we checked if there are any peculiar QSOs in our sample that also have peculiar X-ray properties linked to their different nature. First, we checked the VLA FIRST catalog (White et al. 1997) and the literature to derive information about the radio loudness (RL) of our sources, adopting the definition by Kellermann et al. (1989): $RL = f_{\nu,5\,GHz}/f_{\nu,4400\,Å}$, where $f_{\nu,5\,GHz}$ is the flux density at a rest-frame frequency of 5 GHz and $f_{\nu,4400\,Å}$ is the flux density at a rest-frame wavelength of 4400 Å, and a quasar is considered radio loud if RL > 100. Assuming an average optical spectral index of $\alpha = -0.5$, we extrapolated the optical rest-frame flux density at 4400 Å from the *WISE* W_1 ($\lambda \sim 3.4\ \mu m$) magnitude, when available, or from m_{1450} otherwise. Twenty-five sources have upper limits on their radio fluxes, two have not been observed by VLA (J328.7339-09.5076 and J025.6821-33.4627) and two (J083643.8+005453.2 and J010013.0+280225.9) are detected with a RL $\sim$12 and $\sim$0.3, respectively. The first value is consistent with the one derived by Bañados (2015) and indicates a moderate level of radio emission that is not supposed

to significantly affect its X-ray spectrum (but see Miller et al. 2011). The two VLA-unobserved sources are also not observed by NVSS. Summarizing, from the values of the derived RL parameters, we found that there are no clear indications of the presence of extreme Radio Loud QSOs in our sample. We also checked in the literature for the presence of any Broad Absorption Line (BALQ), Weak-Line (WLQ) or Weak Infrared QSOs (sources with a weak emission at $\sim$10 μm rest-frame due to a possible lack of torus emission component; Jiang et al. 2010). In our sample five QSOs are classified as BALQs, six as WLQs and two as Weak-IR QSOs (see Table 2.1). WLQs are defined as quasars having rest-frame equivalent widths (EWs) of < 15.4 Å for the Lyα+N V emission-line complex (Diamond-Stanic et al. 2009). This could be due to either an extremely high accretion rate, that may result in a relatively narrow UV-peaked SED (Luo et al. 2015) in which prominent high-ionization emission lines are suppressed (the so called Baldwin effect; Baldwin 1977), or a significant deficit of line-emitting gas in the broad-emission line region (Shemmer et al. 2010). In our case the WLQ X-ray properties are consistent with those of non WLQs (see Table 2.3).

2.4.3 Comparison of the optical properties with lower redshift quasars

The optical-X-ray power-law slope (α_{ox}), defined in Equation 2.1 in §2.4, is expected to trace the relative importance of the disk versus corona. Previous works have shown that there is a significant correlation between α_{ox} and the monochromatic $L_{2500\,\text{Å}}$ (α_{ox} decreases as $L_{2500\,\text{Å}}$ increases; Steffen et al. 2006; Lusso & Risaliti 2017), whereas the apparent dependence of α_{ox} on redshift can be explained by a selection bias (Zamorani et al. 1981; Vignali et al. 2003; Steffen et al. 2006; Shemmer et al. 2006; Just et al. 2007; Lusso et al. 2010; but see also Kelly et al. 2007). We further examine the $\alpha_{ox} - L_{2500\,\text{Å}}$ relationship adding our sample of 29 high-redshift QSOs to previous measurements of α_{ox}. We have plotted α_{ox} versus $L_{2500\,\text{Å}}$ for all the X-ray quasars of our sample in Fig. 2.7, including 1515 QSOs from lower redshift analyses (X-ray selected: 529 from Lusso et al. 2010, 174 from Marchese et al. 2012; optically selected: 743 from Lusso & Risaliti 2016, 11 from Vignali et al. 2003, 13 from Vignali et al. 2005, 13 from Shemmer et al. 2006, 32 from Just et al. 2007). We excluded eight sources from the original sample of Shemmer et al. (2006) because they are also present in our sample (our results for these eight sources are consistent with those derived by Shemmer et al. 2006), obtaining a final sample of 1544 QSOs. Our sample follows the correlation between α_{ox} and UV luminosity with no detectable dependence on redshift. We performed linear regression on the data (13 of them have upper limits on α_{ox}) using the ASURV software package (Lavalley et al. 1992), confirming and strengthening the finding

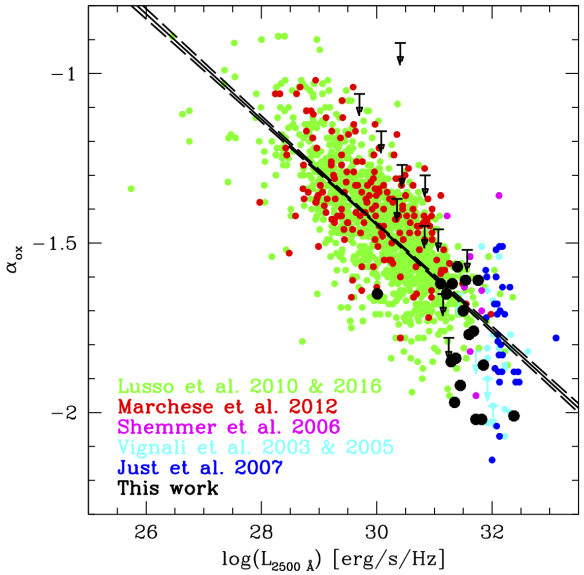

Figure 2.7: α_{ox} versus UV monochromatic luminosity for 1544 QSOs. Black dots correspond to our detected QSO sources, downward-pointing arrows represent undetected sources. Colored points correspond to different literature samples as labeled. The black solid line is the best-fit relation found in our work, while the dashed black lines represent the uncertainty in the relation.

in previous studies that α_{ox} decreases with increasing rest-frame UV luminosity. We found the best-fit relation between α_{ox} and $L_{2500\,\text{Å}}$ to be:

$$\alpha_{ox} = (-0.155 \pm 0.003) log(L_{2500\,\text{Å}}) + (3.206 \pm 0.103). \quad (2.2)$$

Errors are reported at the 1σ confidence level. This correlation is based on the highest number of QSOs available. These best-fit parameters are consistent with those derived by Just et al. (2007) and by Lusso & Risaliti (2017). We note that the presence of our and the Shemmer et al. (2006) samples improves coverage at $z \approx$ 5-6, showing that our analysis supports the idea that luminous AGN SEDs have not significantly evolved out to very high redshift. We also obtained a best-fit relation excluding the X-ray selected data (Lusso et al. 2010 and Marchese et al. 2012) and found that is consistent with Equation 2.2.

2.5 Summary and conclusions

We made a complete and uniform study of the X-ray properties of the most-distant quasars at $z > 5.5$. This is the most up-to-date analysis of the X-ray properties of early AGN. Our main results are the following:

- We started from a parent sample of 198 spectroscopically confirmed QSOs at $z > 5.5$ and considered the 29 objects that have been observed by *Chandra*, XMM-*Newton*, and *Swift*-XRT. Eighteen of them are detected in the X-ray band (0.5-7.0 keV).

- Five sources have sufficient counting statistics (> 30 net counts) to allow us to fit their spectra with a power-law model with Γ free to vary. For these quasars we obtained values of the photon index $\Gamma \sim 1.6-2.4$ consistent with those present in literature (Farrah et al. 2004; Moretti et al. 2014; Gallerani et al. 2017*b*) and those expected from theory (Haardt & Maraschi 1993).

- By performing a spectral stacking analysis we derived the mean photon index of the early AGN population. We divided our 15 *Chandra* detected sources into two redshift bins: $5.7 \leq z \leq 6.1$ (10 sources) and $6.2 \leq z \leq 6.5$ (5 sources). We obtain $\Gamma = 1.92^{+0.28}_{-0.27}$ for the first stacked sub-sample and $\Gamma = 1.73^{+0.43}_{-0.40}$ for the second one. We do not find a significant change in Γ with cosmic time over the redshift range $z \approx 1.0 - 6.4$. Similar results have been recently confirmed also for $z \geq 6$ QSOs (Vito et al. 2019), even if the mean measured photon indices are slightly steeper ($\Gamma = 2.20^{+0.39}_{-0.34}$ and $\Gamma = 2.13^{+0.13}_{-0.13}$ for sources with < 30 and > 30 net counts, respectively). This means that, similarly to optical properties (e.g., Mortlock et al. 2011; Barnett et al. 2015; Bañados et al. 2018), also the X-ray spectral properties of luminous QSOs do not significantly evolve over cosmic time. The upper limits to the mean column density derived from the stacking analysis are $N_H < 8.9 \times 10^{22}$ cm^{-2} for the first sub-sample and $N_H < 5.0 \times 10^{23}$ cm^{-2} for the second one, showing that these luminous high-redshift QSOs are not significantly obscured, as expected from their optical classification as Type 1 AGN.

- Combining our sample with literature works, we confirmed that, by using a statistically larger sample, the α_{ox} parameter depends on UV monochromatic luminosity. The X-ray-to-optical flux ratios of luminous AGN have not significantly evolved up to $z \sim 6$.

Table 2.2
X-ray counts and hardness ratio

Object	X-ray counts *Chandra/XMM*[a]			HR[b]
	0.5−7.0 keV	0.5−2.0 keV	2.0−7.0 keV	
NDWFS J1427+3522	< 6.4	< 5.0	< 1.4	−
RD J1148+5253	$3.3^{+3.0}_{-1.8}$	$0.9^{+2.3}_{-0.8}$	$2.4^{+2.8}_{-1.5}$	$-0.45^{+0.65}_{-0.65}$
" [c]	< 71.3	< 57.9	< 13.4	−
SDSS J0129−0035 [c]	< 1.3	< 1.1	< 0.2	−
SDSS J1044−0125 [c]	$22.9^{+5.9}_{-4.8}$	$19.2^{+5.5}_{-4.4}$	$3.1^{+3.0}_{-1.7}$	$-0.72^{+0.21}_{-0.16}$
SDSS J0836+0054	$21.9^{+5.8}_{-4.7}$	$17.8^{+5.3}_{-4.2}$	$3.0^{+2.9}_{-1.7}$	$-0.71^{+0.22}_{-0.17}$
SDSS J0002+2550	$5.8^{+3.6}_{-2.4}$	$5.8^{+3.6}_{-2.4}$	< 3.0	< -0.32
SDSS J0840+5624	$4.8^{+3.4}_{-2.1}$	$3.8^{+3.1}_{-1.9}$	$1.0^{+2.3}_{-0.9}$	$-0.58^{+0.54}_{-0.46}$
SDSS J0005−0006	$18.4^{+5.4}_{-4.3}$	$16.6^{+5.2}_{-4.0}$	$1.6^{+2.5}_{-1.2}$	$-0.82^{+0.22}_{-0.14}$
NDWFS J1425+3254	< 6.7	< 5.3	< 1.4	−
SDSS J1335+3533	$4.6^{+3.3}_{-2.1}$	$3.8^{+3.1}_{-1.9}$	$0.8^{+2.2}_{-0.7}$	$-0.56^{+0.62}_{-0.52}$
SDSS J1411+1217	$11.9^{+4.6}_{-3.4}$	$9.9^{+4.3}_{-3.1}$	$2.0^{+2.7}_{-1.3}$	$-0.66^{+0.32}_{-0.24}$
PSO J328.7339−09.5076 [c]	< 28.2	< 22.9	< 5.3	−
SDSS J2053+0047	< 6.6	< 4.7	< 1.9	−
ULAS J0148+0600 [c]	< 10.1	< 8.2	< 1.9	−
PSO J007.0273+04.9571	< 33.2	< 28.2	< 5.0	−
CFHQS J0216−0455 [c]	< 65.2	< 53.0	< 12.2	−
SDSS J1306+0356	$125.4^{+12.2}_{-11.2}$	$87.3^{+10.4}_{-9.3}$	$38.1^{+7.2}_{-6.2}$	$-0.39^{+0.09}_{-0.09}$
SDSS J1630+4012	$15.3^{+5.0}_{-3.9}$	$10.8^{+4.4}_{-3.2}$	$4.5^{+3.3}_{-2.1}$	$-0.41^{+0.28}_{-0.27}$
SDSS J0303−0019	< 3.8	< 3.0	< 0.8	−
SDSS J1602+4228	$25.7^{+6.1}_{-5.0}$	$21.8^{+5.7}_{-4.6}$	$3.8^{+3.1}_{-1.9}$	$-0.70^{+0.19}_{-0.15}$
HSC J2216−0016 [c]	< 3.0	< 2.4	< 0.6	−
SDSS J1048+4637	$2.9^{+2.9}_{-1.6}$	$2.9^{+2.9}_{-1.6}$	< 3.0	< 0.02
SDSS J1623+3112	$6.0^{+3.6}_{-2.4}$	$4.0^{+3.2}_{-1.9}$	$2.0^{+2.6}_{-1.3}$	$-0.33^{+0.47}_{-0.48}$
SDSS J0100+2802	$12.0^{+4.6}_{-3.4}$	$10.7^{+4.4}_{-3.2}$	$0.7^{+2.2}_{-0.6}$	$-0.88^{+0.31}_{-0.11}$
" [c]	$154.5^{+13.5}_{-12.4}$	$127.9^{+12.3}_{-11.3}$	$25.8^{+6.1}_{-5.1}$	$-0.66^{+0.07}_{-0.06}$
ATLAS J025.6821−33.4627 [d]	$13.0^{+4.7}_{-3.6}$	$10.4^{+4.3}_{-3.2}$	$1.6^{+2.5}_{-1.2}$	$-0.73^{+0.31}_{-0.22}$
SDSS J1030+0524	$6.0^{+3.6}_{-2.4}$	$6.0^{+3.6}_{-2.4}$	< 3.0	< -0.33
" [c]	$148.0^{+13.2}_{-12.2}$	$128.8^{+12.3}_{-11.3}$	$19.0^{+5.4}_{-4.3}$	$-0.74^{+0.06}_{-0.06}$
SDSS J1148+5251	$36.8^{+7.1}_{-6.0}$	$25.9^{+6.2}_{-5.1}$	$10.9^{+4.4}_{-3.3}$	$-0.41^{+0.17}_{-0.17}$
" [c]	$4.3^{+3.2}_{-2.0}$	$3.1^{+3.0}_{-1.7}$	$1.2^{+2.4}_{-1.0}$	$-0.44^{+0.57}_{-0.57}$
CFHQS J0210−0456 [c]	< 32.8	< 26.7	< 6.1	−
ULAS J1120+0641	$5.7^{+3.5}_{-2.3}$	$4.0^{+3.2}_{-1.9}$	$1.7^{+2.6}_{-1.2}$	$-0.40^{+0.49}_{-0.48}$
" [c]	$34.0^{+6.9}_{-5.8}$	$30.7^{+6.6}_{-5.5}$	$3.1^{+3.0}_{-1.7}$	$-0.82^{+0.15}_{-0.10}$

(a) Errors on the X-ray counts were computed according to Table 1 and 2 of Gehrels (1986) and correspond to the 1σ level in Gaussian statistics. The upper limits are at the 3σ confidence level.
(b) The hardness ratio is defined as $HR = \frac{H-S}{H+S}$ where H and S are the counts in the hard (2.0-7.0 keV) and soft (0.5-2.0 keV) bands. We calculated errors at the 1σ level for the hardness ratio following the method described in §1.7.3 of Lyons (1991).
(c) Sources observed by XMM for which we provide EPIC pn information.
(d) Source observed by *Swift*-XRT.

Table 2.3
Optical and X-ray properties

Object	$m_{1450\,Å}$	$M_{1450\,Å}$	$\log(\nu L_\nu)$ (2500 Å)	f_x 0.5−2 keV	L 2−10 keV	α_{ox}	N_H
(1)	(2)	(3)	(4)	(5)	(6)	(7)	(8)
J1427+3522	21.9	−24.7	45.5	< 5.0	< 2.0	< -1.27	–
J1148+5253	23.1	−23.5	45.1	$0.2^{+0.2}_{-0.1}$	$0.1^{+0.09}_{-0.05}$	$-1.65^{+0.12}_{-0.12}$	–
" [a]	"	"	"	< 17.0	< 7.1	< -0.89	–
J0129-0035 [a]	22.3	−24.3	45.4	< 2.0	< 0.9	< -1.37	–
J1044−0125 [a]	19.2	−27.4	46.7	$3.1^{+0.5}_{-0.4}$	$1.0^{+0.2}_{-0.1}$	$-1.77^{+0.02}_{-0.02}$	< 2.0
J0836+0054	18.8	−27.8	46.8	$11.6^{+2.7}_{-3.8}$	$4.2^{+1.0}_{-1.4}$	$-1.61^{+0.03}_{-0.06}$	< 1.4
J0002+2550	19.0	−27.6	46.8	$3.9^{+2.4}_{-1.6}$	$1.7^{+1.0}_{-0.7}$	$-1.76^{+0.08}_{-0.09}$	–
J0840+5624	20.0	−26.7	46.4	$0.9^{+0.7}_{-0.5}$	$0.4^{+0.3}_{-0.2}$	$-1.85^{+0.10}_{-0.13}$	–
J0005−0006	20.2	−26.5	46.3	$2.5^{+2.7}_{-1.9}$	$1.5^{+1.5}_{-0.6}$	$-1.65^{+0.12}_{-0.22}$	< 1.5
J1425+3254	20.6	−26.1	46.1	< 5.3	< 2.4	< -1.46	–
J1335+3533	19.9	−26.8	46.4	$0.4^{+0.4}_{-0.2}$	$0.2^{+0.2}_{-0.1}$	$-1.97^{+0.12}_{-0.12}$	–
J1411+1217	20.0	−26.7	46.4	$3.5^{+2.3}_{-2.0}$	$1.4^{+0.6}_{-0.6}$	$-1.62^{+0.08}_{-0.14}$	< 2.8
J328.7339−09.5076 [a]	20.4	−26.3	46.2	< 2.0	< 0.9	< -1.65	–
J2053+0047	21.2	−25.5	45.9	< 3.4	< 1.6	< -1.45	–
J0148+0600 [a]	19.4	−27.3	46.7	< 1.2	< 0.6	< -1.52	–
J007.0273+04.9571	20.2	−26.5	46.3	< 1.2	< 0.6	< -1.78	–
J0216−0455 [a]	24.1	−22.6	44.8	< 2.5	< 1.2	< -1.06	–
J1306+0356	19.6	−27.1	46.6	$3.3^{+0.8}_{-0.7}$	$1.2^{+0.3}_{-0.3}$	$-1.70^{+0.04}_{-0.04}$	< 2.5
J1630+4012	20.6	−26.1	46.2	$2.1^{+0.8}_{-0.7}$	$0.9^{+0.3}_{-0.2}$	$-1.62^{+0.05}_{-0.07}$	< 1.4
J0303−0019	21.3	-25.4	45.9	< 7.8	< 3.8	< -1.30	–
J1602+4228	19.9	−26.8	46.5	$5.5^{+1.4}_{-1.3}$	$3.4^{+0.6}_{-0.5}$	$-1.57^{+0.04}_{-0.05}$	< 1.5
J2216−0016 [a]	23.2	−23.5	45.2	< 3.0	< 1.5	< -1.17	–
J1048+4637	19.2	−27.6	46.8	$0.8^{+0.8}_{-0.4}$	$0.4^{+0.4}_{-0.2}$	$-2.02^{+0.12}_{-0.12}$	–
J1623+3112	20.1	−26.7	46.4	$0.9^{+0.7}_{-0.4}$	$0.5^{+0.4}_{-0.2}$	$-1.84^{+0.10}_{-0.10}$	–
J0100+2802	17.6	−29.2	47.5	$3.5^{+2.3}_{-1.8}$	$1.4^{+0.9}_{-0.7}$	$-2.01^{+0.08}_{-0.12}$	< 2.6
" [a]	"	"	"	$7.2^{+0.4}_{-0.9}$	$3.4^{+0.4}_{-0.5}$	$-1.88^{+0.01}_{-0.02}$	< 2.1
J025.6821−33.4627 [b]	19.0	-27.8	46.9	$1.9^{+0.8}_{-0.4}$	$0.7^{+0.3}_{-0.1}$	$-2.02^{+0.06}_{-0.04}$	< 6.7
J1030+0524	19.7	−27.1	46.6	$2.1^{+1.3}_{-0.8}$	$1.1^{+0.7}_{-0.4}$	$-1.77^{+0.08}_{-0.08}$	–
" [a]	"	"	"	$5.7^{+0.9}_{-1.1}$	$2.6^{+0.3}_{-0.4}$	$-1.60^{+0.02}_{-0.03}$	< 0.3
J1148+5251	19.0	−27.8	46.9	$2.4^{+0.6}_{-0.5}$	$1.3^{+1.2}_{-0.5}$	$-1.86^{+0.04}_{-0.04}$	< 5.5
" [a]	"	"	"	$0.8^{+0.8}_{-0.5}$	$0.5^{+0.5}_{-0.3}$	$-2.03^{+0.11}_{-0.16}$	–
J0210−0456 [a]	22.6	−24.2	45.5	< 10.0	< 5.5	< -0.91	–
J1120+0641	20.4	−26.6	46.5	$1.0^{+0.8}_{-0.5}$	$0.7^{+0.6}_{-0.4}$	$-1.81^{+0.10}_{-0.14}$	–
" [a]	"	"	"	$0.7^{+0.1}_{-0.2}$	$0.4^{+0.1}_{-0.1}$	$-1.92^{+0.03}_{-0.04}$	< 0.8

(1) Object name. (2) Monochromatic apparent AB magnitude at the rest-frame wavelength $\lambda = 1450$ Å. (3) Absolute magnitude at the rest-frame wavelength $\lambda = 1450$ Å (see §4). (4) Luminosity at the rest-frame wavelength of 2500 Å. (5) Galactic absorption-corrected flux in the observed 0.5-2 keV band in units of 10^{-15} erg cm^{-2} s^{-1}. Upper limits and errors are reported at the 3σ level and 1σ level, respectively. (6) Luminosity in the 2.0-10.0 keV rest-frame band in units of 10^{45} erg s^{-1}. (7) The optical-X-ray power-law slope. (8) Upper limits to the column density for detected sources with > 10 net counts in units of 10^{23} cm^{-2}.
(a) Sources observed by XMM. X-ray properties were derived averaging the results obtained for the three detectors (pn, MOS1, MOS2). (b) Source observed by *Swift*-XRT.

Chapter 3

The deep X-ray observation of the quasar SDSS J1030+0524 at z = 6.31

In this chapter we present the results from the X-ray observations of the $z = 6.31$ QSO SDSS J1030+0524. In particular, we report here the results from our ∼500 ks *Chandra* ACIS-I observation of SDSS J1030+0524, that represents the deepest X-ray look at a $z > 6$ QSO to date. The results of this chapter have been published in Nanni et al. (2018).

As explained in §1.6.1, how the 10^{8-10} $M_{\odot}$ black holes (BHs) powering $z \sim 6$ QSOs could form and grow within 1 Gyr (the age of the Universe at $z \sim 6$) is still unknown, but is widely believed that early massive BHs form in overdense environments, that may extend up to 10 physical Mpc (pMpc), and host large gas quantities (Overzier et al. 2009; Dubois et al. 2013; Costa et al. 2014; Barai et al. 2018). Deep and wide imaging observations of a 8×8 pMpc^2 region around the QSO SDSS J1030+0525 at $z = 6.31$ showed that this field features the best evidence to date of an overdense region around a $z \sim 6$ QSO (Morselli et al. 2014; Balmaverde et al. 2017). In the last few years, our group has obtained data in the optical and X-ray bands to further investigate and confirm the presence of the putative overdensity, and to obtain one of the highest quality spectrum ever achieved in X-ray for a QSO at $z \sim 6$. SDSS J1030+0525 at $z = 6.31$ (Fan et al. 2001) was one of the first $z \sim 6$ QSOs discovered by the Sloan Digital Sky Survey (SDSS), and its field is part of the Multiwavelength Chile-Yale survey (MUSYC). It has also been covered by HST/WFC3. Near-IR spectroscopy showed that it is powered by a BH with mass of 1.4×10^9 $M_{\odot}$ (Kurk et al. 2007; De Rosa et al. 2011). It was not detected in the submillimeter (Priddey et al. 2003) and radio bands (Petric et al. 2003), but it was detected in the X-rays by *Chandra* (one 8-ks snapshot in 2002; Brandt et al. 2002) and by XMM-*Newton* (one 105-ks

observation in 2003; Farrah et al. 2004). In concordance with literature results on other $z \sim 6$ QSOs, the rest-frame optical continuum shape and luminosity of this QSO are consistent with those of lower redshift AGN (Fan et al. 2001). The X-ray spectrum is instead possibly steeper than standard QSOs spectra ($\Gamma \sim 2.1 - 2.4$; Farrah et al. 2004 and Nanni et al. 2017).

In §3.1 we describe the *Chandra* data of SDSS J1030+0524, and the data reduction procedure. In §3.2 we report the data analysis and spectral fitting, the X-ray variability, and the study of the diffuse emission around the QSO. In §3.3 we discuss the physical conditions that can be responsible for the X-ray observed features, provide the multiband SED of the QSO, and discuss the possible origins of the diffuse emission. In §3.4 we give a summary of our results.

3.1 *Chandra* observations

The source SDSS J1030+0524 was observed by *Chandra* with ten different pointings between January and May 2017 for a total exposure of 479 ks. Observations were taken using the Advanced CCD Imaging Spectrometer (ACIS) instrument and the target was positioned on the ACIS-I3 chip, at roll-angle $\sim$64° for the first five observations, and at roll-angle $\sim$259°, for the others. The ten observations (hereafter ObsIDs) cover a total area of roughly 335 arcmin^2 in size and the exposure times of the individual observations range from 26.7 to 126.4 ks. A summary of the observational parameters is provided in Table 3.1. The data were reprocessed using the *Chandra* software CIAO v. 4.8 using the *vfaint* mode for the event telemetry format. Data analysis was carried out using only the events with ASCA grades 0, 2, 3, 4, and 6. We then produced X-ray images in the soft ($0.5-2$ keV), hard ($2-7$ keV) and full ($0.5-7$ keV) bands for each ObsID.

After this basic reduction, we corrected the astrometry (applying shift and rotation corrections) of the individual ObsIDs using as reference catalog the WIRCAM catalog comprising 14777 J-band selected sources down to $J_{AB} = 24.5$ (Balmaverde et al. 2017). First we created exposure maps and psf maps for all ObsIDs using the CIAO tools *fluximage* and *mkpsfmap*, respectively. The exposure and psf maps were computed in the full band at the 90% of the encircled energy fraction (EEF) and at an energy of 1.4 keV. Then, we ran the *Chandra* source detection task *wavdetect* on the $0.5-7$ keV images to detect sources to be matched with the J-band detected objects. We set the detection threshold to 10^{-6} and wavelet scales up to 8 pixels in order to get only the brightest sources with a well defined X-ray centroid and we also provided the exposure and psf maps. For the match we considered only the X-ray sources with a positional error[1] below $\sim$0.4", in order

[1]Computed as: $\sqrt{\sigma_{RA}^2 + \sigma_{Dec}^2}$, where σ_{RA} and σ_{Dec} are the errors on Right Ascension and Declination, respectively.

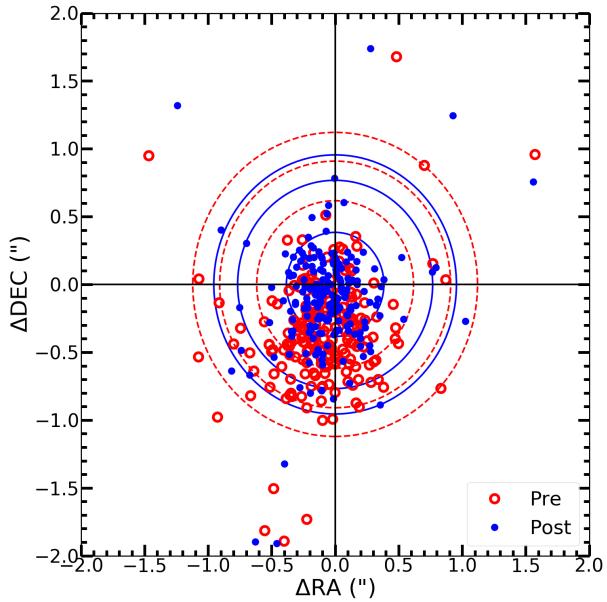

Figure 3.1: X-ray to J-band separation (ΔR.A., ΔDecl.) in arcseconds for X-ray sources detected in each single observations (with a false-positive probability detection threshold to 10^{-6}; see §3.1 for the details) before (red open circles) and after (blue solid circles) the astrometric correction. The circles encompass 68%, 90%, and 95% of the sources before (red dashed line) and after (blue solid line) the correction.

to avoid sources with too uncertain centroid position. We used the CIAO tool *wcs_match* and *wcs_update* to match the sources and correct the astrometry, and create new aspect solution files. We considered a matching radius of 2" and we applied both translation and rotation corrections. The new aspect solutions were then applied to the event files and the detection algorithm was run again (using the same *wavdetect* parameters and criteria adopted previously). The applied astrometric correction reduces the mean angular distance between the X-ray sources and their J-band counterparts from $\theta = 0.253$" to $\theta = 0.064$". After applying the astrometric correction, 95% of the X-ray sources used for the astrometry correction have a distance to their optical counterpart smaller than 0.95", 15% lower than the value before the correction (1.12"). The improvement in the position slightly increases to 16% when considering 90% of the sources (0.77" to 0.91") and significantly increases to ∼40% when considering a smaller sample of 68% of the sources (from 0.38" to 0.62"; see Fig. 3.1).

Finally, we stacked the corrected event files using the *reproject_obs* task and derived a new image of the field. In Fig. 3.2 we display the final *Chandra* full-band image around the QSO position.

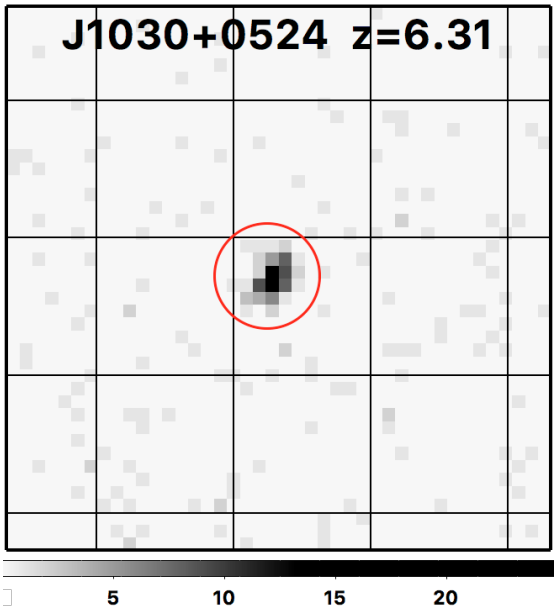

Figure 3.2: Full-band ($0.5-7$ keV) *Chandra* ACIS-I image of SDSS J1030+0524. The red circle represents our extraction region (2" radius). The grid separation is 5" and the cutout spans 20"x20" on the sky. Units on the colorbar are counts per pixel.

3.2 Results

3.2.1 Timing analysis

The long total exposure taken on a time span of five months enabled us to study the possible presence of flux and spectral variability. We extracted the number of counts in each ObsID from circular regions centered at the optical position of the QSO. We used a radius of 2", corresponding to 95% of the encircled energy fraction (EEF) at 1.5 keV, for the source extraction, and a nearby region (free of serendipitously detected sources), with a 100 times larger area, for the background extraction. In the final four columns of Table 3.1 we report the full ($0.5-7$ keV), soft ($0.5-2$ keV), hard ($2-7$ keV) band net counts, extracted in each single observation, and the hardness ratios (HRs), computed as HR $= \frac{H-S}{H+S}$ where H and S are the net counts in the hard and soft bands, respectively.

We first determined whether the QSO varied during the *Chandra* observations by applying a χ^2 test to its entire light curve in the full band. This is computed as

$$\chi^2_\nu = \frac{1}{N-1}\sum_{i=1}^{N}\frac{(f_i-\bar{f})^2}{\sigma_i^2} \tag{3.1}$$

where f_i and σ_i are the full band count rates and its error in the ith observation, $\bar{f}$ is

Table 3.1
Data information on J1030+0524

ObsID	Date	θ^a [°]	t^b_{exp} [ks]	$\mathrm{Cts}^c_{(0.5-7\,keV)}$	$\mathrm{Cts}^c_{(0.5-2\,keV)}$	$\mathrm{Cts}^c_{(2-7\,keV)}$	HR^d
18185	2017 Jan 17	64.2	46.3	$9.5^{+4.3}_{-3.1}$	$3.0^{+3.0}_{-1.7}$	$6.5^{+3.8}_{-2.6}$	$+0.37^{+0.38}_{-0.37}$
19987	2017 Jan 18	64.2	126.4	$39.5^{+7.5}_{-6.4}$	$30.4^{+6.7}_{-5.6}$	$9.1^{+4.3}_{-3.1}$	$-0.54^{+0.15}_{-0.17}$
18186	2017 Jan 25	64.2	34.6	$7.9^{+4.0}_{-2.8}$	$4.0^{+3.2}_{-1.9}$	$3.9^{+3.2}_{-1.9}$	$-0.01^{+0.46}_{-0.41}$
19994	2017 Jan 27	64.2	32.7	$6.3^{+3.8}_{-2.6}$	$3.8^{+3.2}_{-1.9}$	$2.5^{+2.9}_{-1.7}$	$-0.21^{+0.56}_{-0.47}$
19995	2017 Jan 27	64.2	26.7	$4.9^{+3.4}_{-2.2}$	$3.0^{+3.0}_{-1.7}$	$1.9^{+2.7}_{-1.3}$	$-0.22^{+0.60}_{-0.52}$
18187	2017 Mar 22	259.2	40.4	$11.8^{+4.6}_{-3.4}$	$6.9^{+3.8}_{-2.6}$	$4.9^{+3.4}_{-2.2}$	$-0.17^{+0.35}_{-0.33}$
20045	2017 Mar 24	259.2	61.3	$6.7^{+3.8}_{-2.6}$	$4.0^{+3.2}_{-1.9}$	$2.7^{+3.0}_{-1.7}$	$-0.19^{+0.51}_{-0.45}$
20046	2017 Mar 26	259.2	36.6	$13.6^{+4.9}_{-3.7}$	$9.9^{+4.3}_{-3.1}$	$3.7^{+3.2}_{-1.9}$	$-0.46^{+0.29}_{-0.31}$
19926	2017 May 25	262.2	49.4	$12.5^{+4.7}_{-3.6}$	$5.8^{+3.6}_{-2.4}$	$6.7^{+3.8}_{-2.6}$	$+0.07^{+0.35}_{-0.32}$
20081	2017 May 27	262.2	24.9	$9.4^{+4.3}_{-3.1}$	$4.8^{+3.4}_{-2.2}$	$4.6^{+3.4}_{-2.2}$	$-0.02^{+0.43}_{-0.38}$

(a) Roll-angle in degrees of the ACIS-I instrument.

(b) Exposure time after background flare removal.

(c) Net counts in the full ($0.5-7$ keV), soft ($0.5-2$ keV), and hard ($2-7$ keV) bands, respectively. Errors on the X-ray counts were computed according to Table 1 and 2 of Gehrels (1986) and correspond to the 1σ level in Gaussian statistics.

(d) The hardness ratio is defined as $HR = \frac{H-S}{H+S}$ where H and S are the counts in the hard (2.0-7.0 keV) and soft ($0.5-2$ keV) bands. We calculated errors at the 1σ level for the hardness ratio following the method described in §1.7.3 of Lyons (1991).

the average count rate of the source and N is the number of the X-ray observations. The null hypothesis is that the count rate in each epoch is consistent with the mean count rate of the entire light curve, within the errors. We show the distribution of the count rates in the three bands (full, soft, and hard) vs time, starting from the first observation, in Fig. 3.3, where the red lines represent the mean weighted value of the rates. We computed the probability by which the null hypothesis can be rejected (p), and obtained $p \sim 0.47$ (0.44, and 0.40) for the full (soft, and hard) band, respectively. We then conclude that there is no evidence for count rate variability among our *Chandra* observations. The HR distribution vs the observation time is reported in Fig. 3.4. Despite some fluctuations, also the HRs of the different observations show no significant variability ($p = 0.53$).

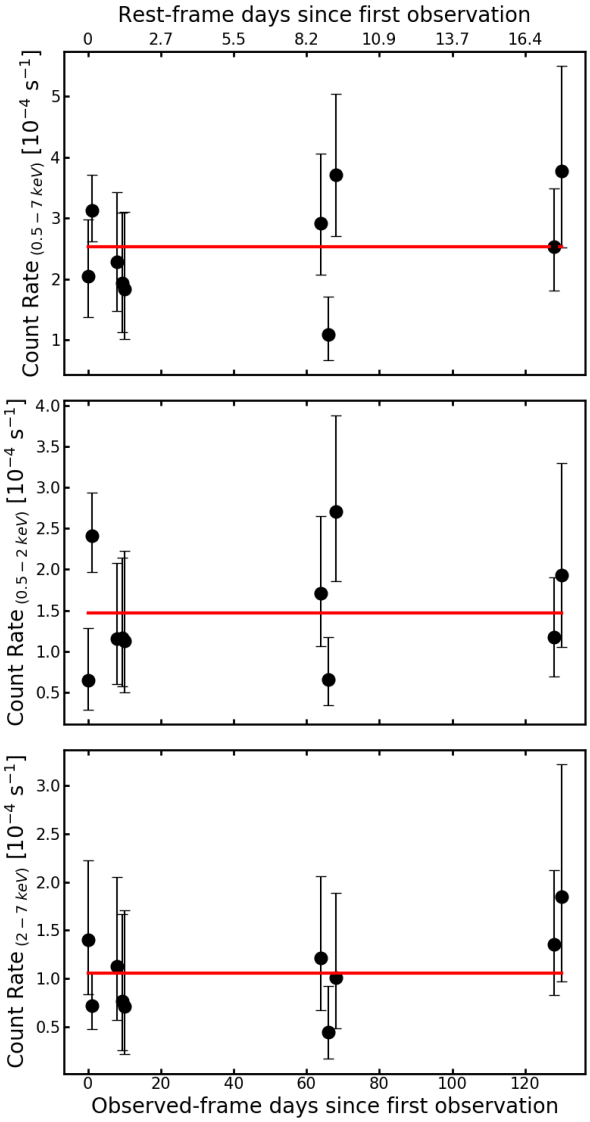

Figure 3.3: Count rate of SDSS J1030+0524 in the three X-ray bands (full in the top, soft in the middle, and hard in the bottom panel) extracted from the ten *Chandra* observations vs the days since the first observation. Errors are reported at the 1σ level. The red solid lines represent the weighted mean.

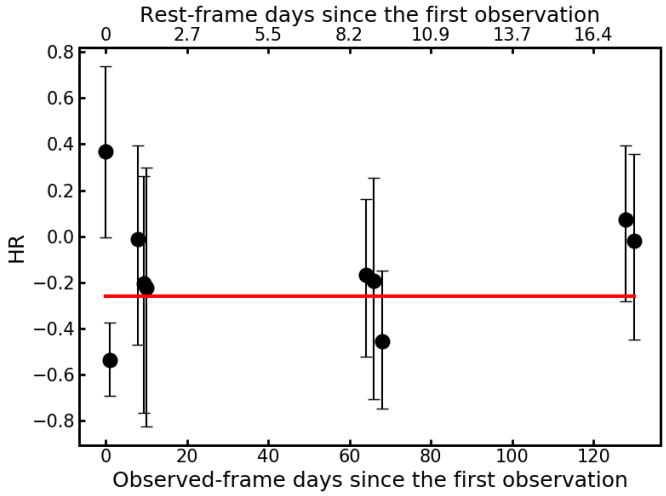

Figure 3.4: Hardness ratio of SDSS J1030+ 0524 in the ten *Chandra* observations vs the days since the first observation. Errors are reported at the 1σ level. The red solid line represents the weighted mean.

3.2.2 Spectral analysis

The lack of significant flux and hardness ratio variability allowed us to combine the ten spectra together (each extracted from the corresponding event file), and obtain a final spectrum with 125 net counts in the full band. The spectral channels were binned to ensure a minimum of one count for each bin, and the best-fit model was decided using the Cash statistics (Cash 1979). First, we modeled the spectrum with a simple power-law, using XSPEC v. 12.9 (Arnaud 1996), with a Galactic absorption component fixed to 2.6×10^{20} cm^{-2} (the value along the line of sight toward the QSO, Kalberla et al. 2005). We found that the best-fit photon index is $\Gamma = 1.81^{+0.18}_{-0.18}$ (C-stat = 88.3 for 93 d.o.f.), and the flux in the $0.5-2$ keV band is $1.74^{+0.11}_{-0.38} \times 10^{-15}$ erg s^{-1} cm^{-2}. The value of the photon index is consistent with the mean photon indices obtained by jointly fitting spectra of unobscured QSOs at the same and at lower redshifts ($\Gamma \sim 1.6-2.0$ for $1 \leq z \leq 7$; e.g., Vignali et al. 2005; Shemmer et al. 2006; Just et al. 2007; Nanni et al. 2017; Vito et al. 2018), but it is flatter than the XMM-*Newton* value found for the same QSO by Farrah et al. (2004) ($\Gamma = 2.12^{+0.11}_{-0.11}$) and by Nanni et al. (2017) ($\Gamma = 2.39^{+0.34}_{-0.30}$; although they fit a power-law plus intrinsic absorption model). Also our measured soft flux is 3.6 times lower than the one derived by Farrah et al. (2004) ($f_{0.5-2} = 6.3 \times 10^{-15}$ erg s^{-1} cm^{-2}), and this difference is significant at the 4σ level (see §3.2.3 for a detailed study of the long-term variability). The spectrum and its best-fit model and residuals are shown in Fig. 3.5.

We performed other fits by adding spectral components to the power-law plus

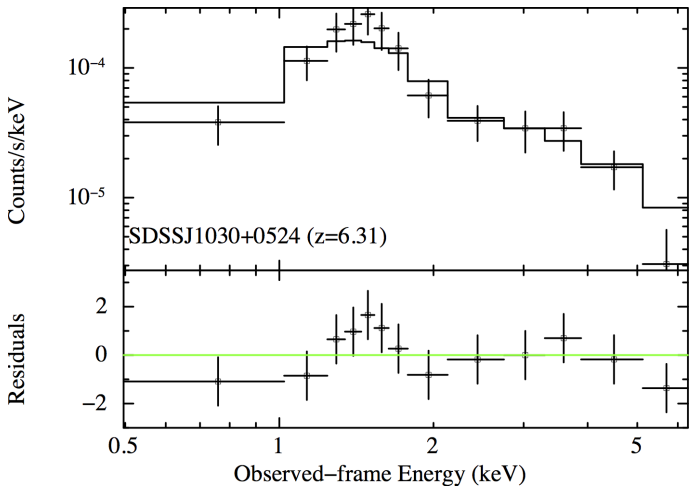

Figure 3.5: X-ray spectrum of SDSS J1030+0524 fitted with a power-law model ($\Gamma = 1.81^{+0.18}_{-0.18}$). In the bottom panel we report the residuals [(data−model)/error]. For display purposes we adopted a minimum binning of ten counts per bin.

Galactic absorption model. First, we added an intrinsic absorption component. Because of the very high redshift of the QSO, this fit is sensitive only to very high values of obscuration ($N_H \geq 10^{23-24}$ cm^{-2}). We found that the column density is poorly constrained and consistent with no absorption ($N_H \leq 7.3 \times 10^{23}$ cm^{-2}), as it may be expected for a luminous Type 1 QSO such as J1030+0524. Then, we fit the same model with the photon index fixed to $\Gamma = 2.39$ (best-fit value found in the XMM-*Newton* data for this QSO by Nanni et al. 2017) and we found $N_H = 5.3^{+1.8}_{-1.7} \times 10^{23}$ cm^{-2}. To search for the presence and significance of a narrow emission iron line, we also added to the power-law model (with photon index fixed to $\Gamma = 1.8$) a Gaussian line, with rest-frame energy of 6.4 keV and width of 10 eV (both fixed in the fit). We obtained a fit with similar quality (C-stat/d.o.f. = 88.4/93) to that of the single power-law model and we derived an upper limit for the rest-frame iron line equivalent width of EW $\leq$ 460 eV. We also checked the presence of iron lines at rest-frame energy of 6.7 and 6.97 keV (as expected from highly ionized iron, FeXXV and FeXXVI), obtaining a rest-frame equivalent width of EW $\leq$ 420 eV in both cases. Considering that we are sampling rest frame energies in the range 3.5-50 keV, where a hardening of AGN spectra is often observed because of the so called "Compton-reflection hump"[2], we checked the possible contribution to the spectrum of a reflected component (*pexrav* model) finding that the photon index is poorly constrained ($\Gamma = 1.72^{+0.95}_{-0.16}$). The possible presence of a FeXXVI emission line at 6.7 keV in the XMM-*Newton*

[2]The "Compton-reflection hump" is radiation from the hot corona that is reprocessed by the accretion disk, and peaks at ∼30 keV.

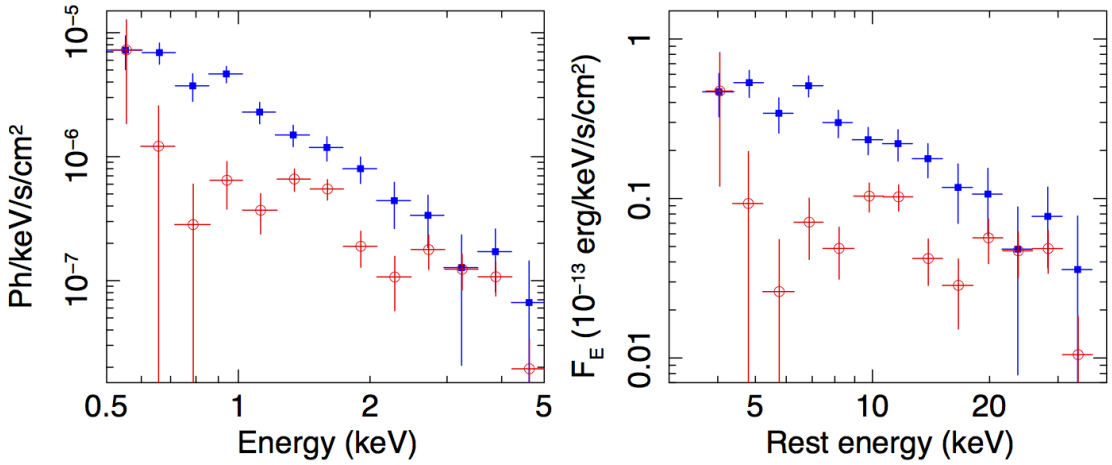

Figure 3.6: Comparison between the 2003 XMM-*Newton* (in blue) and 2017 *Chandra* (in red) spectrum of SDSS J1030+0524. Both spectra have been corrected for the effective response. The XMM-*Newton* spectrum is the average of the three EPIC cameras (with S/N weighting). The left panel shows the observed-frame spectra, while the right panel shows the rest-frame one.

spectrum, with significance at the 2.5σ level, suggested us to fit the *Chandra* spectrum with a power-law model plus a reflection ionized component (*reflionx*). However, we obtained an ionization parameter that is poorly constrained and so is the normalization of the reflection component.

Finally, we noted the possible presence of a dip in the *Chandra* spectrum at $\sim$2.4 keV observed-frame ($\sim$17.5 keV rest-frame; see red spectrum in Fig. 3.6). Previous studies of X-ray AGN spectra revealed the presence of blue-shifted Fe K-shell absorption lines, at rest-frame energies > 7 keV, possibly related to ultra-fast outflows (UFOs) of gas ejected from the QSOs with velocities $\geq 10^4$ km s^{-1} observed at low-redshift (e.g., Tombesi et al. 2013; Tombesi et al. 2015). We then checked the presence of absorption features producing this dip, fitting the spectrum with a power-law model (with Γ free to vary) plus an absorption line component. We generated 10^4 fake spectra (using the same response files and statistics of our original spectrum), and fit them with the power-law plus absorption line model; the adopted procedure is fully described in Lanzuisi et al. (2013) and Tombesi et al. (2013). Comparing the C-stat distribution of the 10^4 fake spectra with the one obtained for the original one, we found that the absorption feature is not significant ($<2\sigma$ level). We also noted the presence of a dip in the 5-10 keV rest-frame energy range (Fig. 3.6), followed by a rise at lower energies, that could be related to the absorption by warm absorbers; however, this rise at low energies contains only 1-2 counts per bin. We tried to fit this low-energy dip with a warm

Table 3.2
Best-fit results of the *Chandra* data

Model (1)	C-stat/d.o.f. (2)	Γ (3)	Parameter (4)	$f_{(0.5-2\,keV)}$ (5)	$f_{(2-7\,keV)}$ (6)	$L^{rest}_{(2-8\,keV)}$ (7)
Power-law (PL)	88.3/93	$1.81^{+0.18}_{-0.18}$	...	$1.74^{+0.11}_{-0.38}$	$2.20^{+0.17}_{-0.55}$	$6.14^{+0.85}_{-2.21}$
PL plus absorption	88.2/92	$1.87^{+0.48}_{-0.21}$	$N_H = 4.6^{+2.7\dagger}_{-4.6}$	$1.68^{+0.13}_{-0.23}$	$2.18^{+0.19}_{-0.27}$	$6.97^{+1.69}_{-1.55}$
PL plus absorption$^\diamond$	89.4/93	2.39	$N_H = 5.3^{+1.8\dagger}_{-1.7}$	$1.42^{+0.23}_{-0.22}$	$2.05^{+0.28}_{-0.29}$	$17.2^{+4.3}_{-3.7}$
PL plus iron line‡	88.4/93	1.8	EW $\leq$ 464 eV	$1.83^{+0.17}_{-0.11}$	$2.07^{+0.10}_{-0.20}$	$6.34^{+0.97}_{-0.38}$
PL plus reflection	87.9/92	$1.72^{+0.95}_{-0.16}$	$Rel_{refl} \leq 14$	$1.74^{+0.12}_{-0.13}$	$2.20^{+5.67}_{-0.79}$	$5.88^{+4.82}_{-1.84}$

(1) Model fit to the X-ray spectrum. (2) C-stat value vs the degrees of freedom. (3) Photon index found or used in the fit. (4) Best-fit value of the corresponding fit-model parameter. (5), (6) Fluxes in the observed $0.5-2$ and $2-7$ keV bands in units of 10^{-15} erg cm^{-2} s^{-1}. (7) Intrinsic luminosity in the rest-frame $2-10$ keV band in units of 10^{44} erg s^{-1}. Errors are reported at the 1σ level and upper limits at the 3σ level.
$\diamond$ Fitting model in which Γ was fixed to the best-fit value found in the XMM-*Newton* data for this QSO by Nanni et al. 2017.
‡ For this model we report results for the case with a Kα emission iron line with fixed rest-frame energy of 6.4 keV and width of 0.01 keV. Γ was fixed to 1.8.
† The column density is reported in units of 10^{23} cm^{-2}.

absorber (*warmabs*[3]) plus a power-law model, fixing the photon index to the *Chandra* ($\Gamma = 1.81$) and XMM-*Newton* ($\Gamma = 2.39$) best-fit values. In both cases we found best-fit values of column density ($N_H \sim 6 \times 10^{23}$ cm^{-2}) and ionization parameter ($log(x_i) \sim 2$) that point back to a cold absorber scenario (the one we tested with the power-law plus absorption model). Furthermore, these values are not well constrained due to the limited counting statistics. Finally, we also tried to fit the rise at low energies with a power-law plus a partial covering absorption model (*zxipcf*), fixing again the photon index to the *Chandra* ($\Gamma = 1.81$) and XMM-*Newton* ($\Gamma = 2.39$) best-fit values. Also in that case, the result points back to a cold absorber scenario ($N_H \sim 7 \times 10^{23}$ cm^{-2}, $log(x_i) \leq 2$, and covering factor of $f \sim 0.9$) with a similar statistical quality of the fit. In Table 3.2 we summarize the results of our spectral analysis.

3.2.3 Comparison with previous analysis

J1030+0524 has been observed in the X-rays twice in the past: by *Chandra* in 2002 and by XMM-*Newton* in 2003. As reported in §3.2.2, our derived soft band

[3] *Warmabs* can be used within XSPEC to fit to observed spectra the results of XSTAR, a software package for calculating the physical conditions and emission spectra of photoionized gas (Kallman & Bautista 2001).

Chandra flux is ∼3.6 times lower than that observed by XMM-*Newton*.

We derived the observed-frame full band ($0.5 - 7$ keV) fluxes for the 2002, 2003, and 2017 observations to build the long-term X-ray light curve (see Fig. 3.7). From the fit we performed on the 2017 *Chandra* observation, using a simple power-law model (first row in Table 3.2), we found $f_{0.5-7\,keV} = 3.96^{+0.18}_{-0.83} \times 10^{-15}$ erg s^{-1} cm^{-2}.

For the *Chandra* snapshot we extracted the number of counts from a circular region with 2" radius, centered on the source position, and the background counts from a nearby circular region with ten times larger area. The source is detected with ∼6 net counts in the full band. Assuming a power-law with $\Gamma = 1.8$, we derived a full band flux of $f_{0.5-7\,keV} = 5.4^{+3.0}_{-2.1} \times 10^{-15}$ erg s^{-1} cm^{-2}, which is 1.4 times higher than the value found for the 2017 observation but consistent with it within the uncertainties.

For the XMM-*Newton* observation, we extracted the three spectra (pn, MOS1, MOS2) from circular regions centered at the optical position of the QSOs with radius of 15", corresponding to 65% of EEF at 1.5 keV, to avoid contamination from nearby luminous sources, while the background was extracted from a nearby region with radius of 30". We used a grouping of one count for each bin for all spectra of the three cameras, and fit the three EPIC spectra (pn, MOS1 and MOS2) with a simple power-law model with photon index free to vary. We obtained a best-fit value $\Gamma = 2.37^{+0.16}_{-0.15}$, that is consistent with the one found by Farrah et al. (2004) but is inconsistent at the 2.4σ level with the value obtained fitting the 2017 *Chandra* data ($\Gamma = 1.81 \pm 0.18$), and a flux $f_{0.5-7\,keV} = 9.78^{+0.44}_{-1.18} \times 10^{-15}$ erg s^{-1} cm^{-2}, that is 2.5 times higher than the full flux derived from the longest *Chandra* observation ($f_{0.5-7\,keV} = 3.96^{+0.18}_{-0.83} \times 10^{-15}$ erg s^{-1} cm^{-2}); the difference is significant at the 4.9σ level. In Fig. 3.7 we show the $0.5 - 7$ keV light curve of the QSO with the fluxes obtained from the three epochs, while in Fig. 3.6 we show the observed-frame (left) and rest-frame (right) spectra of our *Chandra* (in red) and XMM-*Newton* (in blue) analyses. We determined whether the QSO could be considered variable by applying the χ^2 test to its entire light curve in the full band on year timescale, considering the first *Chandra* (2002) and the XMM-*Newton* (2003) observations and our longer *Chandra* observation (2017). We found from our χ^2 test that the QSO has varied ($p \sim 0.99$) with a χ^2 value of 8.51 (d.o.f. = 2).

Previous works (see Appendix B of Lanzuisi et al. (2013)) showed that the XMM-*Newton* source spectra tend to be fitted with softer power-laws (up to 20% difference in photon index) than those observed by *Chandra*. This difference may be now possibly exacerbated by the rapid degradation of the Chandra ACIS-I effective area, which, for instance, has decreased by 18% at 1.5 keV and by 38% at 1 keV between the observations described in Lanzuisi et al. (2013) and ours. In or-

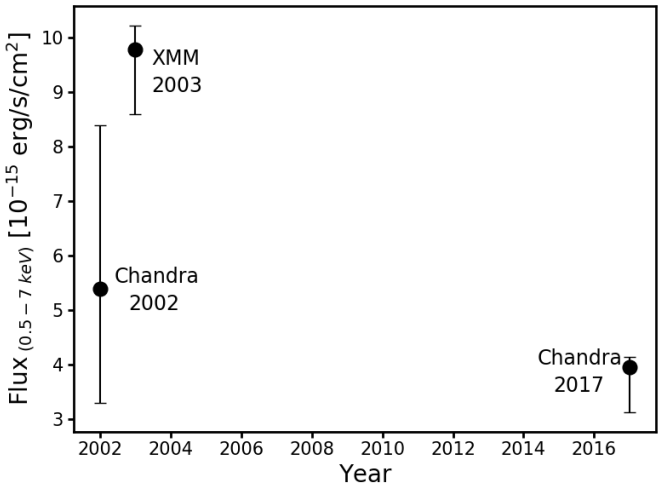

Figure 3.7: Long-term X-ray light curve of SDSS J1030+0524 in the $0.5-7$ keV band. Errors are reported at the 1σ level.

der to verify whether the flux and slope variations are due to the AGN variability and not to any instrumental effect related to the different responses of *Chandra* and XMM-*Newton*, we performed additional checks on the XMM-*Newton* and *Chandra* data-sets. First, we changed the QSO spectral extraction parameters (e.g., size and position of both source and background extraction regions), and the QSO light curve filtering (e.g., cutting the XMM-*Newton* background fluctuations adopting a different thresholds during the data reprocessing) to verify the fit stability, and found that the new best-fit parameters were fully consistent with the XMM-*Newton* values reported above. Secondly, we selected five QSOs detected by both *Chandra* and XMM-*Newton* (with similar counting statistics of our QSO and observed in the central region of the data-sets), and extracted their spectra with the same extraction parameters that we adopted for J1030+0524. We found that the XMM-*Newton* spectra are neither systematically steeper nor brighter than the corresponding *Chandra* spectra, at least in the photon counting statistics regime considered here. Furthermore, our normalized difference in photon index ($(\Gamma_{XMM-Newton}/\Gamma_{Chandra})-1 = 0.31 \pm 0.04$) is three times higher than ($\sim 4\sigma$ off) the mean value found for X-ray sources detected with similar statistic ($(\Gamma_{XMM-Newton}/\Gamma_{Chandra}) - 1$=0.1 in Lanzuisi et al. (2013)). We conclude that the XMM-*Newton* results are stable and that the observed spectral variability in SDSS J1030+0524 is real.

3.2.4 Diffuse emission southward the QSO

By visual inspection of the 2017 *Chandra* observation, we noted an excess of photons extending up to 25" southward of the QSO. This excess becomes more evident by smoothing the image with the task *csmooth*, using a minimal (maximal) signal-to-noise ratio (S/N) of 2 (50), as shown in Fig. 3.8 (top). This diffuse emission lies in a region in which our observations are very sensitive, as shown in Fig. 3.8 (central). We performed photometry on the un-smoothed image, extracting the diffuse counts and spectrum from a region with an area of 460 arcsec^2, shown in Fig. 3.8 (green polygon in the central panel), and the background counts from nearby circular regions (free of X-ray point like sources) with a total area $\sim$3 times larger. We found that the diffuse emission is highly significant, with 90 net counts, corresponding to a S/N = 5.9, and a hardness ratio HR = $0.03^{+0.20}_{-0.25}$. A hint of this diffuse emission is also visible in the XMM-*Newton* observation (bottom panel of Fig. 3.8), at the same sky coordinates, although its significance is less clear as it is difficult to disentangle the diffuse emission from the emission of the nearby QSO, due to the limited XMM-*Newton* angular resolution. Visual inspection of Fig. 3.8 (top) suggests that the diffuse emission may be structured into a few blobs. However, we do not detect any point-like X-ray source running *wavdetect* with a detection threshold relaxed to 10^{-5}.

We fit the diffuse spectrum with a power-law model (including Galactic absorption) and derived a soft band flux of $f_{0.5-2\,keV} = 1.1^{+0.3}_{-0.3} \times 10^{-15}$ erg s^{-1} cm^{-2}. Considering the soft band flux limit for point like sources of our *Chandra* observation ($f_{0.5-2\,keV} \sim 10^{-16}$ erg s^{-1} cm^{-2}), at least 10 unresolved X-ray sources would be required to reproduce the observed diffuse X-ray flux.

We searched in radio and optical bands for sources detected within the region of diffuse X-ray emission. In the radio observation at 1.4 GHz taken by the Very Large Array (down to a 3σ limit of 60 μJy/beam; Petric et al. 2003), we found a radio lobe of a FRII galaxy (RA = 10:30:25.19, Dec = +5:24:28.50; Petric et al. 2003) inside our region (see Fig. 3.9, top). We also considered an archival Hubble Space Telescope WFC3 observation in the F160W filter down to mag 27 AB (bottom panel of Fig. 3.9) and an archival 6.3 hr MUSE observation, both centered on the QSO. The sources for which we were able to analyze MUSE spectra are marked in the image with circles of different colors (see bottom panel of Fig. 3.9): none of them show any sign of AGN activity in their optical spectra.

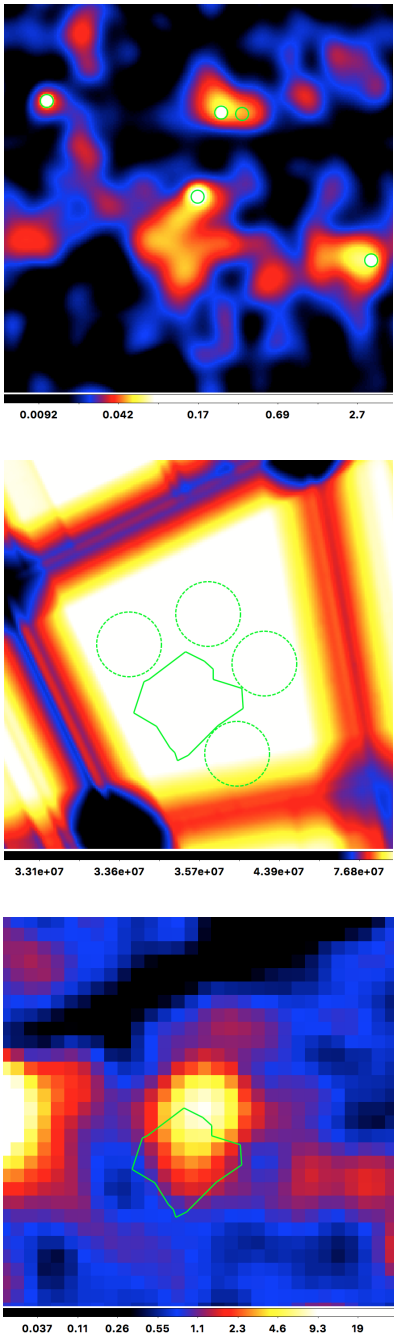

Figure 3.8: *Top panel*: Chandra 0.5-2 keV image ($2'x2'$), smoothed with *csmooth* (see text) and centered at the QSO position. North is up and east is to the left. Green circles mark point-like sources X-ray detected in the soft band. Units on the colorbar are counts per pixel. *Central panel*: $2'x2'$ image of the exposure map computed at 1.4 keV and centered at the QSO position. The green 460 arcsec^2 region is the one used to extract the net counts of the diffuse emission southward on the QSO in the un-smoothed image, and it lays in the most sensitive peak of the exposure map. The four green dashed circles are the regions used to extract the background. Units on the colorbar are cm^2 s per pixel. *Bottom panel*: XMM-*Newton*-pn image in the 0.5-2 keV band ($2'x2'$), centered at the QSO position. Units on the colorbar are counts per pixel.

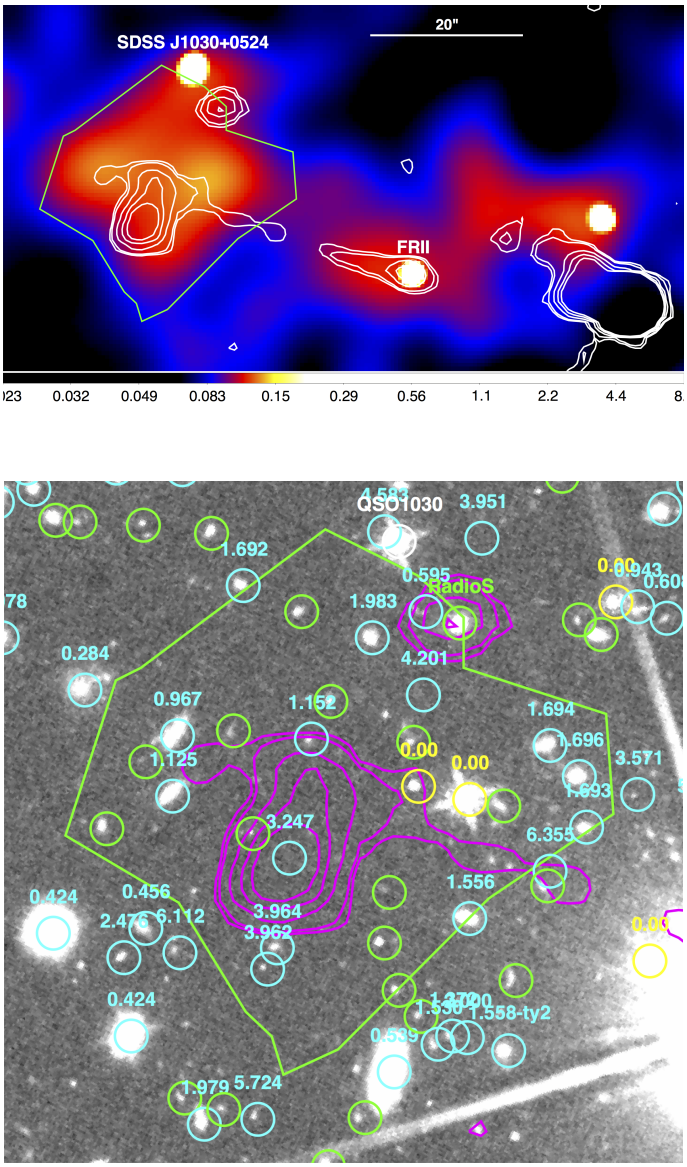

Figure 3.9: *Top panel*: Smoothed Chandra 0.5-7 keV image of the 1.5 × 0.8 arcmin^2 field around SDSS J1030+0524 and the nearby FRII radio galaxy. Radio contours at 1.4 GHz are shown in white. Contour levels are a geometric progression in the square root of two starting at 60 μJy. The green polygon marks the region of diffuse X-ray emission southward of the QSO. Units on the colorbar are counts per pixel. *Bottom panel*: $0.7' \times 0.7'$ HST image in the H-band. Circles are centered at the position of MUSE detected sources. The white circle marks SDSS J1030+0524. Cyan circles mark sources for which a redshift was measured, yellow circles are stars, green circles mark sources for which no redshift was measured. Magenta contours mark the emission of radio sources at 1.4 GHz. The radio lobe of a FRII radio galaxy (Petric et al. 2003) falls within the region of X-ray diffuse emission (green polygon). In both panels, another radio source is visible at the edge of the diffuse X-ray emission (6" south-west the QSO). In all images north is up and east is to the left.

3.3 Discussion

3.3.1 Variability amplitude

To compare the variability seen in SDSS J1030+0524 with that typically seen in AGN, we computed its normalized excess variance, as defined by Nandra et al. (1997) and Turner et al. (1999), and compared it with what is measured in the samples of Shemmer et al. (2017) and Paolillo et al. (2017). Paolillo et al. (2017) measured the variability amplitude (σ^2_{rms}), in the rest-frame $2-8$ keV band, primarily for minimizing the effects of variable obscuration, of X-ray-selected AGN in the 7 Ms exposure of the *Chandra* Deep Field-South (CDF-S) survey (Luo et al. 2017). This sample includes variable and non-variable radio-quiet AGN. Shemmer et al. (2017) studied a luminous sample of four radio-quiet quasars (RQQs) at $4.10 \leq z \leq 4.35$, monitored by *Chandra* at different epochs. Both Shemmer et al. (2017) and Paolillo et al. (2017) found that the X-ray variability anticorrelates with intrinsic AGN X-ray luminosity. This effect has been also observed in samples of nearby AGN and has been interpreted as the consequence of a larger BH mass in more luminous objects, which would also increase the size of the last stable orbit of the accretion disk and thus influence the overall variability produced in its innermost parts (Papadakis 2004).

We derived the rest-frame $2-8$ keV (observed-frame $0.3-1$ keV) band fluxes of the three observations and computed the corresponding X-ray variance and error. In Table 3.3 we summarize the observed-frame full band and the rest-frame $2-8$ keV band fluxes, and luminosity obtained from our best-fit models and analysis described in §3.2.3. Considering the rest-frame $2-8$ keV band fluxes reported in Table 3.3, we obtained an X-ray variance $\sigma^2_{rms} = 0.36 \pm 0.20$. The weighted mean luminosity of the three X-ray observations is $L_{2-8\,keV} = 1.23^{+0.08}_{-0.17} \times 10^{45}$ erg/s. This value of σ^2_{rms} is nominally 8 times higher than the average value found for QSOs of similar luminosities by Paolillo et al. (2017) and Shemmer et al. (2017). However, because of the limited monitoring of the X-ray light curve, the formal errors on the excess variance are much smaller than the true uncertainties, which should be assessed with dedicated simulations (see Paolillo et al. 2017). Therefore, we are not able to determine whether the observed variability is still consistent with what is typically observed in luminous QSOs. For instance, in 2003 XMM-*Newton* may have caught the QSO in a burst period produced by an enhanced accretion episode. Further X-ray observations are needed to determine what is the typical flux state of SDSS J1030+0524, increasing the X-ray monitoring of the QSO and adding more data points to the light curve shown in Fig. 3.7.

Table 3.3
Best-fit fluxes

Observation	Γ	$f_{(0.5-7\,keV)}$	$f^{rest}_{(2-8\,keV)}$	$L^{rest}_{(2-8\,keV)}$
(1)	(2)	(3)	(4)	(5)
Chandra 2002†	1.9	$5.4^{+3.0}_{-2.1}$	$1.8^{+0.9}_{-0.7}$	$0.9^{+0.5}_{-0.3}$
XMM-*Newton* 2003‡	$2.37^{+0.16}_{-0.15}$	$9.78^{+0.44}_{-1.18}$	$5.11^{+0.33}_{-0.72}$	$2.80^{+0.15}_{-0.34}$
Chandra 2017	$1.81^{+0.18}_{-0.18}$	$3.96^{+0.18}_{-0.83}$	$1.16^{+0.15}_{-0.37}$	$0.61^{+0.09}_{-0.22}$

(1) X-ray observation of J1030+0524. (2) Photon index found or used in the fit. (3) Flux in the observed-frame $0.5-7$ keV band in units of 10^{-15} erg cm^{-2} s^{-1}. (4) Flux in the rest-frame $2-8$ keV band in units of 10^{-15} erg cm^{-2} s^{-1}. (5) Luminosity in the rest-frame $2-8$ keV band in units of 10^{45} erg s^{-1}. Errors are reported at the 1σ level.
† For the 2002 *Chandra* observation we report the values derived from PIMMS, assuming a power-law model of $\Gamma = 1.9$.
‡ For the XMM-*Newton* observation we provide the photon index obtained from the joint fit and the fluxes and luminosity obtained averaging the values from the three detectors (pn, MOS1, MOS2).

3.3.2 Spectral variability

The results reported in §3.2.3 highlighted a significant spectral variation between the XMM-*Newton* and the *Chandra* observations. We investigated the possibility that the high X-ray flux level and the steep QSO spectrum measured by XMM-Newton are contaminated by the diffuse X-ray emission seen southward of the QSO in the *Chandra* image, which is partly included in the 15"-radius extraction region used for the analysis of the XMM-*Newton* spectrum of the QSO. To this goal, we first considered the portion of diffuse emission falling within r < 15" from the QSO, extracted its spectrum, and fit it with a power-law model. This spectrum contains about 1/3 of the total photons and flux of the diffuse emission reported in §3.2.4. Then, we fit the XMM-*Newton* spectrum of the QSO with a double power-law model, where the best fit slope and normalization of one of the two power law components were fixed to the best fit values measured for the diffuse emission within r < 15" from the QSO. As a result of this test, we found that the diffuse component contributes less than 10% to the QSO flux measured by XMM-*Newton*, and also has negligible impact on its spectral slope. The contamination by the diffuse emission is therefore not able to explain the observed X-ray spectral variability.

Spectral changes are often detected in a sizable fraction of high-z AGN samples (e.g., Paolillo et al. 2002), and in about 50% of the cases such changes correlate with flux variations. In our case, the origin of the flattening of the X-ray spectral slope is unclear due to the relatively poor counting statistics that affects all the X-ray observations. This spectral variability could be related to two possible scenarios.

The first one considers a change in the spectral slope related to the variation of the accretion rate with time, that makes the spectrum of the QSO steeper when the accretion rate is higher (Sobolewska & Papadakis 2009). To test this scenario, we computed the X-ray Eddington ratio $\lambda_{X,E} = L_{2-10\,keV}/L_E$, as defined in Sobolewska & Papadakis (2009), where $L_E = 1.3 \times 10^{38} M_{BH}/M_\odot$ erg s^{-1} is the Eddington luminosity, and $M_{BH} = 1.4 \times 10^9$ $M_\odot$ in SDSS J1020+0524 (Kurk et al. 2007; De Rosa et al. 2011). We computed $\lambda_{X,E}$ for the 2017 *Chandra* ($\lambda_{X,E} = 0.004^{+0.001}_{-0.002}$) and the 2003 XMM-*Newton* ($\lambda_{X,E} = 0.019^{+0.002}_{-0.001}$) observations and found that they are in general agreement with the $\Gamma - \lambda_{X,E}$ relation found by Sobolewska & Papadakis (2009). The second scenario considers the "flattening" effect caused by an occultation event, for instance produced by gas clouds in the broad line region or in the clumpy torus, as sometimes observed in local AGN (Risaliti et al. 2007). As shown in §3.2.2, an intervening gas cloud with $N_H \sim 5.3 \times 10^{23}$ cm^{-2} is needed to reproduce the observed "flattening" of a power-law with $\Gamma \sim 2.4$, that is the photon index found in the XMM-*Newton* observation. Removing the absorption term from the power-law plus absorption model (the third one reported in Table 3.2), we derived a full band flux of $f_{0.5-7\,keV} = 5.8^{+0.26}_{-1.22} \times 10^{-15}$ erg s^{-1} cm^{-2}, that is 1.7 times lower than the one found with XMM-*Newton* (with a 3σ significance). We conclude that the spectral and flux variabilities are not related to a simple absorption event, but that this must be coupled with an intrinsic decrease of the source power.

3.3.3 The multi-wavelength SED

In Fig. 3.10 we provide the multi-wavelength SED of SDSS J1030+0524, which is one of the $z \sim 6$ QSO best studied in different bands. The XMM-*Newton* and *Chandra* values are from this work; LBT values from Morselli et al. (2014) (r, i, z bands); *Spitzer* and *Herschel* fluxes from Leipski et al. (2014) (IRAC and MIPS for *Spitzer*; PACS and SPIRE for *Herschel*); *Scuba* values from Priddey et al. (2008) (at 1250, 850, 450 μm); CFHT values from Balmaverde et al. (2017) (Y, J bands); H-band and K-band values are from the MUSYC survey (Gawiser et al. 2006); VLA value from Petric et al. (2003) (at 1.4 GHz); ALMA flux from Decarli et al. (2018) (at 252 GHz). The QSO SED is consistent with the combined SED of lower redshift QSOs, of Richards et al. (2006) (green curve in Fig. 3.10), showing that SDSS J1030+0524 has the typical optical properties of lower redshift luminous AGN.

Decarli et al. (2018) studied the FIR properties of luminous high-z AGN, based on a sample of 27 QSOs at $z \geq 5.9$ observed with ALMA. SDSS J1030+0524 is one of the few objects in the sample that is not detected in the [CII] (158 μm), and is only marginally detected in the continuum, suggesting a star formation rate (SFR) < 100 $M_\odot$/yr, whereas the average SFR in the sample is a few hundreds

$M_\odot$/yr. This may suggest that SDSS J1030+0524 is in a more evolved state than the other luminous QSOs at that redshift, that is, it may be in a stage where the star formation in its host is being quenched by its feedback (Hopkins et al. 2008; Lapi et al. 2014).

We use the full-band *Chandra* flux and the 1450 Å magnitude of the QSO ($m_{1450\,\text{Å}} = 19.7$; Bañados et al. 2017) to compute the optical-X-ray power-law slope, defined as in Equation 2.1. The flux density at 2500 Å was derived from the 1450 Å magnitude, assuming a UV-optical power-law slope of 0.5. We found $\alpha_{ox} = -1.76^{+0.06}_{-0.06}$, that is consistent with the mean value, $\alpha_{ox} = -1.80^{+0.02}_{-0.02}$, found for sources at the same redshift ($5.9 \leq z \leq 6.5$: Nanni et al. 2017). The errors on α_{ox} were computed following the numerical method described in §1.7.3 of Lyons (1991), taking into account the uncertainties in the X-ray counts and an uncertainty of 10% in the 2500 Å flux corresponding to a mean z-magnitude error of 0.1. Previous works have shown that there is a significant correlation between α_{ox} and the monochromatic L_{2500} Å (α_{ox} decreases as L_{2500} Å increases; Steffen et al. 2006; Lusso & Risaliti 2017; Nanni et al. 2017), whereas the apparent dependence of α_{ox} on redshift can be explained by a selection bias (Zamorani et al. 1981; Vignali et al. 2003; Steffen et al. 2006; Shemmer et al. 2006; Just et al. 2007; Lusso et al. 2010; but see also Kelly et al. 2007) The derived value is not consistent with the one found by Nanni et al. (2017) for XMM-*Newton* data ($\alpha_{ox} = -1.60^{+0.02}_{-0.03}$), that is one of the flattest found among all $z \sim 6$ QSOs. Considering also the already discussed evidence that the XMM-*Newton* photon index is steeper than the mean population of QSOs at $z \sim 6$, we conclude that the properties derived from XMM-*Newton* data do not probably represent the typical status for SDSS J1030+0524 (that is probably more similar to that found with *Chandra*), strengthening the idea that the higher flux measured by XMM-*Newton* is related to an episodic burst occurred during that observation.

We also checked for the presence of long-term optical variability by comparing the J-band magnitude taken from MUSYC in 2003 (Quadri et al. 2007) with the one taken by WIRCAM in 2015 (Balmaverde et al. 2017). We used stars in both images to calibrate for the differences in aperture correction and in the filter response, finding a r.m.s. in the distribution of magnitude differences of $\Delta mag \sim 0.04$. From 2003 to 2015 the QSO decreased its luminosity by $\Delta mag \sim 0.1$. Therefore, the variation is significant only at 2σ, and if it is on the order of 10% or less as suggested by our measurements, it would have negligible impact on the reported α_{ox} values.

3.3.4 Origin of the diffuse emission

The origin of the diffuse X-ray emission seen southward of the QSO is far from being clear. We discuss below some possible interpretations.

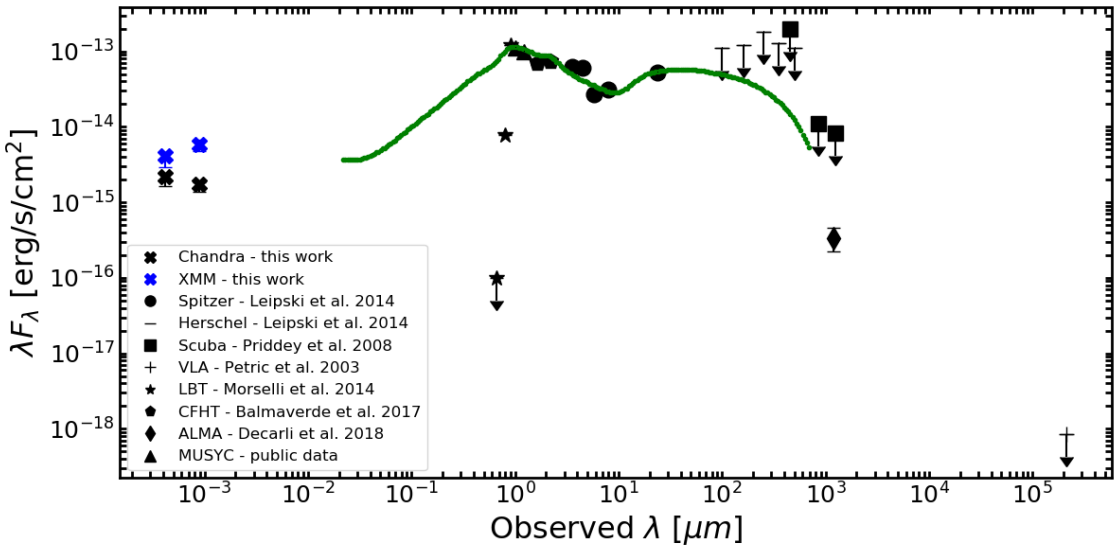

Figure 3.10: Multi-wavelength SED of SDSS J1030+0524. References to the points are labeled. The green curve is the combined SED for luminous lower redshift QSOs taken from Richards et al. (2006). The drop on the SED of SDSS J1030+0524 at $\lambda < 1$ μm is produced by the Lyman alpha forest.

Unresolved sources or foreground group or cluster

In the 460 arcsec^2 region where we find significant excess of X-ray emission (see Fig. 3.8, top) we do not detect any X-ray point-like source down to $f_{0.5-2\,keV} = 10^{-16}$ erg s^{-1} cm^{-2} and we do not find any sign of AGN activity in any of the MUSE spectra of the optical sources we were able to extract in the same region. An implausibly high surface density of undetected point-like X-ray sources (100 times larger than that expected by the logN-logS relation at $f_{0.5-2\,keV} = 10^{-16}$ erg s^{-1} cm^{-2}; Luo et al. 2017) would be required to reproduce entirely the observed flux.

The number density of optical sources detected within the extended X-ray emission is similar to that in nearby regions, and neither the angular distribution of galaxies within the region, nor the redshifts measured with MUSE (see Fig. 3.9, bottom) suggest the presence of a foreground group or cluster. Therefore, we can exclude the presence of a foreground virialized group or cluster as responsible for the diffuse X-ray emission.

Emission from a foreground radio galaxy

A radio-galaxy with FRII morphology was found ∼40" south-west of the QSO in a relatively deep VLA observation at 1.4 GHz with ∼1.5" resolution (Petric et al. 2003). We reanalyzed the archival VLA data, and derived the radio contours shown

in Fig. 3.9[4] The nucleus of the FRII coincides with a *Chandra* source detected only above 2 keV (with ∼30 net counts), suggesting an extremely obscured nucleus (see Fig. 3.9, top). The Eastern lobe of the FRII has a total radio flux of 1.7 mJy and falls within the region of diffuse emission, while the Western one is much brighter, with a total radio flux of 24 mJy. No X-ray emission is associated with the Western lobe. A radio jet is also seen running from the radio core to the Eastern lobe. Because of the beamed nature of the jet synchrotron emission, the Eastern lobe is then supposedly the closest to the observer. A detailed analysis of the radio source is beyond the scope of this work, and will be better described after the analysis of the JVLA data obtained by our group for this field (D'Amato et al. in prep.). Here we discuss its basic properties and the likelihood that the diffuse X-ray emission seen southward of SDSS J1030+0524 can be associated to it.

The emission at 1.4 GHz in the Eastern lobe is not as extended as the diffuse X-ray emission. The interferometric radio observations were, however, conducted with the "A" configuration at the VLA, which may have filtered out diffuse radio emission on scales of tens of arcsec. As a matter of fact, low surface brightness, low significance radio emission in coincidence with the diffuse X-ray structure and even beyond it may be present in the GMRT data of the 150 MHz TGSS survey[5]. Among the possible processes responsible for X-ray emission in radio lobes, we first investigated synchrotron models by extrapolating to the X-rays the flux densities measured at 1.4 GHz and 150 MHz and using the spectral index α measured between the two radio bands ($f_\nu \propto \nu^{-\alpha}$). Because of the widely different angular resolution between TGSS and VLA data (25" vs 3.5" $FWHM$), we also performed tests using data from the NVSS survey at 1.4 GHz (∼45" resolution). Unfortunately, the low S/N of the TGSS data, coupled to the complex structure of the source (the Western lobe heavily contaminates the Eastern emission in NVSS data), prevents us from obtaining a robust estimate of the radio spectral index of the Eastern lobe: we measured values in the range $\alpha \sim 0.7 - 0.9$, depending on the adopted extraction regions. When extrapolating the radio fluxes over more than 8 dex in frequency, this uncertainty in α produces a wide range of predicted X-ray emission, that can be as high as what we measured with *Chandra*. Current data are therefore not sufficient to rule out this possibility, but we note, however, that it would be odd to see X-ray synchrotron emission in the Eastern but not in the Western lobe, that is 5-6 times brighter in the radio bands.

Besides synchrotron emission, there are two other possible scenarios to produce X-ray photons within a radio lobe. The first one involves Inverse Compton

[4]Our data reduction was tuned to achieve a lower resolution ($FWHM \sim 3.5$") to maximize the detection efficiency of the diffuse region emission. The sensitivity limit of our image is $f_{1.4\,GHz} \sim 70$ μJy/beam (3σ).

[5]http://tgssadr.strw.leidenuniv.nl/doku.php

scattering between the relativistic electrons in the lobe and photons coming from either the cosmic microwave background (IC-CMB; e.g., Erlund et al. 2006), the synchrotron photons in the radio lobe itself (Synchro-Self Compton, SSC), or even the photons emitted from the nucleus of the FRII (Brunetti et al. 1997). The latter scenario considers thermal emission produced by diffuse gas shock-heated by the jet (Carilli et al. 2002; Overzier et al. 2005). Unfortunately, we do not have enough photon statistics to distinguish between thermal and non-thermal emission based on the current low S/N X-ray data.

In the IC scenario, the observed hardness ratio of the diffuse X-ray emission would correspond to a power-law with photon index of $\Gamma = 1.6 \pm 0.4$, which is consistent with X-ray emission from radio lobes ascribed to IC processes (e.g., Smail et al. 2012). However, all the diffuse X-ray emission is associated to the fainter, Eastern radio lobe, whereas, if it was produced by SSC or IC, X-ray emission in the Western lobe, which is > 6 times more powerful in the radio band, would be expected as well. In the case of anisotropic scattering of photons from the FRII nucleus, backward scattering would be favored (Brunetti et al. 1997) and one would then expect the farthest (Western) lobe to be the brightest, which is not the case. Ascribing the observed diffuse X-ray emission to processes associated with the FRII radio lobe is not therefore entirely convincing.

As an alternative, the diffuse X-ray emission may be associated with shocked gas, as is sometimes seen in distant ($z \sim 2$) radio galaxies that are embedded in gas-rich large scale structures (Overzier et al. 2005). As there is no spectroscopic redshift for the host of the FRII, we first derived a K-band magnitude from the public data of the MUSYC survey (Gawiser et al. 2006), and then estimated a redshift of $z \approx 1-2$, based on the K-band magnitude vs redshift relation observed for radio-galaxies (e.g., Willott et al. 2003). Assuming that the X-ray emission is thermal, and that both the FRII radio galaxy and the diffuse gas are embedded in a large scale structure at $z = 1.7$ (indeed, there is a weak evidence for a spike at $z = 1.69$ in the redshift distribution of MUSE sources, see the also bottom panel of Fig. 3.9), we derived a temperature of $T \geq 4$ keV for the X-ray emitting gas (using the `apec` model within XSPEC with $0.3\times$ solar metal abundances). Some further diffuse X-ray emission can be recognized in Fig. 3.9 (top) in correspondence of the FRII radio jet and north-west of the FRII core. This emission is at very low S/N, but, if real, it may suggest the presence of other diffuse hot gas in a putative large scale structure. At this redshift, the extension of the diffuse X-ray emission southward of SDSSJ1030+0524 would correspond to 240 physical kpc, and its luminosity to $L_{2-10\,keV} = 3 \times 10^{43}$ erg s^{-1}. Assuming that the point-like X-ray emission observed in the core of the FRII traces the accretion luminosity, we can estimate the power carried out by the jet toward the lobe by considering that this is generally equal or larger than the accretion luminosity (Ghisellini et al. 2014).

At $z = 1.7$, using a photon index of $\Gamma = 1.8$, the hard X-ray source at the FRII nucleus would be a Compton-thick AGN ($N_H \approx 1.5 \times 10^{24}\ cm^{-2}$) with rest-frame deabsorbed 2-10 keV luminosity of $L^{rest}_{2-10} \sim 10^{44}$ erg/s. Adopting a bolometric correction of 30, as appropriate for these X-ray luminosities (e.g., Lusso et al. 2011), we estimate a total accretion luminosity, and hence a total jet power of $P_{jet} \geq 3 \times 10^{45}$ erg s^{-1}. From the fit to the diffuse X-ray emission we derived a gas density of $n \sim 4 \times 10^{-3}$ cm^{-3}, and hence a total thermal energy of $E_{th} \sim nVkT \sim 5 \times 10^{60}$ erg, assuming a spherical volume of radius 120 kpc. To deposit such amount of energy in the gas, the jet would have had to be active at that power for at least 100 Myr (even assuming that the 100% of the jet power is transferred to the gas), which is larger than the typical lifetime of FRII jets ($\sim 1.5 \times 10^7$ yr; Bird et al. 2008). Because of the many uncertainties and assumptions, the above computation must be taken with caution. However, it shows that even thermal emission from gas shock-heated by the FRII jet is not a secure interpretation.

QSO feedback and X-ray jets at $z = 6.31$

Both analytical/numerical models and simulations of early BH formation and growth postulate that a non-negligible fraction of the energy released by early QSOs can couple with the surrounding medium producing significant feedback effects on it (Dubois et al. 2013; Costa et al. 2014; Barai et al. 2018; Gilli et al. 2017). In this scenario, the diffuse X-ray emission may be related to the thermal cooling of environmental gas shock-heated by QSO outflows. This gas can be heated to temperatures higher than 10^8 K on scales that may extend well beyond the virial radius of the dark matter halo hosting the QSO, and reach hundreds of kpc from the QSO depending on the gas density and host halo mass (e.g., Gilli et al. 2017). Significant emission in the X-ray band is then expected (Costa et al. 2014). Also, the morphology of the hot gas may be highly asymmetric, depending on the outflow opening angle (Barai et al. 2018) and even be unipolar, depending on the gas distribution in the BH vicinity (Gabor & Bournaud 2013). The morphology of the diffuse X-ray emission suggests that at least part of it may be indeed associated with the QSO. In fact, a "bridge" of soft X-ray emission appears to originate from the QSO and extend into the south-eastern part of the diffuse X-ray structure (see Fig. 3.8, top-panel).

If the observed diffuse X-ray emission is interpreted as thermally emitting gas at $z = 6.3$ (we used again the `apec` model within XSPEC with 0.3× solar metal abundances), then this should have a temperature of $T \geq 10$ keV, and extend asymmetrically for about 150 physical kpc from the QSO. This is consistent with the simulations above. The observed X-ray emission would then correspond to a luminosity of $L^{rest}_{2-10\,keV} = 5 \times 10^{44}$ erg s^{-1}. As above, we computed the thermal energy of the X-ray emitting gas by assuming that it is distributed in a sphere of

75 kpc radius. We derived a total thermal energy of $\approx 10^{61}$ erg. This is within a factor of two consistent with the predictions of Gilli et al. (2017). In that paper it was calculated that an accreting BH growing to 10^9 $M_\odot$ by $z = 6$, such as that observed in SDSS J1030+0524, may deposit $\sim 5 \times 10^{60}$ erg of energy in the surrounding medium through continuous, gas outflows. Furthermore, based on the thermal model fit we obtain a total gas mass of $M_{gas} \sim 1.2 \times 10^{12}$ $M_\odot$ and hence a total dark matter halo mass of $\geq 8 \times 10^{12}$ $M_\odot$, which would be consistent with the idea that early luminous QSOs form in highest peaks of the density field in the Universe, as further supported by the candidate galaxy overdensity measured around SDSS J1030+0524 (Morselli et al. 2014; Balmaverde et al. 2017). Again, we note that many caveats apply that are related to our assumptions and uncertainties in the physical parameters derived from low S/N X-ray data, so that the above conclusions are still speculative.

The QSO may also be responsible for the extended X-ray emission through non-thermal radiation mechanisms. In particular, it has been proposed that the emission of jets and lobes in high redshift QSOs may be best probed in the X-rays rather than in the radio band. This is because the energy density of the CMB increases as $(1 + z)^4$, causing inverse Compton scattering to dominate over synchrotron emission the energy losses of relativistic electrons (Ghisellini et al. 2014; Fabian et al. 2014). Despite the large uncertainties arising from the low photon statistics and from the image smoothing process, the bridge of soft X-ray emission originating from the QSO in the Eastern part of the diffuse structure reminds of an X-ray jet that is possibly powering a diffuse structure (X-ray lobe). Following Fabian et al. (2014) and Ghisellini et al. (2014), we considered a simple jet IC-CMB model in which the QSO produces a relativistic jet with power equal to the accretion power (10^{47} erg s^{-1}). We assumed that: i) the total power of the relativistic electrons injected in the lobe is 10% of the jet power; ii) the magnetic field strength in the lobe is 15 μG (near equipartition is assumed between magnetic field and relativistic particles); iii) the lobe is a sphere of ≈50 kpc radius. A fiducial power-law spectrum is also assumed for the injected electrons (see Ghisellini et al. 2014). With the above assumptions, both the X-ray luminosity and hardness ratio of the diffuse emission can be reproduced by the IC scattering of CMB photons by the electrons in the lobe, which in turn may also contribute to some of the observed radio emission through synchrotron radiation. The above computation, despite being admittedly uncertain and relying on strong assumptions, provides another plausible emission mechanism for the observed diffuse X-ray emission.

3.4 Summary and conclusions

In this chapter we have reported on the ∼500 ks *Chandra* observation of the QSO SDSS J1030+0524. This is the deepest X-ray observation ever achieved for a $z \sim 6$ QSO. Our main results are the following:

- The QSO has been detected with ∼125 net counts in the full band with no evidence of either significant spectral or flux variability during the *Chandra* observations. The spectrum is well fit by a single power-law with $\Gamma = 1.81^{+0.18}_{-0.18}$, that is consistent with the mean value found for luminous AGN at any redshift. No evidence is found for significant absorption ($N_H \leq 4.6^{+2.7}_{-4.6} \times 10^{23}$ cm^{-2}), nor for other additional spectral features.

- A comparison between the QSO X-ray spectral properties in our *Chandra* data with those obtained from a past XMM-*Newton* observation (Farrah et al. 2004; Nanni et al. 2017) revealed that the QSO significantly varied. The full band flux decreased by a factor of 2.5 from the XMM-*Newton* to the *Chandra* observations while the spectrum became flatter ($\Delta\Gamma \approx -0.6$). We verified that these variations are not related to calibration issues. We discussed the possibility that the hardening of the spectral slope is intrinsic and related to variations of the accretion rate. As an alternative, a variation of the obscuration level along the line of site (with Γ fixed at the XMM-*Newton* value) is not sufficient to explain alone the observed variations. However, because of the limited monitoring of the X-ray light curve and the poor counting statistics, we were not able to disentangle between the different scenarios.

- We provided the SED of SDSS J1030+0524, that is one of the best sampled for a $z > 6$ QSO. The SED is consistent with the mean SED of luminous AGN at lower redshift, but it differs in the FIR and sub-millimeter bands with that found for other QSOs at $z \sim 6$. This difference may suggest that SDSS J1030+0524 is in a more evolved state (i.e., with quenched SFR) than the other luminous QSOs at that redshift. We also computed the optical-X-ray power-law slope for the *Chandra* observation, finding $\alpha_{ox} = -1.76^{+0.06}_{-0.06}$. Comparisons between the α_{ox} and the photon index found by XMM-*Newton* with those found by *Chandra*, suggest that the properties derived from XMM-*Newton* data do not probably represent the typical status for SDSS J1030+0524, strengthening the idea that the higher flux measured by XMM-*Newton* is related to an episodic burst occurred during the XMM-*Newton* observation.

- We detected significant diffuse X-ray emission that extends for 30"x20" southward the QSO, with a S/N = 5.9, hardness ratio of $HR = 0.03^{+0.20}_{-0.25}$, and soft band flux of $f_{0.5-2\,keV} = 1.1^{+0.3}_{-0.3} \times 10^{-15}$ erg s^{-1} cm^{-2}. We verified that an implausibly high surface density of undetected point-like X-ray sources would be required to reproduce entirely the observed flux. Based on HST and MUSE data, we also excluded the presence of a foreground galaxy group or cluster. We discussed different scenarios for the origin of this diffuse emission. The first scenario considers the contribution of a radio lobe from a foreground FRII source that could emit X-ray photons via synchrotron or inverse Compton processes. The large uncertainties on the radio measurements and the low X-ray statistics prevented us from excluding or confirming either possibility. However, the absence of X-ray emission from the brightest radio lobe poses challenges to any scenario involving non-thermal processes, as we would expect stronger X-ray emission in the Western lobe, which is > 6 times more powerful in the radio band but has no X-ray diffuse emission. Alternatively, as high-z radio-galaxies are often found in non-virialized large scale structures, the diffuse X-ray may arise from a reservoir of gas in this structure shock-heated by the FRII jet.

  In the second scenario, the diffuse X-ray emission may probe the feedback produced by SDSS J1030+0524 on its close environment. In that case, if the diffuse emission is thermal, the gas should have a temperature of $T \geq 10$ keV, and extend asymmetrically for about 150 physical kpc from the QSO, in agreement with simulations of early BH formation. In addition, supposing that SDSS J1030+0524 is producing a relativistic jet, this would be best probed in the X-rays rather than in the radio band, as the electron energy losses would be dominated by IC scattering of the strong CMB photon field, rather than by synchrotron emission. The energetics, scales and spectral hardness of the observed X-ray emission would also be consistent with this interpretation.

We conclude that SDSS J1030+0524 is one of the best objects to study the spectral properties and the environment of high redshift AGN. New X-ray observations are needed to check the QSO light-curve and to constrain the origin of the extended emission via spectral analysis. In particular, for the near future *Chandra* and XMM-*Newton* monitoring of SDSS J1030+0524 would provide additional information on the QSO variability and the origin of the diffuse emission seen southward the QSO. This will greatly help developing the science cases for future X-ray missions, such as *Athena* and *Lynx*, that will shed new light on the high redshift frontier.

Chapter 4

The deep Chandra survey in the SDSS J1030+0524 field

In this chapter we present the point-source catalog derived from the ∼479 ks *Chandra* exposure of the J1030+0524 field. This X-ray field has a nominal aim point centered on the QSO SDSS J1030+0525 at $z = 6.31$ (presented in Chapter 3). Thanks to the multi-wavelength coverage of the field, we also present multi-wavelength identifications and basic multi-wavelength photometry for the detected X-ray sources. The main goals of our deep *Chandra* observation of J1030 were the following: i) to obtain one of the highest quality spectrum ever achieved in the X-rays for a QSO at $z \sim 6$ (Nanni et al. 2018), ii) to perform a deep X-ray survey in a candidate highly biased region of the Early Universe that has excellent multi-band coverage, iii) to search for possible AGN companions at $z \sim 6$.

Deep X-ray surveys provide a highly efficient method to pinpoint growing black holes in AGN) across a wide range of redshifts, and offer insights about the demographics, physical properties, and interactions with the environments of SMBHs. Furthermore, they are primary tools to study the diffuse emission of clusters and groups, as well as X-ray binaries in star-forming galaxies (e.g., the *Chandra* Deep Field-South by Xue et al. 2011 and Luo et al. 2017, the *Chandra* Deep Field-North (CDF-N) by Xue et al. 2016, the AEGIS-X survey by Nandra et al. 2015, the *Chandra* Ultra Deep Survey (X-UDS) by Kocevski et al. 2018, and the COSMOS Legacy survey by Cappelluti et al. 2009, Civano et al. 2016, and Marchesi et al. 2016).

While shallow large area surveys are essential to cover large portions of the sky, avoiding field-to-field variance problems and providing a global view of the most luminous X-ray sources (i.e., XMM-XXL survey; Menzel et al. 2016), deep X-ray surveys are capable to reach extremely faint flux levels and thus earlier cosmic epochs. In addition, at a given redshift, deep surveys can probe objects with intrinsically low X-ray luminosities (that are generally more representative of

the source population), as well as intrinsically luminous sources that are dimmed by strong nuclear obscuration (e.g., Norman et al. 2004; Comastri et al. 2011; Gilli et al. 2011).

So far, the podium of the deepest X-ray surveys ever achieved is occupied by: the *Chandra* Deep Field-South (CDF-S), with an exposure of ∼7 Ms over an area of 484.2 arcmin^2 (Xue et al. 2011; Luo et al. 2017), the *Chandra* Deep Field-North (CDF-N), with an exposure of ∼2 Ms over an area of 447.5 arcmin^2 (Xue et al. 2016), and the AEGIS-X survey, with an exposure of ∼800 ks over an area of 0.29 deg^2 (Nandra et al. 2015). These surveys achieved unprecedented X-ray sensitivity with flux limits in their inner square arcmins of $\sim 1.9, 0.6, 2.7 \times 10^{-17}$ erg s^{-1} cm^{-2} for CDF-S, $\sim 3.5, 1.2, 5.9 \times 10^{-17}$ erg s^{-1} cm^{-2} for CDF-N, and $\sim 1.5, 3.4, 2.5 \times 10^{-16}$ erg s^{-1} cm^{-2} for AEGIS-X, in the full (0.5-7 keV), soft (0.5-2 keV), and hard (2-7 keV) bands, respectively.

In §4.1 we describe the *Chandra* data, and the data reduction procedure. In §4.2 we report the X-ray source detection procedure with a detailed description of the analysis of source completeness and reliability. In §4.3, we present the main X-ray source catalog, and provide the X-ray sources characterization and multi-wavelength identifications. In §4.4, we present the cumulative number counts for the main source catalog, and in §4.5 we provide a summary of the main results.

4.1 Observations and Data reduction

As explained in §3.1, the SDSS J1030+0524 field was observed by *Chandra* with ten different pointings between January and May 2017 for a total exposure of ∼479 ks, and a summary of the observations is provided in Table 4.1.

The data reduction and astrometric corrections were performed following the procedure described in §3.1. In the end, we stacked the astrometric corrected event files using the *reproject_obs* task and created X-ray images from the merged event file using the standard ASCA grade set in the full, soft, and hard bands. In Fig. 4.1 we display the final *Chandra* full-band image of the X-ray field around SDSS J1030+0525. The individual PSF maps were combined using the task *dmimgcalc* so as to return the exposure-weighted average PSF value at each pixel location in the combined mosaic, while the individual effective-exposure maps were summed together to obtain the total effective-exposure map of the field in the full, soft, and hard bands. The full-band effective-exposure map is shown in Fig. 4.2.

Table 4.1
Data information on the SDSS J1030+0524 field observations

ObsID	Date	θ^a	t^b_{exp}	Aim Point	
		[°]	[ks]	α (J2000)	δ (J2000)
18185	2017 Jan 17	64.2	46.3	10 30 28.35	+05 25 40.2
19987	2017 Jan 18	64.2	126.4	10 30 28.35	+05 25 35.3
18186	2017 Jan 25	64.2	34.6	10 30 28.35	+05 25 35.3
19994	2017 Jan 27	64.2	32.7	10 30 28.35	+05 25 37.6
19995	2017 Jan 27	64.2	26.7	10 30 28.35	+05 25 34.2
18187	2017 Mar 22	259.2	40.4	10 30 26.67	+05 24 07.1
20045	2017 Mar 24	259.2	61.3	10 30 26.66	+05 24 07.5
20046	2017 Mar 26	259.2	36.6	10 30 26.56	+05 24 13.3
19926	2017 May 25	262.2	49.4	10 30 26.68	+05 24 14.2
20081	2017 May 27	262.2	24.9	10 30 26.66	+05 24 15.2

(a) Roll-angle in degrees of the ACIS-I instrument.

(b) Exposure time after background flare removal.

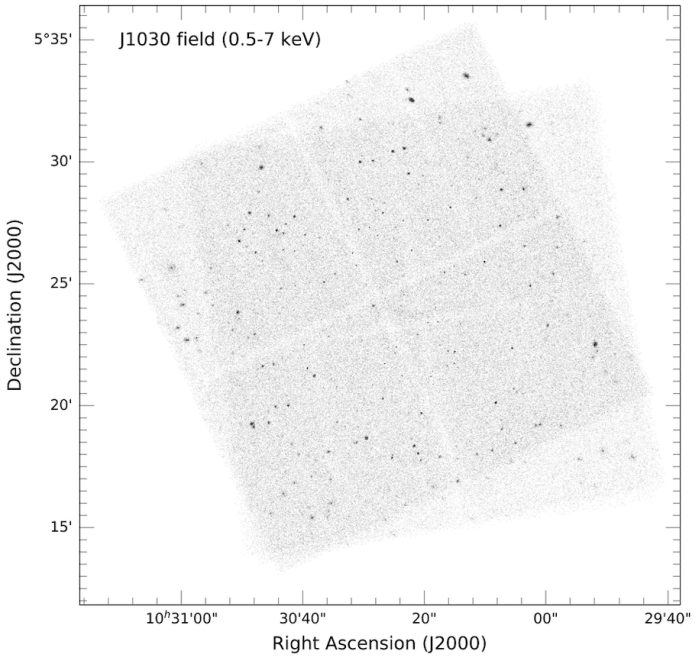

Figure 4.1: Full-band ($0.5 - 7$ keV) *Chandra* ACIS-I image of the SDSS J1030+0524 field in logarithmic gray scale.

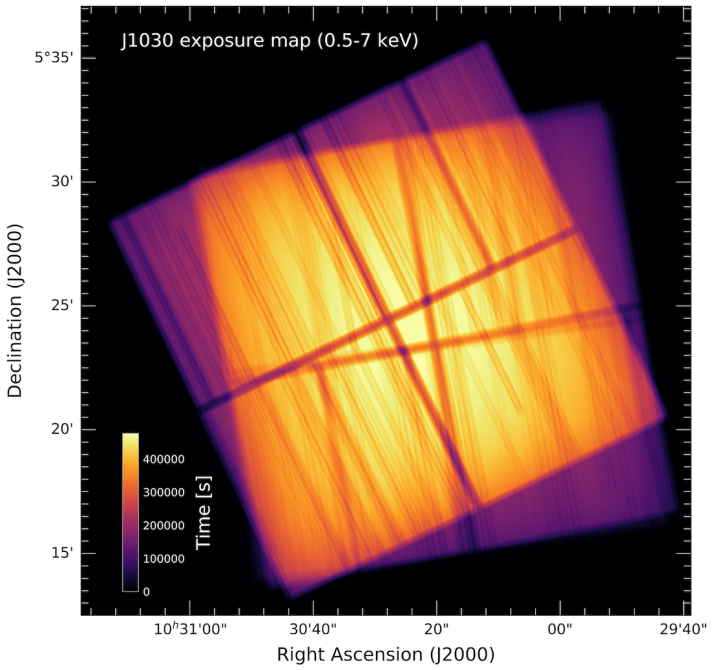

Figure 4.2: Full-band ($0.5 - 7$ keV) *Chandra* effective-exposure map of the SDSS J1030+0524 field. The linear scale color bar is shown in the bottom left; the displayed effective exposure times are in units of s.

4.2 X-ray source detection

The X-ray source detection procedure follows a two-stage approach that has also been adopted for past deep X-ray surveys such as the *Chandra* Deep Field South (i.e., Xue et al. 2011; Luo et al. 2017), the *Chandra* Deep Field North (Xue et al. 2016), and AEGIS-X (Nandra et al. 2015): a preliminary source candidates list was initially generated by *wavdetect* source detection, and then filtered after photometry performed with ACIS Extract (AE; Broos et al. 2012) to produce our final source catalog.

4.2.1 Generation of the Preliminary Catalog

To generate the preliminary candidate source list, we ran *wavdetect* on the merged images in the full, soft, and hard bands, using a sequence of wavelet scales up to 16 pixels (i.e., 1.414, 2, 2.828, 4, 5.656, 8, 11.314, and 16 pixels) and a false-positive probability threshold of 1.e-4. We also provided to *wavdetect* the average PSF maps (§2.1) for each energy band. This produced 498, 383, 370 candidate sources in the full, soft, and hard bands, respectively. Among them 289, 221, and 218 sources are also detected in the full, soft, and hard bands, respectively, when running *wavdetect* with a threshold of 1.e-5. The loose *wavdetect* source-detection threshold of 10^{-4} is expected to introduce a large number of spurious detections that must be filtered out, but also allow us to push the detection to the faintest possible limits.

We then improved the source positions through the AE "CHECK_POSITIONS" procedure and used AE to extract photometric properties of the candidate sources. The details of the AE photometric extraction are described in the AE User's Guide, and a short summary is also provided in Xue et al. (2011). We used AE to perform source and background extractions for each source in each ObsID and then to merge the results. In our case, a polygonal extraction region that approximates the $\sim$90% encircled energy fraction contour, at $E = 1.4$ keV, of the local PSF was utilized to extract source counts. We adopted the AE "BETTER_BACKGROUNDS" algorithm for background extraction (see §7.6.1 of the AE User's Guide), in order to obtain a single background region plus a background scaling that simultaneously models all background components, including the background that arises from the PSF wings of neighboring sources. A minimum number of 100 counts in the merged background spectrum is required to ensure photometric accuracy, which was achieved through the AE "ADJUST_BACKSCAL" stage. The extraction results from individual observations were then merged to produce photometry for each source through the AE "MERGE_OBSERVATIONS" stage. To filter the preliminary catalog, the most important output parameter from AE is the binomial no-source probability (P_B),

which is the probability of observing the same number of source counts or more under the assumption that there is no real source at that location and that the observed number of counts is purely due to a background fluctuation:

$$P_B(X \geq S) = \sum_{X=S}^{N} \frac{N!}{X!(N-X)!} p^X (1-p)^{N-X}, \tag{4.1}$$

where S is the total number of counts in the source extraction region (before background subtraction); $N = S + B_{ext}$, where B_{ext} is the total number of counts in the background extraction region; and $p = 1/(1+BACKSCAL)$ with $BACKSCAL = A_{ext}/A_{src}$ is the ratio between the background and source extraction regions. We computed P_B for each source in all the three (full, soft, hard) bands. Although P_B is a classic confidence level, it is usually not a good indicator of the fraction of spurious sources (e.g., a cut at $P_B = 0.01$ does not correspond to a 1% spurious rate), mainly because the extractions were performed on a biased sample of candidate sources that already survived a filtering process by *wavdetect*. Furthermore, given its definition, the value of P_B is dependent on the choices of source and background extraction regions. Therefore, we cannot reject spurious sources simply based on the absolute value of P_B itself. A P_B threshold derived from simulations has been then adopted to maximize the completeness and reliability of our sample.

4.2.2 Generation of the Simulated Data

To filter our spurious sources from the catalog and to assess the completeness and reliability of our final sample we produced three simulations that mirror our observations, as done in previous X-ray surveys (e.g., Cappelluti et al. 2007; (2009); Puccetti et al. 2009; Xue et al. 2011; (2016); Luo et al. 2017).

First, we considered a mock catalog of X-ray sources (AGN and normal galaxies) that covers one square degree area and reaches fluxes that are well below the detection limit of our ∼479 ks exposure. In this mock catalog, we assigned to each simulated AGN a soft-band flux that was drawn randomly from the soft-band log$N$-log$S$ relation in the AGN population synthesis model by Gilli et al. (2007). Simulated galaxy fluxes were drawn randomly from the soft-band galaxy log$N$-log$S$ relation of the "peak-M" model in Ranalli et al. (2005). The AGN and galaxy integrated fluxes match the cosmic X-ray background (CXB) fluxes. AGN have been simulated down to 2×10^{-19} erg/cm^2/s in the 0.5-2 keV band, galaxies down to 2×10^{-18} erg/cm^2/s in the same band, to include the contribution of undetectable sources that produce the spatially non-uniform background component. The soft-band fluxes of the simulated AGN and galaxies were converted into full-band fluxes assuming power-law spectra with $\Gamma = 1.4$[1] and $\Gamma = 2.0$, respectively.

[1]This value is typically used to translate count rates into fluxes for the population of AGN,

The number of simulated sources has been rescaled for the J1030 field area (∼335 arcmin^2), and source coordinates were randomly assigned within that area. We used the MARX software (v. 5.3.3; Davis et al. 2012) to convert source fluxes to a Poisson stream of dithered photons, and to simulate their detection by ACIS.

Second, we produced ten simulated ACIS-I observations of the mock catalog, each configured to have the same aim point, roll-angle, exposure time, and aspect solution file as one of the J1030 field pointings. These simulated source event files contain the detected emission of the simulated sources from our mock catalog. We then produced the corresponding background event files that are appropriate to the simulated source event files from the J1030 event files. For each real event file, we masked all the events relevant to our preliminary catalog sources and then filled the masked regions with events that obey the local probability distribution of background events (using *blanksky* and *blanksky_sample* tools). The simulated source event files produced by MARX were then merged with the background event files to produce ten simulated ACIS-I pointings that closely mirror the ten real ones.

As a final steps, we followed the same approach adopted above:

- We stacked the simulated event files using the *reproject_obs* task and created X-ray images in all the three X-ray bands from the merged event file (§4.1). As an example, we show in Fig. 4.3 the full-band image of the real J1030 field (top panel) compared to one of our simulated full-band image (bottom panel).

- We ran *wavdetect* on each simulated combined image at a false-positive probability threshold of 1.e-4 to produce a simulated candidate-list catalog, and used AE to perform photometry (including the P_B values) for these simulated sources (§4.2.1).

This procedure allowed us to generate a total of three complete simulations that mirror the J1030 real field and to obtain a simulated preliminary source catalogs from each simulation.

4.2.3 Completeness and reliability

Simulations are the best tools to set a probability threshold (P_B) for sources filtering since we have full control of the input and output sources. After creating the three simulations and the corresponding candidate source catalogs (as described in §4.2.2), we matched the detected output simulated sources with the input sources

since it describes fairly well the observed slope of the CXB and is therefore representative of a sample that includes both unobscured and obscured AGN (Hickox & Markevitch 2006).

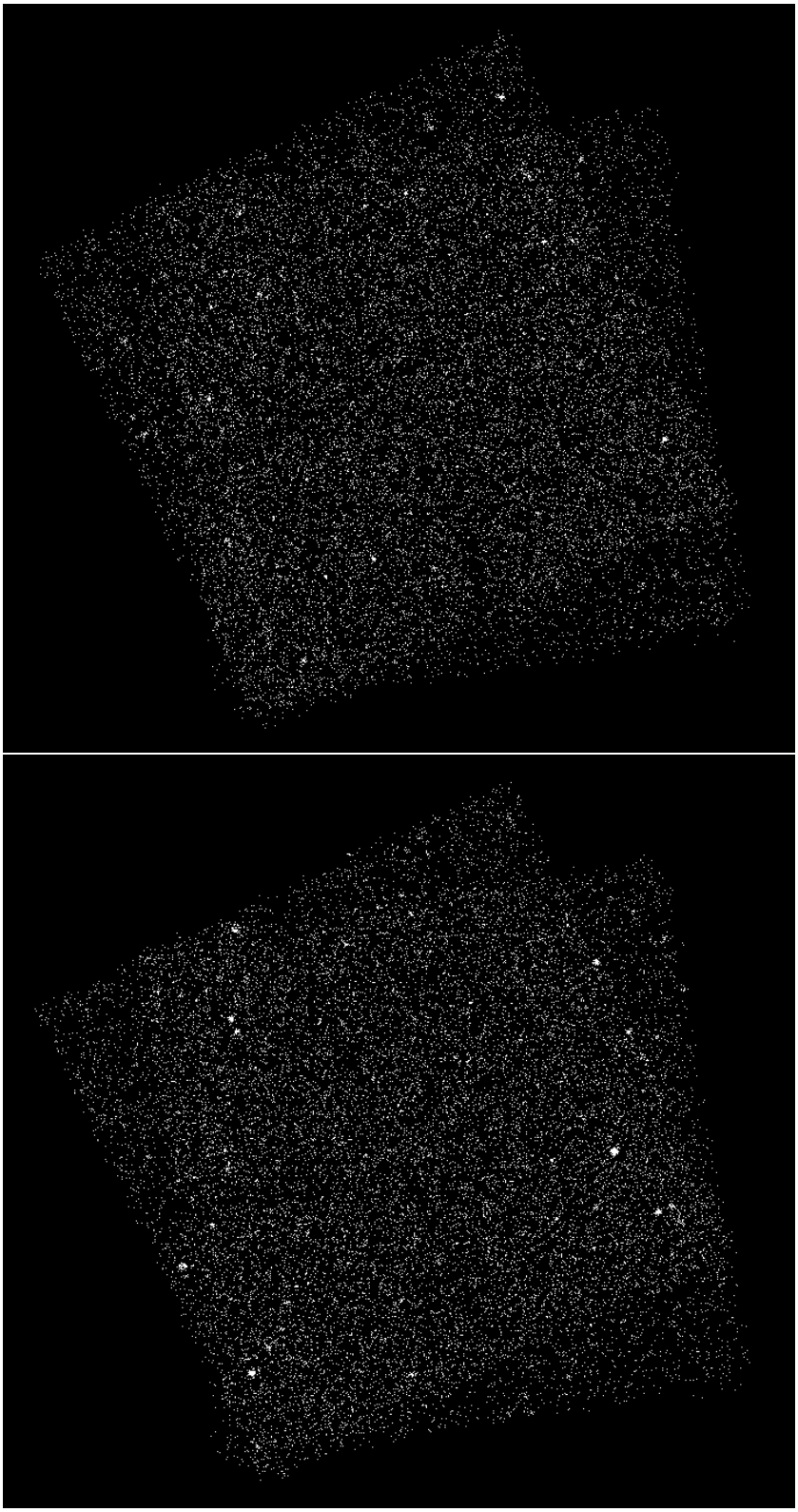

Figure 4.3: Comparison between the real full-band image of J1030 (top) and one of our simulations (bottom). It is evident that the simulated one closely mirrors the real observation.

in the mock catalog, using a likelihood-ratio matching technique (see e.g., Ciliegi et al. 2003).

Briefly, our likelihood-ratio (LR) technique takes into account the positional accuracy of both input and output sources and also the expected flux distribution of the input ones. It assigns likelihood and reliability parameters to all possible counterparts, and mitigates the effect of false matches. For an input source with a flux f at an angular separation r from a given X-ray output, the LR is the ratio between the probability of the input being the true counterpart of the output and the corresponding probability of the input being an unrelated (i.e., background) object (e.g., Ciliegi et al. 2003):

$$LR = \frac{F(r)q(f)}{n(f)} \tag{4.2}$$

where $F(r)$ is the probability distribution function of the angular separation, $q(f)$ is the expected flux distribution of the input sources, and $n(f)$ is the surface density of background objects with flux f. We refer to Appendix A for a complete explanation of Equation 4.2. In our case, for each output source we searched for input sources inside a circular area of $r_{LR} = 5$" (following Luo et al. 2010) centered on the output position, to allow matching of the X-ray sources at large off-axis angles.

A threshold for LR (LR_{th}) is needed to discriminate between spurious and real associations: an output source is considered to have an input counterpart if its LR value exceeds LR_{th}. The choice of LR_{th} depends on two factors: first, LR_{th} should be small enough to avoid missing many real identifications, so that the completeness is high; second, LR_{th} should be large enough to keep the number of spurious identifications low, in order to increase the reliability of the identifications. The reliability of a single input source j, which represents the probability of being the correct identification, is defined as:

$$R_j = \frac{LR_j}{\sum_i LR_i + (1 - Q)} \tag{4.3}$$

where the sum is over all the possible input counterparts for an output source i, and $Q = \int_{f_{lim}}^{+\infty} q(f)df$ is the probability that the input counterpart j is brighter than the flux limit (f_{lim}) of the catalogue. We then defined the reliability parameter (R) for the total sample as the ratio between the sum of the reliabilities of all sources identified as possible counterparts and the total number of sources with $\mathrm{LR} > \mathrm{LR}_{th}$ ($N_{LR>LR_{th}}$):

$$R = \frac{(\sum_j R_j)_{LR>LR_{th}}}{N_{LR>LR_{th}}}, \tag{4.4}$$

We also measure the completeness parameter (C) of the total sample defined as the ratio between the sum of the reliability of all sources identified as possible counterparts and the total number of output sources (N_X):

$$C = \frac{(\sum_j R_j)_{LR>LR_{th}}}{N_X}. \quad (4.5)$$

As explained also in Brusa et al. (2007), LR_{th} was computed as the likelihood-ratio which maximizes the quantity (R + C)/2. We flagged those sources with LR > LR_{th} as real sources ("good" sources) and those with LR < LR_{th} as spurious ones.

We used the matched "good" sources to assess the completeness and reliability of the simulated catalog. Looking at the distributions of the source net counts vs. the off-axis angle in the three bands (full, soft, and hard), we computed three empirical relations (one for each band) to use as source-count limit at various off-axis angles to assess the completeness and reliability. These relations maximize the number of rejected spurious sources and minimize the number of rejected "good" sources as shown in Fig. 4.4. Then, we defined the completeness as the ratio between the number of "good" sources detected with a binomial probability above a certain value and the total number of "good" sources, above a specific source-count limit. The reliability is defined as 1 minus the ratio between the number of spurious sources above a certain probability value and the total number of sources, above a specific source-count limit.

In Fig. 4.5 we show the completeness (black straight line) and reliability (red dashed line) as a function of the P_B for the simulations in the full, soft, and hard bands, for sources that survived our count-limit relation cut. Adopting a probability threshold value of $P_B = 2 \times 10^{-4}$, the completeness levels for the entire J1030 field are 95% (full band), 97% (soft band), and 91% (hard band), while the reliability levels are 95% (full band), 96% (soft band), and 95% (hard band). Finally, we applied our source-count limit cut and the $P_B = 2 \times 10^{-4}$ threshold derived from the simulations as filters for our J1030 preliminary real source catalog: 244, 193, and 208 sources survived in the full, soft, and hard bands, respectively. We then matched the three band catalogs together with a matching radius $r = 5$" (for $5'' < r < 10''$ no additional sources are matched), and visually checked all matches. The final catalog contains 256 unique sources, detected in at least one band.

We also computed the completeness and reliability (following the same approach described above) for source catalogs generated with a *wavdetect* false-positive probability threshold of 1.e-5. Based on simulations, we verified that catalogs generated with *wavdetect* threshold 1.e-5 and ($P_B = 10^{-3}$) have the same reliability and completeness and similar source numbers of those obtained by using 1.e-4 and $P_B = 2 \times 10^{-4}$. After a visual check of those sources that are not in common among the two catalogs, we found that the catalog with a *wavdetect*

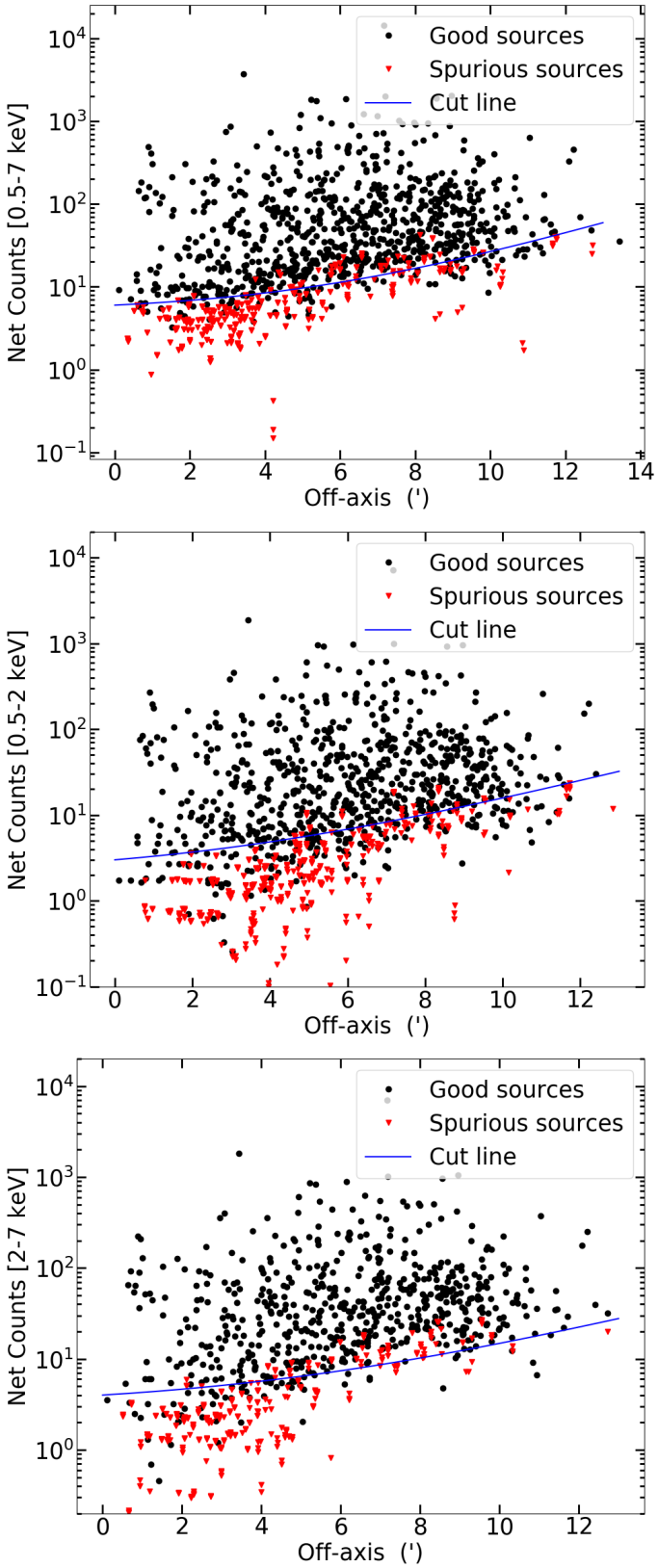

Figure 4.4: Net counts vs off-axis angles of the sources detected in the three simulations in the full (top), soft (middle), and hard (bottom) bands. The black dots are the "good" sources according to the likelihood-ratio method, while the red triangles are those considered spurious. The blue line represents the source-count limit at various off-axis angles that was adopted to compute the completeness and reliability.

Table 4.2
Number of sources detected in at least one band, for each combination of X-ray bands

Band [keV]	Number of sources
F+S+H	156
F+S	31
F+H	46
F	11
S	6
H	6
Total	**256**

The bands reported are the full (F), soft (S), and hard (H).

Table 4.3
Number of sources detected in the SDSS J1030+0524 field and their net counts properties

Band	Number of	Net counts per source				Single
[keV]	sources	Max	Min	Mean	Median	Detections
Full	244	1849.3	6.7	96.5	50.9	11
Soft	193	1196.1	2.7	61.0	41.5	6
Hard	208	647.6	3.4	53.3	40.7	6

In the last column, we show the number of sources detected in only one band.

threshold of 1.e-4 and $P_B = 2 \times 10^{-4}$ have more sources with optical/NIR counterparts within 5" compared to the other one. We then decided to adopt this one as our final catalog for the *Chandra* J1030 field.

4.3 Source catalog

As explained in §4.2.3, our final catalog consists of 256 sources detected in one or more X-ray bands (full, soft, and hard); in Table 4.2 we report the total number of sources for each band combination. Among them 11 sources are detected only in the full-band, 6 only in the soft-band, and 6 only in the hard-band. For each source we derived the net counts, the hardness ratio (HR), and the band fluxes and relative errors or upper limits (for those sources that are not detected in a certain band), as described in §4.3.1. In Table 4.3 we report the basic statistics of the source counts in the three bands.

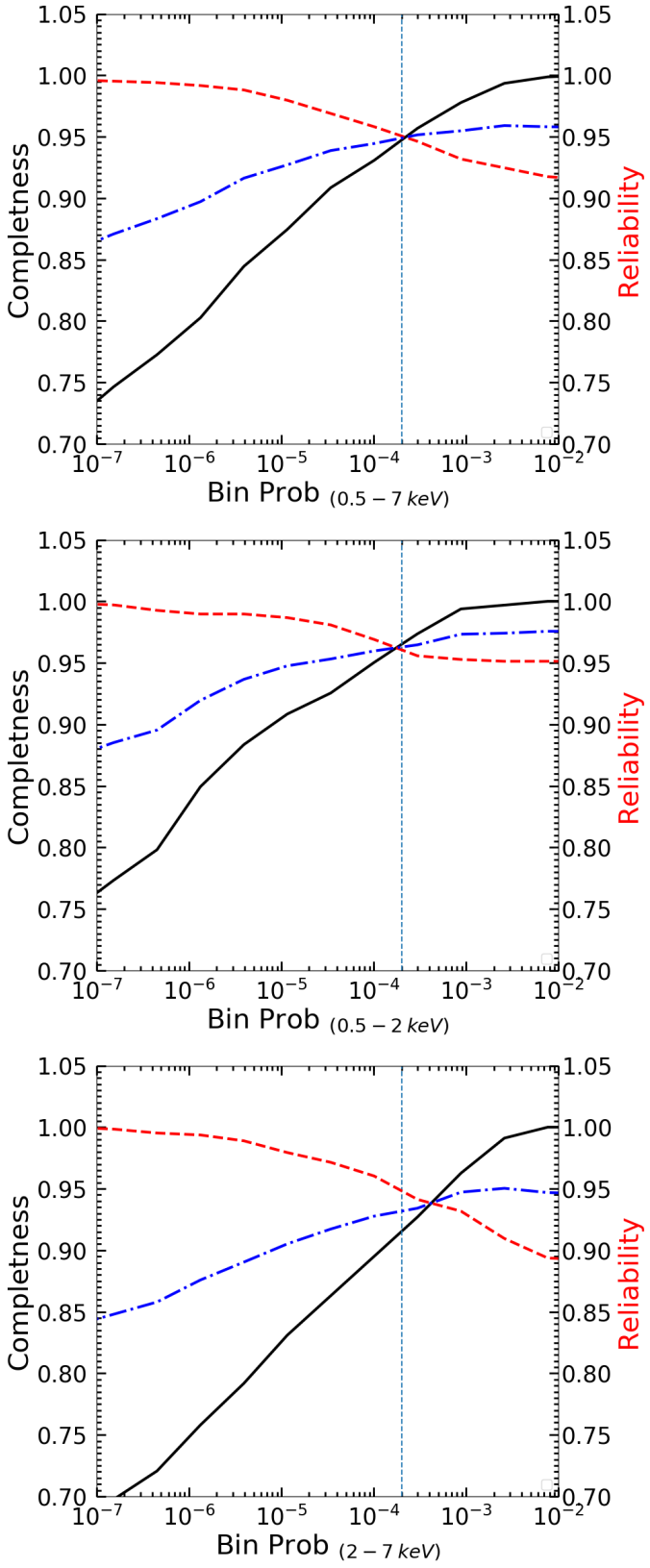

Figure 4.5: Completeness (C, black curve) and reliability (R, red dashed curve) as a function of the binomial no-source probability for the three simulations in the full (top), soft (middle), and hard (bottom) bands, respectively. The blue dot-dashed curve is the (R+C)/2, while the dashed vertical line indicates the chosen source-detection threshold of $P_B = 2 \times 10^{-4}$.

4.3.1 X-ray properties

In each of the three X-ray bands, the net source counts were derived from the AE "MERGE_OBSERVATIONS" procedure using a polygonal extraction region that approximates the $\sim 90\%$ of the encircled energy fraction at $E = 1.4$ keV, as explained in §4.2, while the associated 1σ errors are computed by AE following Gehrels (1986). For those sources that are not detected ($P_B > 2 \times 10^{-4}$) in one or two bands, we computed the 3σ upper limits with the *srcflux* tool of CIAO, that extracts source counts from a circular region, centered at the source position, that contains 90% of the PSF at 2.3, 1.4, and 3.8 keV in the full, soft, and hard bands, respectively. Background counts are extracted from an annular region located at the source location, that has an inner radius equal to the size of the source radius, and an outer radius five times the inner radius. The net source counts and their uncertainties are presented in Columns 8-10 of the main-catalog table (partially displayed in Table 4.4). The distributions of the source counts in the three bands are displayed in Fig. 4.6.

We used the net rates in the different bands to compute the hardness ratio (HR) for each source. The hardness ratio was computed as:

$$HR = \frac{H - S}{H + S}, \tag{4.6}$$

where H and S are the net rates (the ratio between the net counts and the relative exposure time) in the hard and soft bands, respectively. Errors are computed at the 1σ level following the method described in Lyons (1991). Upper and lower limits were computed using the 3σ net counts upper limits. For the 11 sources with only full-band detection we did not compute the HR.

We converted the count rate or upper limit on the count rate to the corresponding flux or flux upper limit in a given band, using the corresponding spectral response file and assuming a spectral power-law with $\Gamma = 1.4$ (i.e., the mean value derived CXB; Hickox & Markevitch 2006) modified by Galactic absorption ($N_H = 2.6 \times 10^{20}$ cm^{-2}). The adopted conversion factors are $CF = flux/CR = 1.44, 0.92, 2.03 \times 10^{-11}$ counts erg cm^{-2} for the full, soft, and hard bands, respectively. The distributions of the source fluxes in the three bands are displayed in Fig. 4.7.

4.3.2 Multi-wavelength Source Identifications

We searched for optical and NIR counterparts of the X-ray sources in our LBT/LBC and CHFT/WIRCam catalogs (see Morselli et al. 2014 and Balmaverde et al. 2017, respectively), using a likelihood-ratio matching technique similar to that described in §4.2.3. Again, a threshold value for the likelihood-ratio that maximizes the

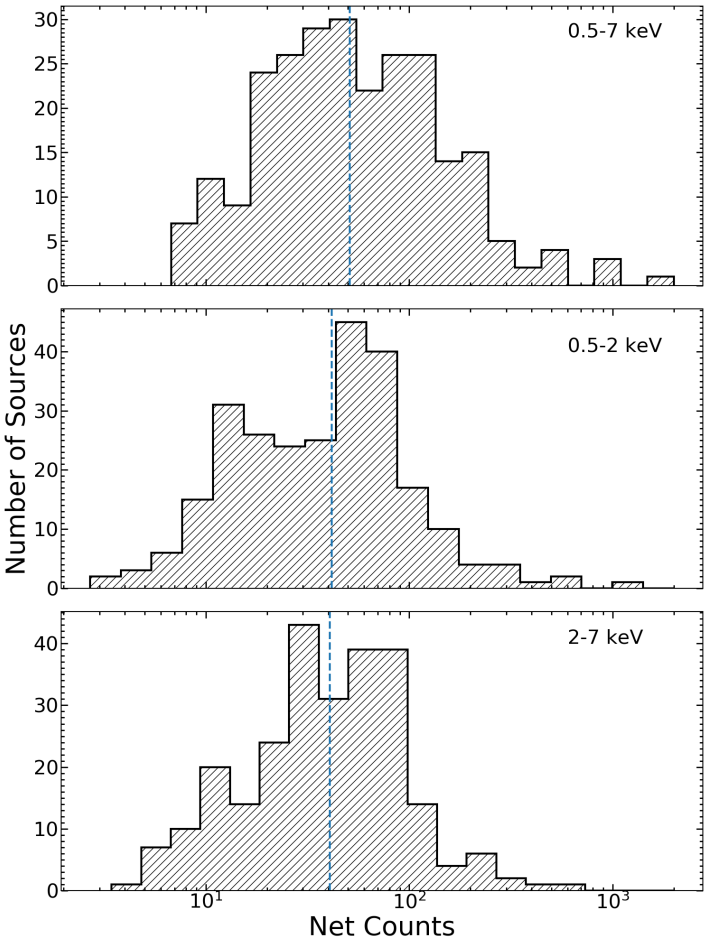

Figure 4.6: Net counts distributions for the sources detected in the full (top), soft (middle), and hard (bottom) bands. The cyan dotted vertical lines mark the medians of the distributions: 50.9, 41.5, and 40.7 net counts for the full, soft, and hard bands, respectively.

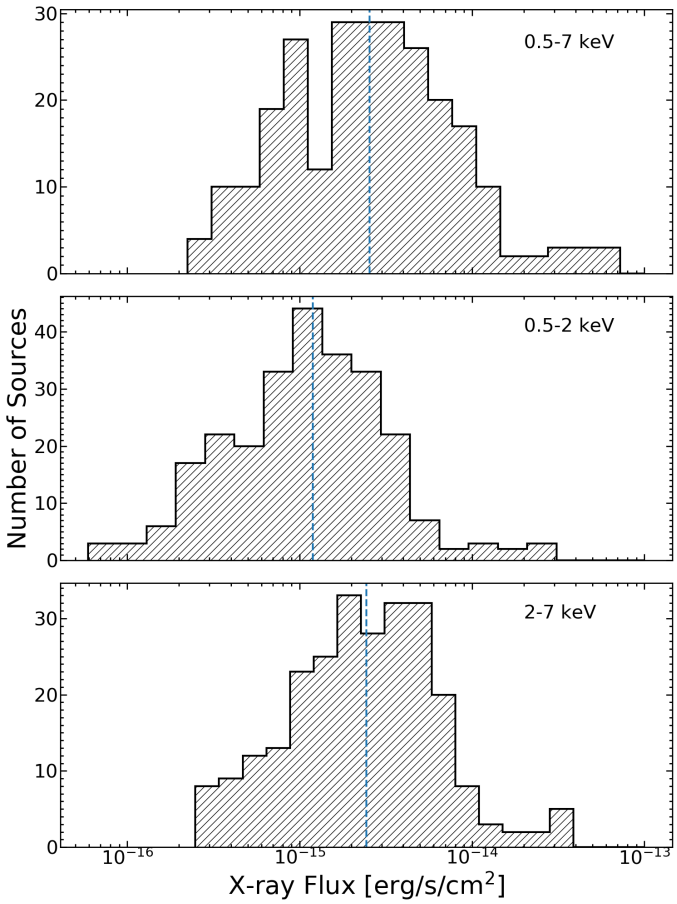

Figure 4.7: X-ray flux distributions for the sources detected in the full (top), soft (middle), and hard (bottom) bands. The cyan dotted vertical lines mark the medians of the distributions: 2.5, 1.2, 2.5×10^{-15} erg s^{-1} cm^{-2} for the full, soft, and hard bands, respectively. Sources with upper limits on the counts are not included in the plots.

(R+C)/2 was chosen ($LR_{th} = 1.06, 1.71, 2.41$ for the r, z, and J bands, respectively). For the X-ray sources with multiple counterpart candidates that satisfy our likelihood threshold we selected the candidate with the highest reliability level. In particular, we found 17, 7, and 3 sources with reliability $< 48\%$, $< 49\%$, and $< 18\%$ that have multiple counterpart candidates in the r, z, and J bands, respectively.

For the optical and NIR identifications we used the following three catalogs:

- The J1030+0524 Large Binocular Camera (LBC) z ad r bands catalogs with limiting AB magnitudes of 26.0 and 27.5, respectively (50% completeness limit at 5σ; Morselli et al. 2014). In Morselli et al. (2014) the z-band data were used as *master* images on which object detection was performed, then the photometric measurements were performed on the r images, resulting in a completeness limit in total magnitude of the images of 25.2, and 25.0 (5σ) for the z, and r images, respectively. We then performed a source detection on the r image to produce a r catalog with limiting AB magnitudes of 27.5.

- The J1030+0524 Wide-field InfraRed Camera (WIRCam) J-band catalog that contains 14770 sources down to $J_{AB} = 24.5$ (50% completeness limit at 5σ; Balmaverde et al. 2017).

We identified primary counterparts for 219 (85.5%) of the 256 main-catalog sources. We examined the 37 X-ray sources that lack counterparts, and manually assigned multi-wavelength matches to eight sources (with off-axis angle $> 1'$) for which the X-ray centroid computed by AE is too far away ($> 1''$) from the most likely optical counterpart to provide a LR value above our threshold, while the positional error is consistent with the optical counterpart. We also noticed that eight X-ray sources that have counterparts in the images that are missing in the catalogs, either due to their faintness, or because of photometric problems (e.g., they are blended with other sources). So, we added these eight faint sources to our optical catalogs, performing aperture photometry in the different optical bands, and assigned to the corresponding X-ray sources. There is also a source that is too close to a bright star for which is impossible to detect any optical counterpart to the X-ray emission. Among the detected sources there are further ten sources that were lacking an optical counterpart in one or two bands, for which we performed aperture photometry to obtain the missing band magnitudes. Finally, we found 20 sources (8%) with no optical counterparts. After these manual adjustments, we found primary counterparts for 235 (91.8%) of the 256 main-catalog sources. The distributions of the X-ray full-band fluxes versus LBT/LBC r-band magnitudes and CHFT/WIRCam J-band magnitudes for the main catalog sources are displayed in Fig. 4.8. The blue diagonal lines show constant X-ray to

r- or J-band flux ratios defined (similarly to Civano et al. (2012)) as:

$$log(f_X/f_{opt}) = log(f_X) + C_{opt} + m_{opt}/2.5 = -1, 0, +1 \quad (4.7)$$

where f_X is the X-ray full-band flux, m_{opt} is the magnitude at the chosen optical band, and C_{opt} is a constant which depends on the specific filter used in the optical observations. Considering the bandwidths and the effective wavelength of the LBC r-band and WIRCam J-band filters, we used $C_r = 5.41$ and $C_J = 5.96$. The yellow shaded region between the blue diagonal dashed lines ($-1 < log(f_X/f_{opt}) < +1$) in Fig. 4.8 represents the "classic locus" where AGN are expected to lay.

Finally, we noted that none of the high-z companion candidates we have detected in Morselli et al. (2014) and Balmaverde et al. (2017) are present in the X-ray catalog. Even performing direct photometry centered at the position of our companion candidates we saw no significant X-ray detection (except for a tentative 2σ detection of our candidate ID 23132; Balmaverde et al. 2017).

4.3.3 Main Catalog Details

We present the main J1030 source catalog in Table 4.4. The details of the table columns are given below.

1. Column 1: source sequence number (XID).

2. Columns 2 and 3: right ascension (R.A.) and declination (DEC) of the X-ray source, respectively. These positions were computed through the AE "CHECK_POSITIONS" procedure (§4.2.1). In the catalog we report the centroid position derived from the full-band. For sources not detected in the full-band we used the centroid positions derived either from the soft or from the hard band.

3. Column 4: positional error on the source centroid. This was computed as $\sigma = PSF_{Radius}/\sqrt{C}$ (Puccetti et al. 2009), where C are the net, background-subtracted, counts computed by AE, and PSF_{Radius} is evaluated with the estimate at the 90% encircled energy radius (at E = 1.4 keV) given by Equation 1 of Hickox & Markevitch (2006).

4. Column 5: off-axis angle in arcminutes computed as the angular distance between the position of the X-ray source and the average aim point of the J1030 field (10:30:27.50, +05:24:54.0).

5. Column 6: effective exposure time in ks taken from the full-band exposure map.

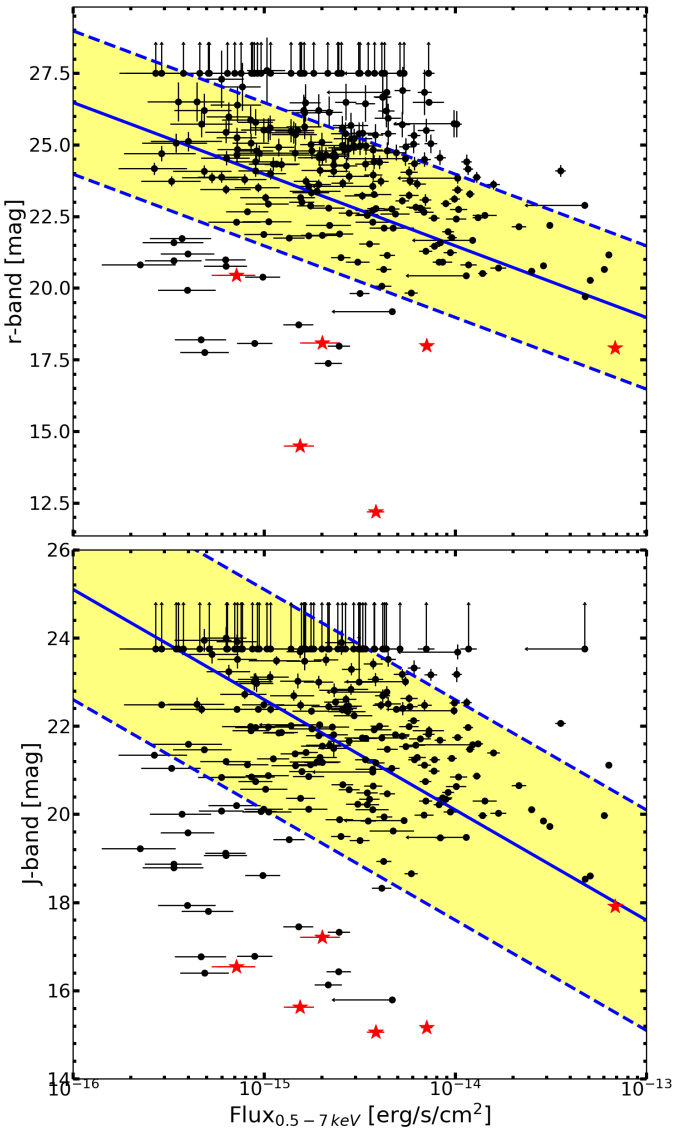

Figure 4.8: X-ray full-band flux vs. r-band (top panel), and J-band (bottom panel) magnitudes. Black dots represent the main catalog sources, while red stars represent the known stars of our catalog. The blue diagonal dashed lines show constant X-ray to r- or J-band flux ratios $log(f_X/f_{opt}) = -1, +1$, while the blue diagonal straight line shows $log(f_X/f_{opt}) = 0$. The yellow shaded region represents the "classic locus" of AGN.

6. Column 7: hardness ratio computed with Equation 4.6. Errors are computed at the 1σ level following the method described in Lyons (1991).

7. Columns 8-10: net counts computed by AE in the full (FB), soft (SB), and hard (HB) bands, respectively. Errors are computed according to Table 1 and 2 of Gehrels (1986) and correspond to the 1σ level in Gaussian statistics. For those sources that are not detected in one or two bands we provided upper limits at the 3σ confidence level (see §4.3.1).

8. Columns 11-13: binomial probability value P_B computed by AE in the full, soft, and hard bands. The condition that an X-ray source must satisfy to be included in the main catalog is $P_B < 0.0002$ in at least one of the three bands.

9. Columns 14-16: X-ray fluxes in the full, soft, and hard bands, respectively. Fluxes and relative errors were computed from the net rates and relative errors assuming a power-law model with $\Gamma = 1.4$, while for undetected sources 3σ upper limits are reported.

10. Columns 17 and 18: right ascension (R.A.) and declination (DEC), respectively, of the optical/NIR counterpart. When available we provide the centroid position from the z-band catalog, otherwise we provide either the J-band or the r-band centroid.

11. Column 19: positional offset between the X-ray source and optical counterpart in arcminutes.

12. Columns 20-22: counterpart magnitude in the r, z, and J bands, respectively.

13. Columns 23-25: counterpart likelihood-ratio value in the r, z, and J bands, respectively.

14. Columns 26-28: reliability value of the counterpart in the r, z, and J bands, respectively.

The catalog with all the info reported above is publicly available at: `http://www.oabo.inaf.it/~LBTz6/Catalogs_1030/`.

4.4 Cumulative log(N)-log(S) of the J1030 field

As a final step, we computed the cumulative number of sources, $N(>S)$, brighter than a given intrinsic flux (S) in each X-ray band. To this goal, we had to compute the sky-coverage (the area covered as a function of the flux limit, Ω) of the J1030

Table 4.4
Main J1030 source catalog properties

XID	R.A.	DEC	Pos Err ["]	Off-axis [′]	Exposure [ks]	HR	FB
(1)	(2)	(3)	(4)	(5)	(6)	(7)	(8)
1	10:30:24.96	+05:19:09.40	0.27	5.8	391.9	$-0.12^{+0.08}_{-0.08}$	$251.7^{+17.3}_{-16.3}$
2	10:30:32.82	+05:19:28.80	0.14	5.6	420.1	$-0.01^{+0.04}_{-0.04}$	$827.0^{+30.0}_{-29.0}$
3	10:30:23.77	+05:20:30.23	0.24	4.5	425.4	$-0.04^{+0.08}_{-0.08}$	$164.0^{+14.1}_{-13.1}$
4	10:30:30.11	+05:21:05.96	0.15	3.9	428.4	$-0.15^{+0.07}_{-0.07}$	$259.4^{+17.2}_{-16.2}$
5	10:30:22.19	+05:22:00.79	0.33	3.2	331.3	$-0.32^{+0.19}_{-0.19}$	$36.6^{+7.3}_{-6.2}$

field so to correct the incompleteness of our main-catalog. We computed our sky-coverage versus flux relation by dividing the number of output sources flagged as "good" in our simulations by the number of input sources as a function of flux and then multiplying for the total geometric area of the J1030 field covered by *Chandra*. The sky-coverage values we computed where then fitted with a spline to obtain a smooth monotonically increasing function. The sky coverage versus flux relation in the full, soft, and hard bands is plotted in Fig. 4.9. Once the sky coverage is known, the cumulative source number of sources was computed using the equation:

$$N(>S) = \sum_{i=1}^{N_S} \frac{1}{\Omega_i} \quad deg^{-2} \tag{4.8}$$

where N_S is the total number of detected sources in the field with fluxes higher than S, and Ω_i is the sky coverage associated with the flux of the i-th source. The three log(N)-log(S) relations in the three X-ray bands are reported in Fig. 4.10 and are obtained by interpolating the sky coverage value for each flux. The red points represent the cumulative number of sources of our J1030 field, while the simulated input sources coming from our mock catalog are represented with the blue line. For comparison, we also plotted the log(N)-log(S) relation found for the 4Ms (black line) and the 7 Ms *Chandra* Deep Field-South from Lehmer et al. (2012) Luo et al. (2017), respectively, and the one (green dashed line) found for the COSMOS field from Civano et al. (2016). From Fig.4.10 we conclude that our log(N)-log(S) is in general agreement with both our simulations and those from Lehmer et al. (2012), Luo et al. (2017), and Civano et al. (2016) in all the three X-ray bands.

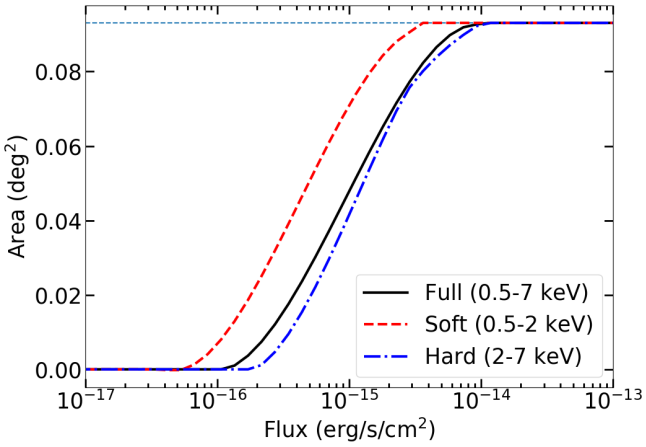

Figure 4.9: Sky coverage versus flux relation in the full (black solid line), soft (red dashed line), and hard (blue dash-dotted line) bands resulting from the three simulations. The horizontal cyan dotted line represent the sky area of our J1030 field (335 arcmin^2).

4.5 Summary

We have presented the X-ray source catalog for the deep *Chandra* survey in the SDSS J1030+0524 field, which covers a total area of 335 arcmin^2. The field has been observed with 10 *Chandra* pointings for a total exposure time of ∼479 ks. This is currently the fourth deepest X-ray survey in existence, after the *Chandra* Deep Fields North and South, and the AEGIS-X survey. We have achieved X-ray sensitivity with average flux limits over the central $\sim$ 1 arcmin^2 region of $\sim 1.3 \times 10^{-16}$, 6.3×10^{-17}, and 2.1×10^{-16} erg cm^{-2} s^{-1} in the full, soft, and hard bands, respectively.

The main *Chandra* source catalog contains 256 X-ray sources that were detected in up to three X-ray bands (full, soft, and hard) by *wavdetect* with a threshold of 1.e-4, and filtered by AE with a binomial probability threshold of 2×10^{-4}. We assess the binomial probability threshold by producing three X-ray simulations that mirror our *Chandra* observation, obtaining a completeness of 95% (full band), 97% (soft band), and 91% (hard band), while the reliability levels are 95% (full band), 96% (soft band), and 95% (hard band). Using a likelihood-based association method, we identified optical/NIR counterparts for 234 (91.4%) sources, while 21 sources (8%) have no optical counterparts. We computed the cumulative number of sources in each X-ray band finding that is in general agreement with both our simulations and those coming from the CDFS and COSMOS fields.

Finally, we asked and obtained LBT LUCI and MODS (16, and 36 hrs, respectively) multi-object spectroscopic observations of our X-ray sources with opti-

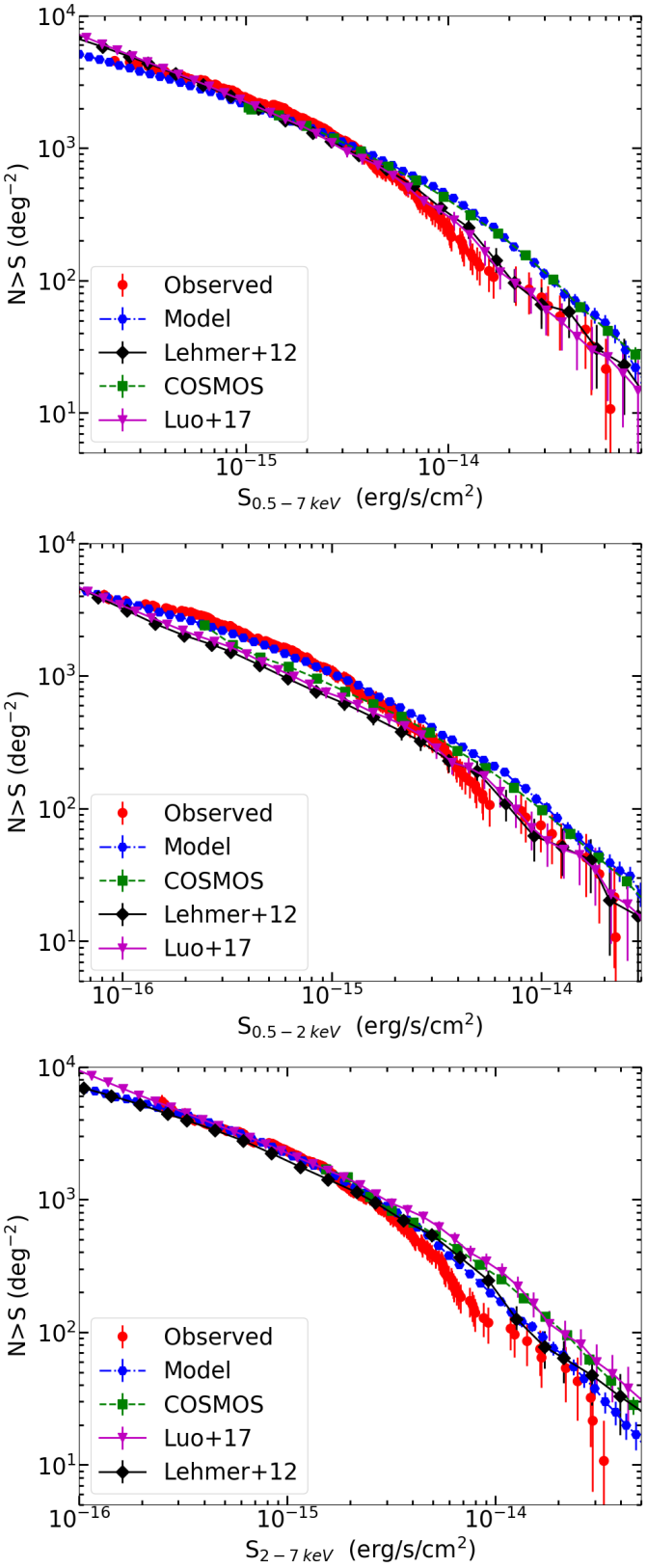

Figure 4.10: The cumulative number counts (number of sources brighter than a given flux) for the main source catalog (red dots) in the full (top), soft (middle), and hard (bottom) bands. The blue line represents our cumulative number of simulated input sources coming from our mock catalog. For comparison, we also plot the log(N)-log(S) relations found in the 4Ms *Chandra* Deep Field-South by Lehmer et al. (2012, black line), the 7Ms *Chandra* Deep Field-South by Luo et al. (2017, black dotted line), and in the COSMOS field by Civano et al. (2016, green dashed line).

cal counterparts to measure their redshifts. Based on the predictions of X-ray background synthesis models, corroborated by the results from other deep X-ray surveys, we expect a broad redshift distribution for our targets, peaking at $z = 1.0 - 1.5$, and significantly extending towards higher redshifts. About 80% of the X-ray sources with optical counterpart are brighter than $r_{AB} = 25$, which is the magnitude limit over which we expect to get robust redshift measurements. For a subset of optically fainter sources that are bright at NIR frequencies we will measure the redshift through NIR spectroscopy with LUCI. At the moment, the optical spectroscopic identification is in progress.

Chapter 5

Hunting for z $\sim$ 6 quasars

Quasars at $z > 5.5$ place strong constraints on black hole formation models (e.g., Volonteri et al. 2016) and are fundamental probes of the final phases of cosmological reionization (see Becker et al. 2015; Mortlock 2016, for recent reviews). About twenty years ago the first QSOs at $z > 5.6$ (i.e., within the first Gyr of the Universe) were discovered (Fan et al. 2000). After that, the search for high-z QSOs has undergone significant progress in recent years, thanks to the advent of wide-field (1000 deg^2 class) multi-band optical imaging surveys such as the Sloan Digital Sky Survey (SDSS; Fan et al. 2000), the Canada-France-Hawaii Telescope Legacy Survey (CFHTLS; Willott et al. 2010), the Panoramic Survey Telescope and Rapid Response System 1 (Pan-STARRS1; Bañados et al. 2016), and NIR imaging surveys such as the United Kingdom Infrared Telescope Infrared Deep Sky Survey (UKIDSS; Mortlock et al. 2011), the VISTA Kilo-degree Infrared Galaxy survey (VIKING; Venemans et al. 2013), the VLT Survey Telescope ATLAS (VST-ATLAS; Carnall et al. 2015), the Dark Energy Survey (DES; Reed et al. 2015), and the Hyper Suprime-Cam survey (HSC; Matsuoka et al. 2016). As reported at the beginning of Chapter 2, $\sim$ 300 QSOs have been discovered so far at redshift $z > 5.5$ thanks to the surveys mentioned above. In particular, five QSOs have been discovered at $z > 7$, the two most distant being at $z = 7.09$ (Mortlock et al. 2011), and $z = 7.54$ (Bañados et al. 2018).

In this chapter we present our preliminary results on the search for high-redshift AGN companions around luminous known $z > 5.5$ QSOs. In particular, we report the discovery of 25 high-redshift companion candidates that have been found in the Pan-STARRS1 (hereafter PS1) catalog. In §5.1 we present the high-z QSO candidate selection and the results. Future prospects, including the plans for the spectroscopic follow-up of the companion candidates, are presented in §5.2.

5.1 QSO candidate selection

As explained in 1.6.1, the existence of SMBHs, with $M_{BH} \sim 10^8 - 10^{10}\, M_\odot$ up to $z \sim 7.5$, and hence formed in less than 1 Gyr, poses a great challenge to modern astrophysics. There is general agreement that early massive BHs form in overdense environments, that may extend up to 10 physical Mpc (pMpc), and host large gas quantities (Overzier et al. 2009; Dubois et al. 2013; Costa et al. 2014; Barai et al. 2018). According to simulations, the fields around high-redshift QSOs are expected to show galaxy overdensities (galaxy companions that lay in the same structure of the main QSO), which probably represent the progenitors of the most massive clusters in the local Universe (Springel et al. 2005). In the past decades, large efforts have been made to find overdense regions in fields as large as 2×2 pMpc around $z \sim 6$ QSOs (e.g., Stiavelli et al. 2005; Husband et al. 2013; Bañados et al. 2013; Simpson et al. 2014; Mazzucchelli et al. 2017), but the results were inconclusive. Some of these works ascribed the lack of detection of overdensities at very high-z to the strong ionizing radiation coming from the QSO that may prevent star formation in its vicinity (but see also Habouzit et al. 2019 regarding the variance in galaxy number counts around high-z QSOs). The presence of strong gas jets and/or radiation feedback extending up to few hundreds of kpc at $z = 6$ is, in fact, a common feature in modern simulations of BHs formation (Costa et al. 2014; Barai et al. 2018). The above considerations are now motivating the scientific community to extend the search for galaxy overdensities around high-z QSOs at larger scales (> 2 pMpc) with promising results (Morselli et al. 2014; Balmaverde et al. 2017), but high-z galaxy candidates are too faint ($mag_z = 25 - 26$) to detect with optical/NIR surveys, while large area time-consuming follow-up observations are required. On the other hand, the search for brighter ($mag_z = 19 - 22$) AGN around massive $z \sim 6$ QSOs, whose presence in overdense region is also predicted by simulations, is easier to achieve with current optical/NIR surveys, and can provide a more feasible way to pinpoint overdensities at $z \sim 6$. However, the lack of evidences for $z \sim 6$ AGN companions (but see Connor et al. 2019 for a tentative $z \sim 6$ AGN companion detection) recently motivated us to hunt for fainter AGN at larger scales (20 pMpc) than what was done in previous works in the fields of high-z QSOs.

Following the predictions that early SMBHs formed at the center of overdense regions surrounded by fainter galaxy and QSO companions, we searched for high-z AGN companions coming from the Pan-STARRS1 Data Release 1 (PS1-DR1) that fall inside circular areas of 1 deg radius (~ 20 pMpc at $z = 6$) around 75 known QSOs (at $z = 5.6 - 6.3$) discovered in the PS1 by Bañados et al. (2016). Pan-STARRS is a system for wide-field astronomical imaging developed and operated by the Institute for Astronomy at the University of Hawaii. The PS1 survey used a 1.8 meter telescope and its 1.4 Gigapixel camera to image the sky in five broadband

filters (g, r, i, z, y), with a Field of View (FoV) of 7 square degrees. The mean 5σ point source limiting sensitivities of PS1 in the stacked 3π Steradian Survey in g, r, i, z, y are 23.3, 23.2, 23.1, 22.3, 21.4, respectively. The large area surveyed by PS1 down to these source limiting sensitivities is the best choice to hunt for high-z QSOs. Quasars at redshift $z > 5.5$ are observationally characterized by very red ($i - z > 2.2$) color and blue continuum that extends up to the WISE bands (i.e., $z - y < 0.5$, $-0.2 < W1 - W2 < 0.85$, and $-0.7 < y - W1 < 2.2$). They are very faint or completely undetected in the i band due to the optically thick Lyα forest at these redshifts, causing most of the light coming from wavelengths $\lambda_{rest} < 1216$ Å to be absorbed. The main contaminants of $z \sim 6 - 7$ QSO searches are brown dwarfs (BDs), especially late-type M, L, and T dwarfs, which can have optical colors similar to quasars, but are much more abundant. We crossed matched our preliminary catalog ($\sim$ 11 M sources) with the M dwarf catalog of West et al. (2011), and the L and T dwarf catalog based on the list compiled by Mace (2014), with additions from Lodieu et al. (2014), Marocco et al. (2015), and Best et al. (2015), using a matching radius $r = 2''$. With these cross-matches we discarded the known BDs from our catalog. Similarly, we crossed matched and filtered our catalog with the already known QSOs. Then, we followed a filtering procedure that is similar to the one adopted by Bañados et al. (2016):

1. We excluded those sources for which the Image Processing Pipeline (Magnier 2006; Magnier 2007) flagged the result as suspicious (see Table 6 of Bañados et al. 2014).

2. We divided our preliminary catalog into 75 sub-catalogs (one for each of our 75 known QSOs) and produced color-color diagrams as the one shown in Fig. 5.1. We then used this kind of diagrams to select our high-z QSO candidates, as described in §5.1.1.

3. At the position of each candidate, we applied forced aperture photometry in the single-epoch images to remove artifacts that appeared as very bright sources in some of the individual exposures and did not appear in others.

4. We matched the candidate list to the 2MASS, UKIDSS, UHS, VHS, and Decals catalogs to eliminate BDs contaminants that are expected to be brighter in the J-band compared to the high-z QSOs. We also matched the candidate list to the WISE catalog to prioritize our candidates for future spectroscopic follow-ups.

5. Finally, we asked and obtained NIR follow-up photometry of our high-priority candidates with no J-band magnitude, using the New Technology Telescope, to reject possible BDs contaminants.

5.1.1 The filtering method

After removing those sources with unreliable measurements according to the Image Processing Pipeline, we divided the preliminary catalog into 75 sub-catalogs, grouping together the objects according to the closest known QSO. Then, for each high-z known QSO we produced a $i - z$ versus $z - y$ diagram using the sources within deg^2 from the central QSO. As an example, in Fig. 5.1 we report one of the 75 color-color diagrams produced using the objects around the $z = 5.96$ QSO PSOJ333.9859+26.1081.

To select the candidates, we used the broad-band dropout technique that was already performed by Bañados et al. (2016), which has proven to be very effective in selecting more than 100 $z > 5.5$ QSOs, but searching for fainter objects ($S/N(z) > 5$) than those sampled in past studies. Since we were searching for AGN companions around $5.7 \leq z \leq 6$ QSOs, we restricted our selection method to the upper left region of Fig. 5.1 (i.e., $z-y < 0.5$ and $i-z > 2.2$, that is enclosed inside the dotted box in the figure), where $5.7 \leq z \leq 6$ QSOs (i-band dropouts) are supposed to lay. We used the difference between the aperture (mag_{ape}) and PSF (mag_{PSF}) magnitudes in the z and y bands as a proxy to remove extended sources: $|z_{ape} - z_{PSF}| < 0.3$, and $|y_{ape} - y_{PSF}| < 0.3$. We also removed sources that were detected in the g and r bands, keeping those with signal-to-noise ratio $SNR(g, r) < 3$ or with $r-z > 2.2$, while we relaxed the detection threshold for the z-band ($SNR(z) \geq 5$) compared to Bañados et al. (2016) ($SNR(z) \geq 10$). This procedure was performed for each of the 75 known QSOs, producing 75 sub-lists of possible high-z candidates.

It is possible that a fraction of our candidates were moving objects, spurious objects, or artifacts that appeared as very bright sources in some of the individual exposures and did not appear in others. For this reason, we performed forced aperture photometry on all individual single epoch g, r, and z band images by using a circular aperture with $r = 4''$ (the one also used to derive the aperture magnitudes provided by the PS1-DR1). We flagged the images in which the SNR at the position of the candidate was $SNR(g, r) > 3$ or $SNR(z) < 5$. The sources that did not satisfy the measured SNR criteria were then discarded.

As a third step, we matched our sources with several public infrared surveys to extend and verify the photometry of the quasar candidates. The extra information were used to either remove foreground interlopers or prioritize targets for possible subsequent spectroscopic follow-ups. We cross match our candidates (with a cross-matching radius $z = 3''$) with the 2MASS, UKIDSS, VHS, UHS, Decals DR5 and DR6 catalogs to remove bright cool contaminants (manly dwarfs that are not yet discovered). In particular, we required our candidates to be undetected or to have $y - J < 1$, where the y-band magnitude is coming from the PS1 and the J-band magnitude from the NIR surveys mentioned above. We also cross matched our

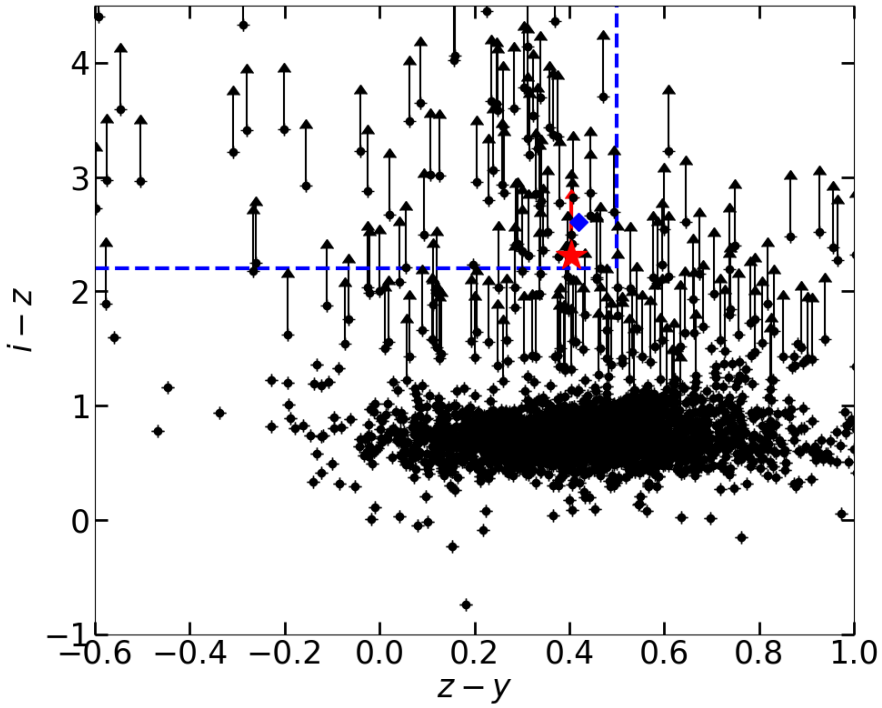

Figure 5.1: Color-color diagram showing the criteria used to select $z \sim 6$ QSO candidates (dashed blue lines) around the $z = 6.03$ QSO PSOJ333.9859+26.1081. Black points are the sources around PSOJ333.9859+26.1081 ($r < 1$ deg) coming from the PS1-DR1 catalog after removal of: known QSOs, BDs, extended sources, suspicious sources according to Image Processing Pipeline, sources with $SNR(g, r) > 3$, and with $SNR(z) < 5$ (see §5.1 for the filtering details). For display purposes we did not report the errors on the single dots, while we displayed the 3σ upper limits. The blue diamond represents the $z = 6.03$ PSOJ333.9859+26.1081 that was discovered by Bañados et al. 2016, while the red star represents the high-z AGN candidate PSO334.17123+26.75792.

sources with the WISE catalog to prioritize our candidates: objects with $SNR > 3$ in W1 and W2 bands (3.4 and 4.6 μm, respectively) were assigned a higher priority if their colors fulfilled the additional criteria $-0.2 < W1 - W2 < 0.85$ and $-0.7 < y - W1 < 2.2$. Also for objects with $SNR > 3$ in W3-band (12 μm) we assigned a higher priority if $W2 - W3 > 0$. Objects undetected in the WISE catalog or with $SNR < 3$ in W1 or W2 bands were assigned an intermediate priority (possible high-z AGN with few data points to preform SED fitting), while the remaining candidates were given a low priority (more likely non AGN). At the end of this process we obtained a total of 27, 530, and 174 candidates with high, intermediate, and low priority, respectively, around our 75 high-z QSOs.

Since many of our high-priority candidates had no J-band magnitudes, we obtained deep NIR follow-up imaging, which provides essential information to efficiently separate cool dwarfs (our main contaminants) from high-redshift QSOs. In December 2018 and July 2019, two observing runs at the New Technology Telescope (NTT/SOFI; Moorwood et al. 1998) were granted to our group to obtain deep J-band follow-up imaging of high-z QSO candidates, that allowed us to efficiently separate cool dwarfs (our main contaminants) from high-redshift QSOs, that show flat spectra in the observed range $\lambda \sim 1.0 - 1.2\,\mu m$ ($y - J < 1$). Again, candidates were considered foreground interlopers if they had $y - J > 1$. In the end, we found 25 high-priority AGN companion candidates ($mag_z = 19.7 - 21.2$) around 18 out of the 75 high-z QSOs: the separation range between the candidates and the main QSOs is $6' - 57'$ ($\sim 2 - 20$ pMpc at $z \sim 6$). Finally, to prove the robustness of our selected sample, we derived the photometric redshifts by fitting the candidate SEDs with the $z \sim 6$ QSOs composite spectrum (taken from Bañados et al. 2016), and we found that they are consistent with those derived for the main QSOs ($z = 5.6 - 6.3$). As an example, we report in Fig. 5.2 the SED fitting of the AGN candidate PSO334.17123+26.75792 with derived photometric redshift of $z = 6.08 \pm 0.07$ (1σ errors). For high-z overdense structures extended up to ~ 20 pMpc we expect to find AGN companions inside $\Delta z \sim 0.3$ from the main QSO redshift. In Fig. 5.3 we summarize the procedure adopted to select our high-z candidates.

5.2 Results and future prospects

As reported in §5.1.1, 25 high priority candidates survived our filtering method. In Table 5.1 we report the main information regarding these objects that are distributed around 18 known $z \sim 6$ QSOs. These candidates need spectroscopic observations to confirm or reject their high-redshift origin, and we submitted an optical and NIR spectroscopic proposal (P.I. Nanni) with EFOSC and SOFI at the New Technology Telescope to answer this final question. If they will be confirmed

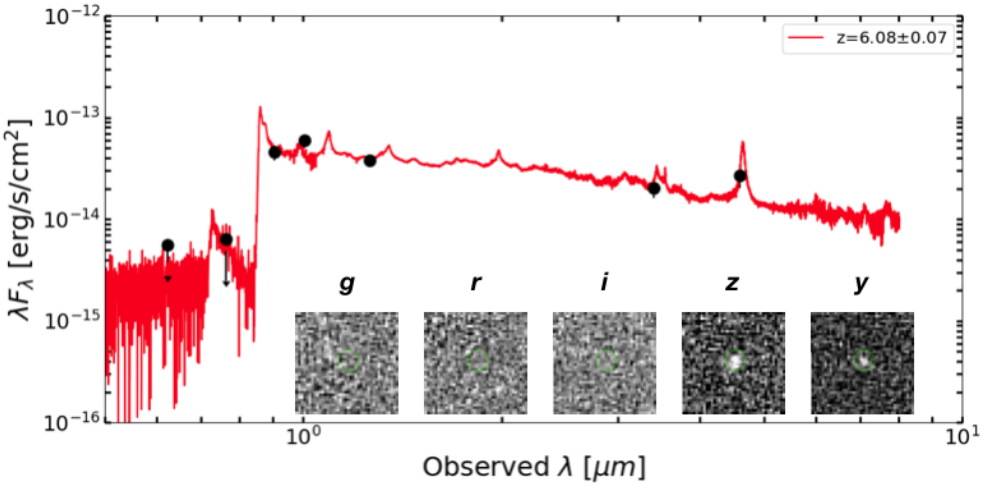

Figure 5.2: Spectral energy distribution of one of our targets, PSO334.17123+26.75792, companion candidate of the $z = 6.03$ QSO PSOJ333.9859+26.1081. Black dots show the r, i, z, y band photometry from the PS1, the J-band photometry from ESO/NTT, and the W1, W2 band photometry from WISE. The red line shows the best fit model obtained using the $z \sim 6$ QSOs composite spectrum taken from Bañados et al. 2016. The best fit redshift solution is $z = 6.08 \pm 0.07$ (1σ errors). In the bottom we show $10'' \times 10''$ images of the candidate in the PS1 filters. Green circles with $r = 0.5''$ are centered on the candidate position.

as high-z QSO companions, they could pinpoint the possible presence of an overdense region around known QSOs, that should be investigated with future studies, similarly to what we have done for J1030+0524 (Morselli et al. 2014; Balmaverde et al. 2017).

Finally, to complete this study of high-z AGN companion candidates, the sources flagged as intermediate and low priority according to our selection method will be also investigated. In principle, we should follow the same approach adopted for high-priority sources, applying for NIR photometric follow-ups to select the best candidates or reject the contaminants. However, it is impractical to re-observe all such candidates, so alternative approaches should be adopted to filter our candidates before asking for future photometric follow-ups. In particular, we aim at developing a Markov-Chain Monte Carlo (MCMC) SED fitting method, based to what was done by Reed et al. (2017*b*) to prioritize their candidates. The main idea is to fit both high-z QSO SED (i.e., taken from Bañados et al. 2018) and BD SED models (i.e., using polynomial fits of the BD colors from Skrzypek et al. 2015) to the photometric data we have for our candidates, and discriminate between the two model classes using χ^2 minimization. Candidates are first ranked based only on their quasar reduced χ^2 values, with the smallest reduced χ^2 sources having the highest ranking. Following this ranking, we can compare the quasar reduced χ^2 values to those obtained from a brown dwarf fit to the photometry. Objects

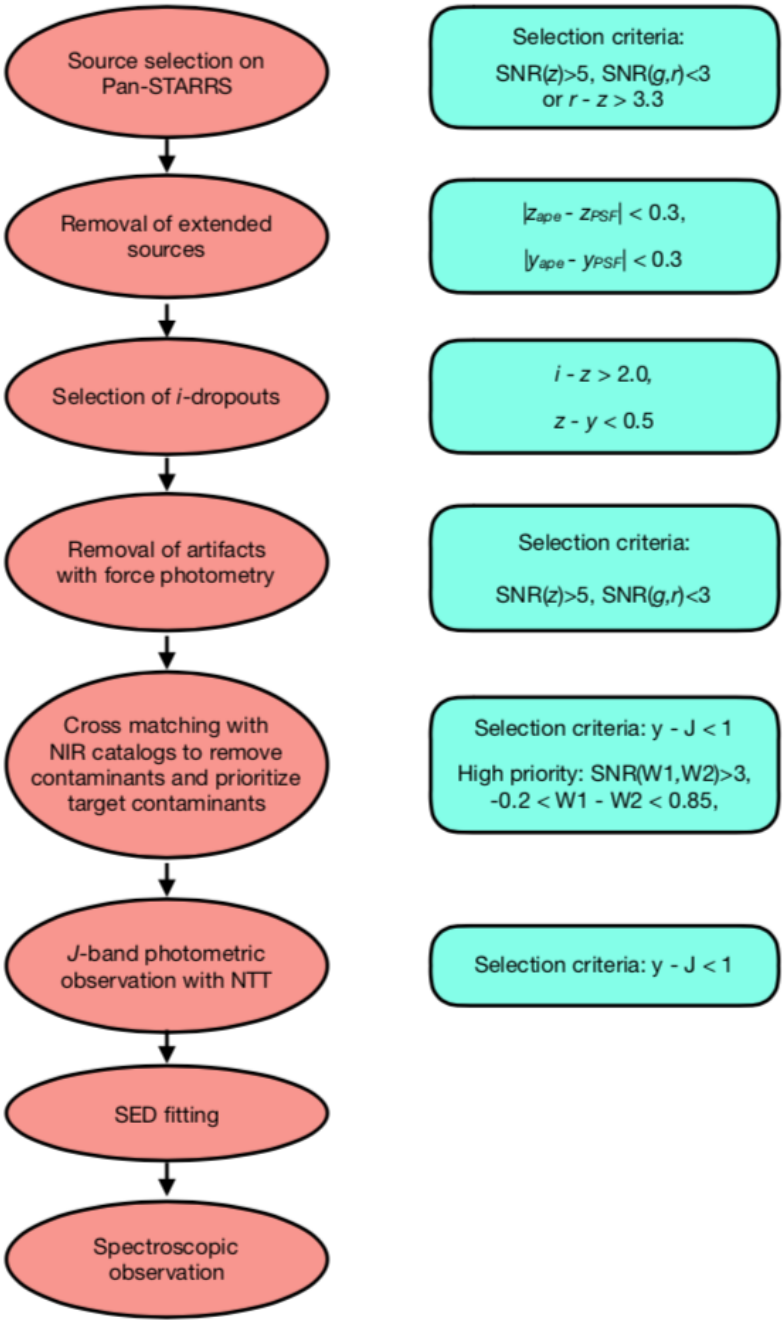

Figure 5.3: Flowchart of the high-z AGN candidate selection.

Table 5.1
Optical properties of the 25 high-z candidates found by our group

Candidate	RA (J2000)	Dec (J2000)	Separation [°]	Central QSO	z	z_{mag}	y_{mag}	J_{mag}
(1)	(2)	(3)	(4)	(5)	(6)	(7)	(8)	(9)
PSO003.00690-06.72792	00:12:02	-06:43:41	0.94	PSOJ002.1073-06.4345	5.93	20.80 ± 0.01	20.40 ± 0.20	20.69 ± 0.05
PSO004.36267-24.59902	00:17:27	-24:35:56	0.51	PSOJ004.8140-24.2991	5.68	21.08 ± 0.08	20.88 ± 0.19	19.97 ± 0.03
PSO005.05873-25.13329	00:20:14	-25:08:00	0.86	PSOJ004.8140-24.2991	5.68	20.70 ± 0.17	20.30 ± 0.16	20.13 ± 0.04
PSO017.16397-12.03501	01:08:39	-12:02:06	0.10	PSOJ017.0691-11.9919	5.95	21.18 ± 0.09	20.72 ± 0.19	19.95 ± 0.06
PSO021.72363-25.67974	01:26:54	-25:40:47	0.34	PSOJ021.4213-25.8822	5.79	20.10 ± 0.04	19.64 ± 0.18	19.96 ± 0.04
PSO029.30546-29.26910	01:57:13	-29:16:09	0.26	PSOJ029.5172-29.0886	5.96	20.39 ± 0.18	20.25 ± 0.16	20.66 ± 0.06
PSO049.99792-27.06543	03:20:00	-27:03:56	0.81	PSOJ049.2934-26.5543	5.94	20.72 ± 0.13	20.25 ± 0.17	19.96 ± 0.02
PSO049.16869-26.62788	03:16:40	-26:37:40	0.13	PSOJ049.2934-26.5543	5.94	20.42 ± 0.08	20.04 ± 0.18	19.94 ± 0.03
PSO128.03860+02.99301	08:32:09	+02:59:35	0.76	PSOJ127.2817+03.0657	5.85	19.73 ± 0.02	19.33 ± 0.04	18.61 ± 0.01
PSO135.88396+15.49990	09:03:32	+15:30:00	0.89	PSOJ135.3860+16.2518	5.63	20.44 ± 0.08	20.00 ± 0.06	19.2 ± 0.01
PSO135.84593-14.07432	09:03:23	-14:04:28	0.24	PSOJ135.8704-13.8336	5.91	20.85 ± 0.16	20.58 ± 0.27	20.26 ± 0.04
PSO135.91353-12.98085	09:03:39	-12:58:51	0.85	PSOJ135.8704-13.8336	5.91	20.97 ± 0.06	20.49 ± 0.15	19.63 ± 0.02
PSO210.87058-11.86130	14:03:29	-11:51:41	0.15	PSOJ210.8722-12.0094	5.84	21.13 ± 0.16	20.92 ± 0.191	20.37 ± 0.02
PSO211.69821-11.98877	14:06:48	-11:59:20	0.81	PSOJ210.8722-12.0094	5.84	21.01 ± 0.19	20.87 ± 0.19	20.83 ± 0.07
PSO213.26706-16.14703	14:13:04	-16:08:49	0.95	PSOJ212.2974-15.9865	5.83	20.95 ± 0.20	20.78 ± 0.17	20.01 ± 0.18
PSO213.81335-12.55033	14:15:15	-12:33:01	0.93	PSOJ213.7329-13.4803	5.78	20.87 ± 0.11	20.44 ± 0.14	20.08 ± 0.07
PSO213.63859-14.27244	14:14:33	-14:16:21	0.80	PSOJ213.7329-13.4803	5.78	21.23 ± 0.12	20.78 ± 0.18	20.95 ± 0.26
PSO214.91463+26.66423	14:19:40	+26:39:51	0.48	PSOJ215.4303+26.5325	6.27	20.56 ± 0.17	20.10 ± 0.21	20.25 ± 0.19
PSO216.61077-16.87529	14:26:27	-16:52:31	0.95	PSOJ217.0891-16.0453	6.15	21.03 ± 0.08	20.78 ± 0.20	19.91 ± 0.08
PSO217.79232-06.67782	14:31:10	-06:40:40	0.74	PSOJ217.9185-07.4120	6.14	21.04 ± 0.26	20.57 ± 0.12	19.76 ± 0.14
PSO229.17434+21.81042	15:16:42	+21:48:38	0.73	PSOJ228.6871+21.2388	5.92	21.19 ± 0.17	20.882 ± 0.19	21.0 ± 0.13
PSO333.28889+26.43989	22:13:09	+26:26:24	0.71	PSOJ333.9859+26.1081	6.03	20.80 ± 0.18	20.61 ± 0.19	20.8 ± 0.10
PSO333.61342+26.35883	22:14:27	+26:21:32	0.42	PSOJ333.9859+26.1081	6.03	20.96 ± 0.05	20.48 ± 0.17	20.21 ± 0.18
PSO334.17123+26.75792	22:16:41	+26:45:29	0.67	PSOJ333.9859+26.1081	6.03	21.06 ± 0.18	20.65 ± 0.16	20.89 ± 0.10
PSO340.28525-19.45946	22:41:08	-19:27:34	0.80	PSOJ340.2041-18.6621	6.01	20.97 ± 0.15	20.49 ± 0.17	20.0 ± 0.05

(1) Candidate name. (2) and (3) right ascension and declination, respectively, of the candidate. (4) Separation in degree from the central known high-z QSO. (5) Name of the central high-z QSO. (6) Redshift of the central high-z QSO. (7), (8), (9) AB magnitudes of the candidate in the z, y, and J band, respectively. Errors are reported at the 1σ level.

where the reduced χ^2 to be a brown dwarf is comparable to or higher than that to be a quasar are removed, filtering our candidates for future photometric and spectroscopic follow-ups.

Chapter 6

Discussion and conclusions

In this thesis, we investigated the physical and environmental properties of early accreting SMBHs. In particular, we provided a systematic analysis and study of all the X-ray data available for $z \sim 6$ QSOs to derive the general properties of accretion onto SMBHs in the early Universe. Furthermore, we investigated the X-ray field around $z \sim 6$ QSO SDSS J1030+0524 to search for AGN in the galaxy overdensity around the QSO, that was tentatively observed by our group in the past. This was finally complemented by the hunt for high-z AGN companions around luminous $z \sim 6$ QSOs to find new overdense fields in the primordial Universe.

In Chapter 2, we have studied the X-ray properties of high-redshift ($z \geq 5.5$) QSOs and investigated the formation and growth of early SMBHs. Optical and NIR observations showed that these QSOs are evolved systems with large black hole masses ($10^{8-10}\,M_{\odot}$), large amount of gas and dust, and intense star formation in their host galaxies, while their SEDs and the rest-frame optical/UV spectra have not significantly evolved over cosmic time. To investigate also the X-rays properties and compare them with those from lower redshift QSOs, we made a complete and uniform study of the X-ray properties of the most-distant quasars at $z > 5.5$, starting from a parent sample of 198 spectroscopically confirmed QSOs at high-redshift and considering the 29 objects that have been observed by *Chandra*, XMM-*Newton*, and *Swift*-XRT. In particular, we found that only 18 of them are detected in the full X-ray band, while all the others were serendipitously observed at very large off-axis angles, where the detector sensitivity is lower. Among the 18 X-ray detected QSOs, five sources are detected with a sufficient counting statistic (> 30 net counts) that allowed us to fit their spectra with photon index free to vary. For these quasars we obtained values of the photon index $\Gamma \sim 1.6 - 2.4$ consistent with those reported in the literature.

For those sources that are detected with low counting statistics (< 30 net counts), we performed spectral stacking analysis and derived their mean photon index. We divided our 15 Chandra detected sources into two redshift bins,

$5.7 \leq z \leq 6.1$ (10 sources) and $6.2 \leq z \leq 6.5$ (5 sources), and fit the stacked spectra with a power-law model. From the spectral fits, we found that the photon indices are consistent with the values found for lower redshift luminous QSOs ($\Gamma = 1.92^{+0.28}_{-0.27}$ for the first stacked sub-sample and $\Gamma = 1.73^{+0.43}_{-0.40}$ for the second one), confirming that there is no significant change in Γ with cosmic time over the redshift range $z = 1.0 - 6.4$. Recently, we confirmed similar results also for $z \geq 6$ QSOs, even if the mean measured photon indices are slightly steeper for sources with < 30 net counts. This means that, similarly to optical properties, also the X-ray spectral properties of luminous QSOs do not significantly evolve over cosmic time. Combining our sample with literature works, we also confirmed that, by using a statistically larger sample, the α_{ox} parameter depends on UV monochromatic luminosity. We then concluded that, the X-ray-to-optical flux ratios of luminous AGN have not significantly evolved up to $z \sim 6$, suggesting that the interplay between the accretion disk and the hot corona, that are responsible for the UV/optical and X-ray emission, respectively, is already in place when our Universe was less than 1 Gyr. Furthermore, the upper limits to the mean column density that we derived from the stacking analysis showed that these luminous high-redshift QSOs are not significantly obscured ($N_H < 5.0 \times 10^{23}$ cm^{-2}), as expected from their optical classification as Type 1 AGN.

In Chapter 3, we reported on the ~ 500 ks *Chandra* observation of the QSO SDSS J1030+0524, that is the deepest X-ray observation of a $z \sim 6$ QSO. The QSO has been detected with ~ 125 net counts in the full band with no evidence of either significant spectral or flux variability during the *Chandra* observations. Moreover, SDSS J1030+0524 appeared to be a "classic" QSO, since its X-ray spectrum is well fit by a single power-law with $\Gamma = 1.81 \pm 0.18$, that is consistent with the mean value found for luminous AGN at any redshift, while no evidence is found for significant absorption nor for other additional spectral features. We built the QSO SED and showed that is one of the best sampled for at $z > 6$ QSO. Similarly to what is normally observed in $z \sim 6$ QSOs, the SED of SDSS J1030+0524 is consistent with the mean SED of luminous QSOs of lower redshifts at UV to NIR rest-frame wavelengths. However, it differs in the FIR and sub-millimeter bands from what is found for other QSOs at similar redshift, since it is not detected. This difference may suggest that SDSS J1030+0524 is in a more evolved state (i.e., with quenched SFR) than other luminous QSOs at that redshift.

The comparison between the QSO X-ray spectral properties derived from our *Chandra* data with those obtained from a past XMM-*Newton* observation revealed that the QSO significantly varied. The full band flux decreased by a factor of 2.5 from the XMM-*Newton* to the *Chandra* observations and the spectrum became flatter ($\Delta\Gamma \approx -0.6$). We showed that these variations are not related to calibration issues and discussed the possibility that the hardening of the spectral slope is

intrinsic and could be related to either a variation of the accretion rate, or a variation of the obscuration level along the line of site. The low detection statistics does not allow us to discriminate among the proposed scenarios regarding the X-ray variability that is why, in the next future, *Chandra* and XMM-*Newton* monitoring of SDSS J1030+0524 may provide additional information on the QSO variability, and will greatly help developing the science cases for future X-ray missions, such as *Athena* and *Lynx*, that will shed new light on the high-redshift frontier.

Thanks to our deep *Chandra* observation, we detected significant diffuse X-ray emission that extends for $30'' \times 20''$ southward the QSO, with a $S/N = 5.9$, hardness ratio of $HR = 0.03^{+0.20}_{-0.25}$, and soft band flux of $f = (1.1 \pm 0.3) \times 10^{-15}$ erg s^{-1} cm^{-2}. We discussed several scenarios regarding the origin of this diffuse emission, and verified that an implausibly high surface density of undetected point-like X-ray sources would be required to reproduce entirely the observed flux while. In one of the most intreaguing scenarios, the diffuse X-ray emission may probe the feedback produced by SDSS J1030+0524 on its close environment. In that case, if the diffuse emission is thermal, the gas should have a temperature of $T \geq 10$ keV, and extend asymmetrically for about 150 physical kpc from the QSO, in agreement with simulations of early BH formation. In addition, supposing that SDSS J1030+0524 is producing a relativistic jet, this would be best probed in the X-rays rather than in the radio band, as the electron energy losses would be dominated by IC scattering of the strong CMB photon field, rather than by synchrotron emission. The energetics, scales and spectral hardness of the observed X-ray emission would also be consistent with this interpretation. However, we recently discovered at least eight galaxy members forming an overdensity with spectroscopic redshift $z = 1.687 - 1.699$, including a FRII galaxy at $z = 1.699$. The eastern radio lobe produced by the FRII lays in the diffuse X-ray emission, and four star-forming galaxies in the overdensity are distributed in an arc-like shape at the edge of this diffuse emission. This strengthen the idea that the diffuse X-rays originate from an expanding bubble of gas that is shock heated by the FRII jet, and that star formation is promoted by the compression of the cold interstellar medium of the galaxies around the bubble, which may be remarkable evidence of positive AGN feedback on cosmological scales.

In Chapter 4 we have presented the X-ray source catalog for the deep *Chandra* survey in the SDSS J1030+0524 field, which covers a total area of 335 arcmin^2. This is currently the fourth deepest X-ray survey in existence, after the *Chandra* Deep Fields North and South, and the AEGIS-X survey. The main *Chandra* source catalog contains 256 X-ray sources that were detected in up to three X-ray bands (full, soft, and hard) by *wavdetect* with a threshold of 1.e-4, and filtered by AE with a binomial probability threshold of 2×10^{-4}. We assess the binomial probability threshold by producing three X-ray simulations that mirror our *Chandra*

observation, obtaining a completeness of 95% (full band), 97% (soft band), and 91% (hard band), while the reliability levels are 95% (full band), 96% (soft band), and 95% (hard band). Using a likelihood-based association method, we identified optical/NIR counterparts for 234 (91.4%) sources, while 21 sources (8%) have no optical counterparts. We computed the cumulative number of sources in each X-ray band finding that is in general agreement with both our simulations and those coming from the CDFS and COSMOS fields. Finally, we asked and obtained LBT LUCI and MODS multi-object spectroscopic observations of our X-ray sources to measure their redshifts. The data have been taken and the optical spectroscopic identification is now in progress.

Finally, in Chapter 5 we reported the discovery of 25 AGN companion candidates around 18 $z \sim 6$ QSOs coming from the PanSTARRS-DR1 survey. These candidates have been selected among $\sim$ 11 millions PS1 sources that are 1 deg from 75 known high-z QSOs using a filtering pipeline that was already used to find the majority of the > 300 detected $z \geq 5.5$ QSOs in the past decade. The separation range between the candidates and the main QSOs is $6' - 57'$ ($\sim 2 - 20$ pMpc at $z \sim 6$). To prove the robustness of our selected sample, we derived the photometric redshifts by fitting the candidate SEDs with a $z \sim 6$ QSOs composite spectrum and found that they are consistent with those derived for the main QSOs ($z = 5.6 - 6.3$). Among them, our best AGN candidate, PSO334.17123+26.75792, has a photometric redshift of $z = 6.08 \pm 0.07$. These candidates need future spectroscopic observations to confirm or reject their high-redshift origin.

6.1 Future prospects

As reported at the beginning of this Chapter, there are many open questions to answer in the next future. Below we summarize the open problems and the future plans to asses them:

- We have already submitted an ESO/NTT optical and NIR (EFOSC and SOFI) proposal of three nights to observe the 25 high-z AGN companions we found. The goals are to measure the redshifts, confirm the high-z nature of the candidates and their physical connection with the primary QSOs, and to derive the SMBH mass and Eddington ratio of those sources that are confirmed as companions. The proposed program is the final advance to confirm the derived photometric redshifts, and represents a crucial step to understand the impact of growing SMBHs on the large scale environment at the reionization epoch. If they will be confirmed as high-z QSO companions, they could pinpoint the possible presence of an overdense region around their main known QSOs, that should be investigated with future studies similarly to what we have done for SDSS J1030+0524.

- We have submitted an XMM-*Newton* proposal to observe SDSS J1030+0524 to investigate the observed X-ray spectral and flux variability. We plan to observe the QSO in spring and autumn 2020 for 50ks in each epoch, when the source is visible with XMM. Our immediate objective is to extend the temporal monitoring of SDSS J1030+0524. This will allow us to: i) obtain an accurate flux measurement in both epochs and verify whether the high flux value measured by XMM in 2003 is a rare flare or not; ii) determine what is the average/typical flux of the source. If the source flux is found to be similar to that measured by Chandra in 2002 and 2017, we will conclude that in 2003 the QSO was caught during a very rare, but still probable flare, and hence the variability of SDSS J1030+0524 is consistent with standard quasar variability. On the other hand, if larger values are measured, e.g. similar to those seen in 2003, then SDSS J1030+0524 will keep being a peculiar source candidate whose variability challenges current accretion models, motivating further X-ray monitoring in the future.

- The presence of the overdense region around the $z \sim 6$ QSO SDSS J1030+0524 is still to be confirmed, and we plan to derive the redshifts of those X-ray sources with no optical counterparts to find possible high-z faint/obscured AGN companions. Nowadays, this can only be achieved by mm/sub-mm observations that are able to detect (and hence measure the redshift) of the [CII] line (158 μm rest-frame) emitted by the host-galaxy of these sources. To infer the redshifts of our candidates, we plan to use ALMA to scan with six different frequency settings the frequency range centered at 260 GHz, where the [CII] line emitted at $z = 6.0 - 6.6$ can be detected. The identification of some of these source as high-z companions will strengthen the evidence of an overdense region around SDSS J1030+0524.

Appendix A

Likelihood-ratio method

As described in §4.2.3, after producing three simulations that mirror our J1030 field and using *wavdetect* to detect the sources on these simulated fields, we needed a numerical method to disentangle output sources that actually correspond to input ones from those that are spurious detections. To this purpose, we used a likelihood-ratio (LR) method to match output with input sources. The LR method we adopted was already used in past works to match sources detected at different wavelength (e.g., Sutherland & Saunders 1992; Ciliegi et al. 2003; Brusa et al. 2007; Luo et al. 2010). For an input simulated candidate with a flux f at an angular separation r from a given X-ray output, the LR is defined as in Equation 4.2:

$$LR = \frac{F(r)q(f)}{n(f)} \tag{A.1}$$

In Equation 4.2 we assumed that $F(r)$ (the probability distribution function of the angular separation) follows a Gaussian distribution (e.g., Zamorani et al. 1999):

$$F(r) = \frac{1}{2\pi\sigma_{pos}^2} exp\left(\frac{-r^2}{2\sigma_{pos}^2}\right) \tag{A.2}$$

where σ_{pos} is the 1σ positional error of the X-ray detected sources computed as $\sigma_{pos} = PSF_{Radius}/\sqrt{C}$ (Puccetti et al. 2009), while C are the net, background-subtracted, counts computed by AE, and PSF_{Radius} is evaluated with the estimate at the 90% encircled energy radius (at E = 1.5 keV) ad off-axis (θ) as $PSF_{Radius} = 1" + 10"(\theta/10')^2$ (Hickox & Markevitch 2006).

The flux-dependent surface density of the background sources, $n(f)$, is estimated using our sample of input simulated sources that are at an angular separation inside an annulus from any of the output detected sources ($r_{in} = 5"$ and $r_{out} = 30"$; e.g., Luo et al., 2010). Input sources that fall inside the annular regions are considered as background sources.

$q(f)$ is the expected flux distribution of counterparts, and is not directly observable. To derive an estimate of $q(f)$, the LR method selects all input sources within $r_{in} = 2$" from any detected source. The flux distribution of these sources is denoted as $total(f)$, which was then background-subtracted to derive:

$$real(f) = total(f) - \pi r_{in}^2 N_{out} n(f) \tag{A.3}$$

where N_{out} is the total number of X-ray detected sources. Due to the magnitude limits of the input catalog, we were only able to detect a fraction Q of all the true counterparts (see §4.2.3 for the definition of Q). Thus the expected flux distribution of the counterparts $q(f)$ is derived by normalizing $real(f)$ and then multiplying by Q:

$$q(f) = \frac{real(f)}{\sum_i real(f)_i} Q \tag{A.4}$$

Having computed the values of $q(f)$, $n(f)$, and $f(r)$, our LR method calculates LR values for all the input sources within $r_{LR} = 5$" from each output detected source.

Chapter 7

Ringraziamenti

"Mi spinsi nel futuro quanto mai occhio umano, le meraviglie vidi di quel mondo lontano."

A volte penso che sarebbe bello potersi spingere nel futuro per vedere cosa ci aspetta, quali sfide ci attendono, quali nuove sorprese o scoperte e cosa il futuro ha in serbo per noi. Poi ripenso che se dovessi vivere con la consapevolezza di eventi che accadranno forse la mia curiosità cesserebbe, tutto diventerebbe piatto e scontato e forse non ci sarebbe più un libero arbitrio in quello che faccio. Quando ho iniziato il corso di astronomia otto anni fa avevo già spinto il mio occhio lontano nel futuro; già sapevo che avrei fatto la magistrale, che avrei voluto fare un dottorato e che dopo di quello avrei tentato un postdoc. Forse era un percorso scontato per la mia carriera e forse non è nemmeno importante il risultato di tutte queste tappe intraprese, ma il come sono state vissute, le esperienze fatte e le persone con cui si sono condivisi i momenti più importanti di questo percorso. Ora sto per iniziare l'ultima parte di quel progetto che avevo immaginato tempo fa. Non so cosa ne sarà dopo. All'epoca era già incredibile per me fare piani da lì fino a dieci anni, figurarsi andare oltre. Di quel che sarà dopo il postdoc vedrò poi. Ora che sono qui in un altro paese lontano da casa e che ho un attimo per voltarmi indietro e ripensare agli ultimi tre anni, ci tengo a menzionare e ricordare tutte le persone con cui ho condiviso i momenti più belli di questo dottorato. Ad essere precisi dovrei ringraziare tutte le persone che mi sono state vicine da sempre, e che ho già menzionato nei ringraziamenti della mia precedente tesi, ma questa volta mi limiterò a menzionare quelli che più hanno dato un contributo in questi ultimi anni, così come i nuovi arrivati nella mia vita.

In primis ringrazio i miei supervisor e i più stretti collaboratori: Roberto e Cristian. Ci sono voluti un po' di mesi per togliere le formalità con cui vi chiamavo (Professore, Dottore) ma penso che vi siate un po' divertiti di questo mio modo di fare all'inizio. Spero siate fieri del lavoro che ho svolto sotto la vostra guida

e supervisione, e spero anche di continuare a lavorare con con voi per i progetti a venire. Tra i collaboratori vorrei anche menzionare l'aiuto fornito da Stefano, Giorgio e Roberto D. I vostri consigli mi hanno spesso aiutato e insegnato molto. Tra i collaboratori di Heidelberg ci tengo a menzionare Chiara. Sei sempre stata molto paziente con me e mi hai anche fatto da mentore per quei mesi in Germania. Non lo dimenticherò mai e ti auguro ogni buona cosa per il futuro.

Tra i colleghi vorrei ringraziare i miei compagni di ufficio. In primis i 4 G(unny): Jack, Ale e quel coglionazzo di Vittorio. È stato per me un onore e un grande piacere fare parte di quell'ufficio. Mi mancano le giornate passate assieme a parlare, di scherzi e di pettegolezzi. Ricordo affettuosamente anche Alberto, il mio primo mentore, che mi ha sempre consigliato sulle scelte future e col quale ho condiviso spesso battute ciniche per rallegrare la monotonia. Sicuramente quello che più non se la raccatta è Antonio il Pensabene (Benza o Gensabene se vuoi essere il quinto Gunny). Il manicomio che abbiamo fatto io e te in quell'ufficio è irripetibile e ti auguro una buona continuazione di carriera con la speranza che un altro coglionazzo come me arrivi a farti compagnia. Ovviamente devo ringraziare anche il PEKA (o PEHA) per la fitta collaborazione che sembra non finire mai (nemmeno ora che stiamo in due posti diversi). Mi raccomando, non lavorare troppo e non dare testate alle belle ragazze se ti impezzano. Non vogliono rubarti il portafoglio. I ringraziamenti un po' più seri (ma neanche troppo) vanno anche a Olga, per tutto il tempo passato a parlare di cose varie e giochi di ruolo, e a Sandro, che mi ha fatto da mentore per la divulgazione e con cui spero di collaborare ancora in futuro. Ammetto che mi mancano i momenti passati a scherzare sui fatti impensabili della scienza.

Ringrazio tutti gli amici con cui sono uscito e esco da sempre ma soprattutto vorrei ringraziare i Fojonco, per i bellissimi momenti passati a rievocazione, e i nuovi arrivati. Tra i nuovi arrivati "Bolognesi" abbiamo Alberto, con cui ho passato dei bellissimi momenti a bere buona birra, giocare di ruolo, fare finta di ballare lindy e andare in giro assieme per il Veneto. Poi abbiamo i "Germani", i miei carissimi amici di Heidelberg, con cui ho vissuto per sei mesi assieme. So che molti di voi non capiscono l'italiano ma vi ringrazio lo stesso. Un grazie infinito va a Matteo, Ben, Yulong, Sabina, Carla, Christos, Mladen, Camille e il fantastico Neven. Si tu Neven, trekker sfegatato e amante della politica. Spero tu possa trovare una posizione lavorativa che ti soddisfi e che ci riporti a passare altro tempo assieme.

Infine ringrazio la mia famiglia, che ha sempre un posto speciale per me. Soprattutto i miei genitori, che ora si ritrovano a fare i conti con due nipoti e con un figlio lontano nel tempo e nello spazio. Grazie al vostro aiuto me la sono sempre cavata e i risultati che ho ottenuto sono tanto miei quanto vostri. Non smetterò mai di essere fiero di fare parte della nostra famiglia. Infine ringrazio anche la

Polly (si lo so, sono abituato a questo nome dopo tanti anni, non ti arrabbiare) per gli ultimi mesi in cui mi sei stata molto vicina, aiutandomi ad affrontare sia la scrittura della tesi che l'inizio di questa nuova avventura. So quanto sia difficile vivere lontani ma non vedo l'ora di poter affrontare altre avventure assieme, e in questo sono fiducioso.

E visto che un capitolo si è concluso mentre un altro inizia ora:

"Larga è la foglia, stretta è la via. Dite la vostra che io ho detto la mia."

Bibliography

Agarwal, B., Dalla Vecchia, C., Johnson, J. L., Khochfar, S. & Paardekooper, J.-P. (2014), 'The First Billion Years project: birthplaces of direct collapse black holes', *mnras* **443**, 648–657.

Ai, Y., Dou, L., Fan, X., Wang, F., Wu, X.-B. & Bian, F. (2016), 'Exploratory Chandra Observation of the Ultraluminous Quasar SDSS J010013.02+280225.8 at Redshift 6.30', *apjl* **823**, L37.

Aird, J., Coil, A. L., Georgakakis, A., Nandra, K., Barro, G. & Pérez-González, P. G. (2015), 'The evolution of the X-ray luminosity functions of unabsorbed and absorbed AGNs out to z = 5', *mnras* **451**(2), 1892–1927.

Aird, J., Nandra, K., Georgakakis, A., Laird, E. S., Steidel, C. C. & Sharon, C. (2008), 'The X-ray luminosity function of AGN at z = 3', *mnras* **387**(2), 883–896.

Aird, J., Nandra, K., Laird, E. S., Georgakakis, A., Ashby, M. L. N., Barmby, P., Coil, A. L., Huang, J. S., Koekemoer, A. M., Steidel, C. C. & Willmer, C. N. A. (2010), 'The evolution of the hard X-ray luminosity function of AGN', *mnras* **401**(4), 2531–2551.

Alexander, D. M., Bauer, F. E., Chapman, S. C., Smail, I., Blain, A. W., Brandt, W. N. & Ivison, R. J. (2005), 'The X-Ray Spectral Properties of SCUBA Galaxies', *apj* **632**(2), 736–750.

Antonucci, R. (1993), 'Unified models for active galactic nuclei and quasars.', *araa* **31**, 473–521.

Arnaud, K. A. (1996), XSPEC: The First Ten Years, *in* G. H. Jacoby & J. Barnes, eds, 'Astronomical Data Analysis Software and Systems V', Vol. 101 of *Astronomical Society of the Pacific Conference Series*, p. 17.

Bañados, E. (2015), 'The discovery and characterization of the most distant quasars'.

Bañados, E., Venemans, B. P., Decarli, R., Farina, E. P., Mazzucchelli, C., Walter, F., Fan, X., Stern, D., Schlafly, E., Chambers, K. C., Rix, H.-W., Jiang, L., McGreer, I., Simcoe, R., Wang, F., Yang, J., Morganson, E., De Rosa, G., Greiner, J., Baloković, M., Burgett, W. S., Cooper, T., Draper, P. W., Flewelling, H., Hodapp, K. W., Jun, H. D., Kaiser, N., Kudritzki, R.-P., Magnier, E. A., Metcalfe, N., Miller, D., Schindler, J.-T., Tonry, J. L., Wainscoat, R. J., Waters, C. & Yang, Q. (2016), 'The Pan-STARRS1 Distant z>5.6 Quasar Survey: More than 100 Quasars within the First Gyr of the Universe', *apjs* **227**, 11.

Bañados, E., Venemans, B. P., Mazzucchelli, C., Farina, E. P., Walter, F., Wang, F., Decarli, R., Stern, D., Fan, X., Davies, F. B., Hennawi, J. F., Simcoe, R. A., Turner, M. L., Rix, H.-W., Yang, J., Kelson, D. D., Rudie, G. C. & Winters, J. M. (2018), 'An 800-million-solar-mass black hole in a significantly neutral Universe at a redshift of 7.5', *nat* **553**(7689), 473–476.

Bañados, E., Venemans, B. P., Mazzucchelli, C., Farina, E. P., Walter, F., Wang, F., Decarli, R., Stern, D., Fan, X., Davies, F., Hennawi, J. F., Simcoe, R., Turner, M. L., Rix, H., Yang, J., Kelson, D. D., Rudie, G. & Winters, J. M. (2017), 'An 800 million solar mass black hole in a significantly neutral universe at redshift 7.5', *ArXiv e-prints* .

Bañados, E., Venemans, B. P., Morganson, E., Decarli, R., Walter, F., Chambers, K. C., Rix, H. W., Farina, E. P., Fan, X., Jiang, L., McGreer, I., De Rosa, G., Simcoe, R., Weiß, A., Price, P. A., Morgan, J. S., Burgett, W. S., Greiner, J., Kaiser, N., Kudritzki, R. P., Magnier, E. A., Metcalfe, N., Stubbs, C. W., Sweeney, W., Tonry, J. L., Wainscoat, R. J. & Waters, C. (2014), 'Discovery of Eight z > 6 Quasars from Pan-STARRS1', *aj* **148**(1), 14.

Bañados, E., Venemans, B., Walter, F., Kurk, J., Overzier, R. & Ouchi, M. (2013), 'The Galaxy Environment of a QSO at z ˜ 5.7', *apj* **773**, 178.

Baldwin, J. A. (1977), 'The Ly-alpha/H-beta intensity ratio in the spectra of QSOs', *mnras* **178**, 67P–74P.

Balmaverde, B., Gilli, R., Mignoli, M., Bolzonella, M., Brusa, M., Cappelluti, N., Comastri, A., Sani, E., Vanzella, E., Vignali, C., Vito, F. & Zamorani, G. (2017), 'Primordial environment of supermassive black holes. II. Deep Y- and J-band images around the z 6.3 quasar SDSS J1030+0524', *aap* **606**, A23.

Barai, P., Gallerani, S., Pallottini, A., Ferrara, A., Marconi, A., Cicone, C., Maiolino, R. & Carniani, S. (2018), 'Quasar outflows at z > 6: the impact on the host galaxies', *mnras* **473**, 4003–4020.

Barnett, R., Warren, S. J., Banerji, M., McMahon, R. G., Hewett, P. C., Mortlock, D. J., Simpson, C., Venemans, B. P., Ota, K. & Shibuya, T. (2015), 'The spectral energy distribution of the redshift 7.1 quasar ULAS J1120+0641', *aap* **575**, A31.

Becker, G. D., Bolton, J. S., Madau, P., Pettini, M., Ryan-Weber, E. V. & Venemans, B. P. (2015), 'Evidence of patchy hydrogen reionization from an extreme Ly trough below redshift six', *mnras* **447**(4), 3402–3419.

Beckmann, V. & Shrader, C. R. (2012), *Active Galactic Nuclei*.

Bennett, C. L., Larson, D., Weiland, J. L., Jarosik, N., Hinshaw, G., Odegard, N., Smith, K. M., Hill, R. S., Gold, B., Halpern, M., Komatsu, E., Nolta, M. R., Page, L., Spergel, D. N., Wollack, E., Dunkley, J., Kogut, A., Limon, M., Meyer, S. S., Tucker, G. S. & Wright, E. L. (2013), 'Nine-year Wilkinson Microwave Anisotropy Probe (WMAP) Observations: Final Maps and Results', *apjs* **208**, 20.

Best, W. M. J., Liu, M. C., Magnier, E. A., Deacon, N. R., Aller, K. M., Redstone, J., Burgett, W. S., Chambers, K. C., Draper, P., Flewelling, H., Hodapp, K. W., Kaiser, N., Metcalfe, N., Tonry, J. L., Wainscoat, R. J. & Waters, C. (2015), 'A Search for L/T Transition Dwarfs with Pan-STARRS1 and WISE. II. L/T Transition Atmospheres and Young Discoveries', *apj* **814**(2), 118.

Bird, J., Martini, P. & Kaiser, C. (2008), 'The Lifetime of FR II Sources in Groups and Clusters: Implications for Radio-Mode Feedback', *apj* **676**, 147–162.

Brandt, W. N. & Alexander, D. M. (2015), 'Cosmic X-ray surveys of distant active galaxies. The demographics, physics, and ecology of growing supermassive black holes', *aapr* **23**, 1.

Brandt, W. N., Guainazzi, M., Kaspi, S., Fan, X., Schneider, D. P., Strauss, M. A., Clavel, J. & Gunn, J. E. (2001), 'An XMM-Newton Detection of the Z=5.80 X-Ray-Weak Quasar SDSSP J104433.04-012502.2', *aj* **121**, 591–597.

Brandt, W. N., Schneider, D. P., Fan, X., Strauss, M. A., Gunn, J. E., Richards, G. T., Anderson, S. F., Vanden Berk, D. E., Bahcall, N. A., Brinkmann, J., Brunner, R., Chen, B., Hennessy, G. S., Lamb, D. Q., Voges, W. & York, D. G. (2002), 'Exploratory Chandra Observations of the Three Highest Redshift Quasars Known', *apjl* **569**, L5–L9.

Broos, P., Townsley, L., Getman, K. & Bauer, F. (2012), 'AE: ACIS Extract'.

Brunetti, G., Setti, G. & Comastri, A. (1997), 'Inverse Compton X-rays from strong FRII radio-galaxies.', *aap* **325**, 898–910.

Brusa, M., Zamorani, G., Comastri, A., Hasinger, G., Cappelluti, N., Civano, F., Finoguenov, A., Mainieri, V., Salvato, M. & Vignali, C. (2007), 'The XMM-Newton Wide-Field Survey in the COSMOS Field. III. Optical Identification and Multiwavelength Properties of a Large Sample of X-Ray-Selected Sources', *apjs* **172**(1), 353–367.

Buchner, J., Georgakakis, A., Nandra, K., Brightman, M., Menzel, M.-L., Liu, Z., Hsu, L.-T., Salvato, M., Rangel, C., Aird, J., Merloni, A. & Ross, N. (2015), 'Obscuration-dependent Evolution of Active Galactic Nuclei', *apj* **802**(2), 89.

Burtscher, L., Meisenheimer, K., Tristram, K. R. W., Jaffe, W., Hönig, S. F., Davies, R. I., Kishimoto, M., Pott, J. U., Röttgering, H., Schartmann, M., Weigelt, G. & Wolf, S. (2013), 'A diversity of dusty AGN tori. Data release for the VLTI/MIDI AGN Large Program and first results for 23 galaxies', *aap* **558**, A149.

Calura, F., Gilli, R., Vignali, C., Pozzi, F., Pipino, A. & Matteucci, F. (2014), 'The dust content of QSO hosts at high redshift', *mnras* **438**, 2765–2783.

Cappelluti, N., Brusa, M., Hasinger, G., Comastri, A., Zamorani, G., Finoguenov, A., Gilli, R., Puccetti, S., Miyaji, T. & Salvato, M. (2009), 'The XMM-Newton wide-field survey in the COSMOS field. The point-like X-ray source catalogue', *aap* **497**(2), 635–648.

Cappelluti, N., Hasinger, G., Brusa, M., Comastri, A., Zamorani, G., Böhringer, H., Brunner, H., Civano, F., Finoguenov, A. & Fiore, F. (2007), 'The XMM-Newton Wide-Field Survey in the COSMOS Field. II. X-Ray Data and the logN-logS Relations', *apjs* **172**(1), 341–352.

Carilli, C. L., Harris, D. E., Pentericci, L., Röttgering, H. J. A., Miley, G. K., Kurk, J. D. & van Breugel, W. (2002), 'The X-Ray-Radio Alignment in the z=2.2 Radio Galaxy PKS 1138-262', *apj* **567**, 781–789.

Carilli, C. L. & Walter, F. (2013), 'Cool Gas in High-Redshift Galaxies', *araa* **51**(1), 105–161.

Carnall, A. C., Shanks, T., Chehade, B., Fumagalli, M., Rauch, M., Irwin, M. J., Gonzalez-Solares, E., Findlay, J. R. & Metcalfe, N. (2015), 'Two bright $z > 6$ quasars from VST ATLAS and a new method of optical plus mid-infrared colour selection.', *mnras* **451**, L16–L20.

Cash, W. (1979), 'Parameter estimation in astronomy through application of the likelihood ratio', *apj* **228**, 939–947.

Chartas, G., Krawczynski, H., Zalesky, L., Kochanek, C. S., Dai, X., Morgan, C. W. & Mosquera, A. (2017), 'Measuring the Innermost Stable Circular Orbits of Supermassive Black Holes', *apj* **837**(1), 26.

Chartas, G., Rhea, C., Kochanek, C., Dai, X., Morgan, C., Blackburne, J., Chen, B., Mosquera, A. & MacLeod, C. (2016), 'Gravitational lensing size scales for quasars', *Astronomische Nachrichten* **337**(4-5), 356.

Chiaberge, M., Capetti, A. & Celotti, A. (1999), 'The HST view of FR I radio galaxies: evidence for non-thermal nuclear sources', *aap* **349**, 77–87.

Chiaberge, M., Celotti, A., Capetti, A. & Ghisellini, G. (2000), 'Does the unification of BL Lac and FR I radio galaxies require jet velocity structures?', *aap* **358**, 104–112.

Ciliegi, P., Zamorani, G., Hasinger, G., Lehmann, I., Szokoly, G. & Wilson, G. (2003), 'A deep VLA survey at 6 cm in the Lockman Hole', *aap* **398**, 901–918.

Civano, F., Elvis, M., Brusa, M., Comastri, A., Salvato, M., Zamorani, G., Aldcroft, T., Bongiorno, A., Capak, P., Cappelluti, N., Cisternas, M., Fiore, F., Fruscione, A., Hao, H., Kartaltepe, J., Koekemoer, A., Gilli, R., Impey, C. D., Lanzuisi, G., Lusso, E., Mainieri, V., Miyaji, T., Lilly, S., Masters, D., Puccetti, S., Schawinski, K., Scoville, N. Z., Silverman, J., Trump, J., Urry, M., Vignali, C. & Wright, N. J. (2012), 'The Chandra COSMOS Survey. III. Optical and Infrared Identification of X-Ray Point Sources', *apjs* **201**(2), 30.

Civano, F., Marchesi, S., Comastri, A., Urry, M. C., Elvis, M., Cappelluti, N., Puccetti, S., Brusa, M., Zamorani, G., Hasinger, G., Aldcroft, T., Alexander, D. M., Allevato, V., Brunner, H., Capak, P., Finoguenov, A., Fiore, F., Fruscione, A., Gilli, R., Glotfelty, K., Griffiths, R. E., Hao, H., Harrison, F. A., Jahnke, K., Kartaltepe, J., Karim, A., LaMassa, S. M., Lanzuisi, G., Miyaji, T., Ranalli, P., Salvato, M., Sargent, M., Scoville, N. J., Schawinski, K., Schinnerer, E., Silverman, J., Smolcic, V., Stern, D., Toft, S., Trakhenbrot, B., Treister, E. & Vignali, C. (2016), 'The Chandra Cosmos Legacy Survey: Overview and Point Source Catalog', *apj* **819**, 62.

Comastri, A., Ranalli, P., Iwasawa, K., Vignali, C., Gilli, R., Georgantopoulos, I., Barcons, X., Brand t, W. N., Brunner, H., Brusa, M., Cappelluti, N., Carrera, F. J., Civano, F., Fiore, F., Hasinger, G., Mainieri, V., Merloni, A., Nicastro, F., Paolillo, M., Puccetti, S., Rosati, P., Silverman, J. D., Tozzi, P., Zamorani, G., Balestra, I., Bauer, F. E., Luo, B. & Xue, Y. Q. (2011), 'The XMM Deep survey in the CDF-S. I. First results on heavily obscured AGN', *aap* **526**, L9.

Connor, T., Bañados, E., Stern, D., Decarli, R., Schindler, J.-T., Fan, X., Farina, E. P., Mazzucchelli, C., Mulchaey, J. S. & Walter, F. (2019), 'Two X-ray Sources in a z 6.2 Quasar/Galaxy Merger', *arXiv e-prints* p. arXiv:1909.08619.

Costa, T., Sijacki, D., Trenti, M. & Haehnelt, M. G. (2014), 'The environment of bright QSOs at z = 6: star-forming galaxies and X-ray emission', *mnras* **439**, 2146–2174.

Cowie, L. L., Songaila, A., Hu, E. M. & Cohen, J. G. (1996), 'New Insight on Galaxy Formation and Evolution From Keck Spectroscopy of the Hawaii Deep Fields', *aj* **112**, 839.

Davis, J. E., Bautz, M. W., Dewey, D., Heilmann, R. K., Houck, J. C., Huenemoerder, D. P., Marshall, H. L., Nowak, M. A., Schattenburg, M. L., Schulz, N. S. & Smith, R. K. (2012), Raytracing with MARX: x-ray observatory design, calibration, and support, *in* 'Space Telescopes and Instrumentation 2012: Ultraviolet to Gamma Ray', Vol. 8443 of *procspie*, p. 84431A.

De Rosa, G., Decarli, R., Walter, F., Fan, X., Jiang, L., Kurk, J., Pasquali, A. & Rix, H. W. (2011), 'Evidence for Non-evolving Fe II/Mg II Ratios in Rapidly Accreting z ˜ 6 QSOs', *apj* **739**, 56.

Decarli, R., Walter, F., Venemans, B. P., Banados, E., Bertoldi, F., Carilli, C., Fan, X., Farina, E. P., Mazzucchelli, C., Riechers, D., Rix, H.-W., Strauss, M. A., Wang, R. & Yang, Y. (2018), 'An ALMA [CII] survey of 27 quasars at z>5.94', *ArXiv e-prints* .

Di Matteo, T., Springel, V. & Hernquist, L. (2005), 'Energy input from quasars regulates the growth and activity of black holes and their host galaxies', *nat* **433**(7026), 604–607.

Diamond-Stanic, A. M., Fan, X., Brandt, W. N., Shemmer, O., Strauss, M. A., Anderson, S. F., Carilli, C. L., Gibson, R. R., Jiang, L., Kim, J. S., Richards, G. T., Schmidt, G. D., Schneider, D. P., Shen, Y., Smith, P. S., Vestergaard, M. & Young, J. E. (2009), 'High-redshift SDSS Quasars with Weak Emission Lines', *apj* **699**, 782–799.

Done, C., Davis, S. W., Jin, C., Blaes, O. & Ward, M. (2012), 'Intrinsic disc emission and the soft X-ray excess in active galactic nuclei', *mnras* **420**(3), 1848–1860.

Dubois, Y., Pichon, C., Devriendt, J., Silk, J., Haehnelt, M., Kimm, T. & Slyz, A. (2013), 'Blowing cold flows away: the impact of early AGN activity on the formation of a brightest cluster galaxy progenitor', *mnras* **428**, 2885–2900.

Erlund, M. C., Fabian, A. C., Blundell, K. M., Celotti, A. & Crawford, C. S. (2006), 'Extended inverse-Compton emission from distant, powerful radio galaxies', *mnras* **371**, 29–37.

Event Horizon Telescope Collaboration, Akiyama, K., Alberdi, A., Alef, W., Asada, K., Azulay, R., Baczko, A.-K., Ball, D., Baloković, M., Barrett, J., Bintley, D., Blackburn, L., Boland, W., Bouman, K. L., Bower, G. C., Bremer, M., Brinkerink, C. D., Brissenden, R., Britzen, S., Broderick, A. E., Broguiere, D., Bronzwaer, T., Byun, D.-Y., Carlstrom, J. E., Chael, A., Chan, C.-k., Chatterjee, S., Chatterjee, K., Chen, M.-T., Chen, Y., Cho, I., Christian, P., Conway, J. E., Cordes, J. M., Crew, G. B., Cui, Y., Davelaar, J., De Laurentis, M., Deane, R., Dempsey, J., Desvignes, G., Dexter, J., Doeleman, S. S., Eatough, R. P., Falcke, H., Fish, V. L., Fomalont, E., Fraga-Encinas, R., Friberg, P., Fromm, C. M., Gómez, J. L., Galison, P., Gammie, C. F., García, R., Gentaz, O., Georgiev, B., Goddi, C., Gold, R., Gu, M., Gurwell, M., Hada, K., Hecht, M. H., Hesper, R., Ho, L. C., Ho, P., Honma, M., Huang, C.-W. L., Huang, L., Hughes, D. H., Ikeda, S., Inoue, M., Issaoun, S., James, D. J., Jannuzi, B. T., Janssen, M., Jeter, B., Jiang, W., Johnson, M. D., Jorstad, S., Jung, T., Karami, M., Karuppusamy, R., Kawashima, T., Keating, G. K., Kettenis, M., Kim, J.-Y., Kim, J., Kim, J., Kino, M., Koay, J. Y., Koch, P. M., Koyama, S., Kramer, M., Kramer, C., Krichbaum, T. P., Kuo, C.-Y., Lauer, T. R., Lee, S.-S., Li, Y.-R., Li, Z., Lindqvist, M., Liu, K., Liuzzo, E., Lo, W.-P., Lobanov, A. P., Loinard, L., Lonsdale, C., Lu, R.-S., MacDonald, N. R., Mao, J., Markoff, S., Marrone, D. P., Marscher, A. P., Martí-Vidal, I., Matsushita, S., Matthews, L. D., Medeiros, L., Menten, K. M., Mizuno, Y., Mizuno, I., Moran, J. M., Moriyama, K., Moscibrodzka, M., Müller, C., Nagai, H., Nagar, N. M., Nakamura, M., Narayan, R., Narayanan, G., Natarajan, I., Neri, R., Ni, C., Noutsos, A., Okino, H., Olivares, H., Oyama, T., Özel, F., Palumbo, D. C. M., Patel, N., Pen, U.-L., Pesce, D. W., Piétu, V., Plambeck, R., PopStefanija, A. a., Porth, O., Prather, B., Preciado-López, J. A., Psaltis, D., Pu, H.-Y., Ramakrishnan, V., Rao, R., Rawlings, M. G., Raymond, A. W., Rezzolla, L., Ripperda, B., Roelofs, F., Rogers, A., Ros, E., Rose, M., Roshanineshat, A., Rottmann, H., Roy, A. L., Ruszczyk, C., Ryan, B. R., Rygl, K. L. J., Sánchez, S., Sánchez-Arguelles, D., Sasada, M., Savolainen, T., Schloerb, F. P., Schuster, K.-F., Shao, L., Shen, Z., Small, D., Sohn, B. W., SooHoo, J., Tazaki, F., Tiede, P., Tilanus, R. P. J., Titus, M., Toma, K., Torne, P., Trent, T., Trippe, S., Tsuda, S., van Bemmel, I., van Langevelde, H. J., van Rossum, D. R., Wagner, J., Wardle, J., Weintroub, J., Wex, N., Wharton, R., Wielgus, M., Wong, G. N., Wu, Q., Young, A., Young, K., Younsi, Z., Yuan, F., Yuan, Y.-F., Zensus, J. A., Zhao, G., Zhao, S.-S., Zhu, Z., Farah, J. R., Meyer-Zhao, Z., Michalik, D., Nadolski, A., Nishioka, H., Pradel, N., Primiani, R. A., Souccar, K., Vertatschitsch, L.

& Yamaguchi, P. (2019), 'First M87 Event Horizon Telescope Results. VI. The Shadow and Mass of the Central Black Hole', *apjl* **875**(1), L6.

Fabian, A. C. & Miniutti, G. (2005), 'The X-ray spectra of accreting Kerr black holes', *arXiv e-prints* pp. astro–ph/0507409.

Fabian, A. C., Sanders, J. S., Ettori, S., Taylor, G. B., Allen, S. W., Crawford, C. S., Iwasawa, K., Johnstone, R. M. & Ogle, P. M. (2000), 'Chandra imaging of the complex X-ray core of the Perseus cluster', *mnras* **318**(4), L65–L68.

Fabian, A. C., Walker, S. A., Celotti, A., Ghisellini, G., Mocz, P., Blundell, K. M. & McMahon, R. G. (2014), 'Do high-redshift quasars have powerful jets?', *mnras* **442**, L81–L84.

Fan, X. (2012), 'Observations of the first light and the epoch of reionization', *Research in Astronomy and Astrophysics* **12**(8), 865–890.

Fan, X., Narayanan, V. K., Lupton, R. H., Strauss, M. A., Knapp, G. R., Becker, R. H., White, R. L., Pentericci, L., Leggett, S. K., Haiman, Z., Gunn, J. E., Ivezić, Ž., Schneider, D. P., Anderson, S. F., Brinkmann, J., Bahcall, N. A., Connolly, A. J., Csabai, I., Doi, M., Fukugita, M., Geballe, T., Grebel, E. K., Harbeck, D., Hennessy, G., Lamb, D. Q., Miknaitis, G., Munn, J. A., Nichol, R., Okamura, S., Pier, J. R., Prada, F., Richards, G. T., Szalay, A. & York, D. G. (2001), 'A Survey of z>5.8 Quasars in the Sloan Digital Sky Survey. I. Discovery of Three New Quasars and the Spatial Density of Luminous Quasars at z=6', *aj* **122**, 2833–2849.

Fan, X., Strauss, M. A., Richards, G. T., Hennawi, J. F., Becker, R. H., White, R. L., Diamond-Stanic, A. M., Donley, J. L., Jiang, L., Kim, J. S., Vestergaard, M., Young, J. E., Gunn, J. E., Lupton, R. H., Knapp, G. R., Schneider, D. P., Brandt, W. N., Bahcall, N. A., Barentine, J. C., Brinkmann, J., Brewington, H. J., Fukugita, M., Harvanek, M., Kleinman, S. J., Krzesinski, J., Long, D., Neilsen, Jr., E. H., Nitta, A., Snedden, S. A. & Voges, W. (2006), 'A Survey of z>5.7 Quasars in the Sloan Digital Sky Survey. IV. Discovery of Seven Additional Quasars', *aj* **131**, 1203–1209.

Fan, X., White, R. L., Davis, M., Becker, R. H., Strauss, M. A., Haiman, Z., Schneider, D. P., Gregg, M. D., Gunn, J. E., Knapp, G. R., Lupton, R. H., Anderson, John E., J., Anderson, S. F., Annis, J., Bahcall, N. A., Boroski, W. N., Brunner, R. J., Chen, B., Connolly, A. J., Csabai, I., Doi, M., Fukugita, M., Hennessy, G. S., Hindsley, R. B., Ichikawa, T., Ivezić, Ž., Loveday, J., Meiksin, A., McKay, T. A., Munn, J. A., Newberg, H. J., Nichol, R., Okamura, S., Pier, J. R., Sekiguchi, M., Shimasaku, K., Stoughton, C., Szalay, A. S.,

Szokoly, G. P., Thakar, A. R., Vogeley, M. S. & York, D. G. (2000), 'The Discovery of a Luminous Z=5.80 Quasar from the Sloan Digital Sky Survey', *aj* **120**(3), 1167–1174.

Farrah, D., Priddey, R., Wilman, R., Haehnelt, M. & McMahon, R. (2004), 'The X-Ray Spectrum of the z=6.30 QSO SDSS J1030+0524', *apjl* **611**, L13–L16.

Ferrarese, L. & Merritt, D. (2000), 'A Fundamental Relation between Supermassive Black Holes and Their Host Galaxies', *apjl* **539**(1), L9–L12.

Fontanot, F., De Lucia, G., Monaco, P., Somerville, R. S. & Santini, P. (2009), 'The many manifestations of downsizing: hierarchical galaxy formation models confront observations', *mnras* **397**(4), 1776–1790.

Fujimoto, S., Oguri, M., Nagao, T., Izumi, T. & Ouchi, M. (2019), 'Truth or delusion? A possible gravitational lensing interpretation of the ultra-luminous quasar SDSS J010013.02+280225.8 at z=6.30', *arXiv e-prints* p. arXiv:1909.13512.

Gabor, J. M. & Bournaud, F. (2013), 'Simulations of supermassive black hole growth in high-redshift disc galaxies', *mnras* **434**, 606–620.

Gallerani, S., Zappacosta, L., Orofino, M. C., Piconcelli, E., Vignali, C., Ferrara, A., Maiolino, R., Fiore, F., Gilli, R., Pallottini, A., Neri, R. & Feruglio, C. (2017*a*), 'X-ray spectroscopy of the z = 6.4 quasar SDSS J1148+5251', *mnras* **467**, 3590–3597.

Gallerani, S., Zappacosta, L., Orofino, M. C., Piconcelli, E., Vignali, C., Ferrara, A., Maiolino, R., Fiore, F., Gilli, R., Pallottini, A., Neri, R. & Feruglio, C. (2017*b*), 'X-ray spectroscopy of the z = 6.4 quasar SDSS J1148+5251', *mnras* **467**, 3590–3597.

Gawiser, E., van Dokkum, P. G., Herrera, D., Maza, J., Castander, F. J., Infante, L., Lira, P., Quadri, R., Toner, R., Treister, E., Urry, C. M., Altmann, M., Assef, R., Christlein, D., Coppi, P. S., Durán, M. F., Franx, M., Galaz, G., Huerta, L., Liu, C., López, S., Méndez, R., Moore, D. C., Rubio, M., Ruiz, M. T., Toft, S. & Yi, S. K. (2006), 'The Multiwavelength Survey by Yale-Chile (MUSYC): Survey Design and Deep Public UBVRIz' Images and Catalogs of the Extended Hubble Deep Field-South', *apjs* **162**, 1–19.

Gehrels, N. (1986), 'Confidence limits for small numbers of events in astrophysical data', *apj* **303**, 336–346.

Ghisellini, G. & Celotti, A. (2001), 'The dividing line between FR I and FR II radio-galaxies', *aap* **379**, L1–L4.

Ghisellini, G., Tavecchio, F., Maraschi, L., Celotti, A. & Sbarrato, T. (2014), 'The power of relativistic jets is larger than the luminosity of their accretion disks', *nat* **515**, 376–378.

Gilli, R., Calura, F., D'Ercole, A. & Norman, C. (2017), 'Exponentially growing bubbles around early supermassive black holes', *aap* **603**, A69.

Gilli, R., Comastri, A. & Hasinger, G. (2007), 'The synthesis of the cosmic X-ray background in the Chandra and XMM-Newton era', *aap* **463**(1), 79–96.

Gilli, R., Su, J., Norman, C., Vignali, C., Comastri, A., Tozzi, P., Rosati, P., Stiavelli, M., Brandt, W. N., Xue, Y. Q., Luo, B., Castellano, M., Fontana, A., Fiore, F., Mainieri, V. & Ptak, A. (2011), 'A Compton-thick Active Galactic Nucleus at z $\sim$5 in the 4 Ms Chandra Deep Field South', *apjl* **730**(2), L28.

Haardt, F. & Maraschi, L. (1991), 'A two-phase model for the X-ray emission from Seyfert galaxies', *apjl* **380**, L51–L54.

Haardt, F. & Maraschi, L. (1993), 'X-ray spectra from two-phase accretion disks', *apj* **413**, 507–517.

Habouzit, M., Volonteri, M., Latif, M., Dubois, Y. & Peirani, S. (2016), 'On the number density of 'direct collapse' black hole seeds', *mnras* **463**(1), 529–540.

Habouzit, M., Volonteri, M., Somerville, R. S., Dubois, Y., Peirani, S., Pichon, C. & Devriendt, J. (2019), 'The diverse galaxy counts in the environment of high-redshift massive black holes in Horizon-AGN', *mnras* **489**(1), 1206–1229.

Häring, N. & Rix, H.-W. (2004), 'On the Black Hole Mass-Bulge Mass Relation', *apjl* **604**(2), L89–L92.

Harrison, C. (2014), Observational constraints on the influence of active galactic nuclei on the evolution of galaxies, PhD thesis, Durham University.

Hasinger, G. (2008), 'Absorption properties and evolution of active galactic nuclei', *Astronomy and Astrophysics* **490**(3), 905–922.

Hasinger, G., Miyaji, T. & Schmidt, M. (2005), 'Luminosity-dependent evolution of soft X-ray selected AGN. New Chandra and XMM-Newton surveys', *aap* **441**(2), 417–434.

Hickox, R. C., Jones, C., Forman, W. R., Murray, S. S., Kochanek, C. S., Eisenstein, D., Jannuzi, B. T., Dey, A., Brown, M. J. I., Stern, D., Eisenhardt, P. R., Gorjian, V., Brodwin, M., Narayan, R., Cool, R. J., Kenter, A., Caldwell, N. & Anderson, M. E. (2009), 'Host Galaxies, Clustering, Eddington Ratios, and Evolution of Radio, X-Ray, and Infrared-Selected AGNs', *apj* **696**(1), 891–919.

Hickox, R. C. & Markevitch, M. (2006), 'Absolute Measurement of the Unresolved Cosmic X-Ray Background in the 0.5-8 keV Band with Chandra', *apj* **645**(1), 95–114.

Hopkins, P. F., Hernquist, L., Cox, T. J. & Kereš, D. (2008), 'A Cosmological Framework for the Co-Evolution of Quasars, Supermassive Black Holes, and Elliptical Galaxies. I. Galaxy Mergers and Quasar Activity', *apjs* **175**, 356–389.

Husband, K., Bremer, M. N., Stanway, E. R., Davies, L. J. M., Lehnert, M. D. & Douglas, L. S. (2013), 'Are z = 5 quasars found in the most massive high-redshift overdensities?', *mnras* **432**, 2869–2877.

Iwasawa, K. & Taniguchi, Y. (1993), 'The X-Ray Baldwin Effect', *apjl* **413**, L15.

Jaffe, W., Meisenheimer, K., Röttgering, H. J. A., Leinert, C., Richichi, A., Chesneau, O., Fraix-Burnet, D., Glazenborg-Kluttig, A., Granato, G. L., Graser, U., Heijligers, B., Köhler, R., Malbet, F., Miley, G. K., Paresce, F., Pel, J. W., Perrin, G., Przygodda, F., Schoeller, M., Sol, H., Waters, L. B. F. M., Weigelt, G., Woillez, J. & de Zeeuw, P. T. (2004), 'The central dusty torus in the active nucleus of NGC 1068', *nat* **429**(6987), 47–49.

Jiang, L., Fan, X., Brandt, W. N., Carilli, C. L., Egami, E., Hines, D. C., Kurk, J. D., Richards, G. T., Shen, Y., Strauss, M. A., Vestergaard, M. & Walter, F. (2010), 'Dust-free quasars in the early Universe', *nat* **464**, 380–383.

Just, D. W., Brandt, W. N., Shemmer, O., Steffen, A. T., Schneider, D. P., Chartas, G. & Garmire, G. P. (2007), 'The X-Ray Properties of the Most Luminous Quasars from the Sloan Digital Sky Survey', *apj* **665**, 1004–1022.

Kaastra, J. S., Mewe, R., Liedahl, D. A., Komossa, S. & Brinkman, A. C. (2000), 'X-ray absorption lines in the Seyfert 1 galaxy NGC 5548 discovered with Chandra-LETGS', *aap* **354**, L83–L86.

Kalberla, P. M. W., Burton, W. B., Hartmann, D., Arnal, E. M., Bajaja, E., Morras, R. & Pöppel, W. G. L. (2005), 'The Leiden/Argentine/Bonn (LAB) Survey of Galactic HI. Final data release of the combined LDS and IAR surveys with improved stray-radiation corrections', *aap* **440**, 775–782.

Kallman, T. & Bautista, M. (2001), 'Photoionization and High-Density Gas', *apjs* **133**, 221–253.

Kartaltepe, J. S., Sanders, D. B., Scoville, N. Z., Calzetti, D., Capak, P., Koekemoer, A., Mobasher, B., Murayama, T., Salvato, M., Sasaki, S. S. & Taniguchi, Y. (2007), 'Evolution of the Frequency of Luminous Close Galaxy Pairs at z < 1.2 in the COSMOS Field', *apjs* **172**(1), 320–328.

Kaspi, S., Brandt, W. N., Netzer, H., Sambruna, R., Chartas, G., Garmire, G. P. & Nousek, J. A. (2000), 'Discovery of Narrow X-Ray Absorption Lines from NGC 3783 with the Chandra High Energy Transmission Grating Spectrometer', *apjl* **535**(1), L17–L20.

Kellermann, K. I., Sramek, R., Schmidt, M., Shaffer, D. B. & Green, R. (1989), 'VLA observations of objects in the Palomar Bright Quasar Survey', *aj* **98**, 1195–1207.

Kelly, B. C., Bechtold, J., Siemiginowska, A., Aldcroft, T. & Sobolewska, M. (2007), 'Evolution of the X-ray Emission of Radio-quiet Quasars', *apj* **657**, 116–134.

Kocevski, D. D., Hasinger, G., Brightman, M., Nandra, K., Georgakakis, A., Cappelluti, N., Civano, F., Li, Y., Li, Y., Aird, J., Alexander, D. M., Almaini, O., Brusa, M., Buchner, J., Comastri, A., Conselice, C. J., Dickinson, M. A., Finoguenov, A., Gilli, R., Koekemoer, A. M., Miyaji, T., Mullaney, J. R., Papovich, C., Rosario, D., Salvato, M., Silverman, J. D., Somerville, R. S. & Ueda, Y. (2018), 'X-UDS: The Chandra Legacy Survey of the UKIDSS Ultra Deep Survey Field', *apjs* **236**(2), 48.

Kormendy, J. & Ho, L. C. (2013), 'Coevolution (Or Not) of Supermassive Black Holes and Host Galaxies', *araa* **51**(1), 511–653.

Kurk, J. D., Walter, F., Fan, X., Jiang, L., Riechers, D. A., Rix, H.-W., Pentericci, L., Strauss, M. A., Carilli, C. & Wagner, S. (2007), 'Black Hole Masses and Enrichment of z ˜ 6 SDSS Quasars', *apj* **669**, 32–44.

La Franca, F., Fiore, F., Comastri, A., Perola, G. C., Sacchi, N., Brusa, M., Cocchia, F., Feruglio, C., Matt, G., Vignali, C., Carangelo, N., Ciliegi, P., Lamastra, A., Maiolino, R., Mignoli, M., Molendi, S. & Puccetti, S. (2005), 'The HELLAS2XMM Survey. VII. The Hard X-Ray Luminosity Function of AGNs up to z = 4: More Absorbed AGNs at Low Luminosities and High Redshifts', *apj* **635**(2), 864–879.

Lanzuisi, G., Civano, F., Elvis, M., Salvato, M., Hasinger, G., Vignali, C., Zamorani, G., Aldcroft, T., Brusa, M., Comastri, A., Fiore, F., Fruscione, A., Gilli, R., Ho, L. C., Mainieri, V., Merloni, A. & Siemiginowska, A. (2013), 'The Chandra-COSMOS survey - IV. X-ray spectra of the bright sample', *mnras* **431**, 978–996.

Lanzuisi, G., Civano, F., Marchesi, S., Comastri, A., Costantini, E., Elvis, M., Mainieri, V., Hickox, R., Jahnke, K., Komossa, S., Piconcelli, E., Vignali, C., Brusa, M., Cappelluti, N. & Fruscione, A. (2013), 'The XMM-Newton Spectrum of a Candidate Recoiling Supermassive Black Hole: An Elusive Inverted P-Cygni Profile', *apj* **778**(1), 62.

Lanzuisi, G., Gilli, R., Cappi, M., Dadina, M., Bianchi, S., Brusa, M., Chartas, G., Civano, F., Comastri, A., Marinucci, A., Middei, R., Piconcelli, E., Vignali, C., Brandt, W. N., Tombesi, F. & Gaspari, M. (2019), 'NuSTAR Measurement of Coronal Temperature in Two Luminous, High-redshift Quasars', *apjl* **875**(2), L20.

Lapi, A., Raimundo, S., Aversa, R., Cai, Z.-Y., Negrello, M., Celotti, A., De Zotti, G. & Danese, L. (2014), 'The Coevolution of Supermassive Black Holes and Massive Galaxies at High Redshift', *apj* **782**, 69.

Lavalley, M. P., Isobe, T. & Feigelson, E. D. (1992), ASURV, Pennsylvania State University. Report for the period Jan 1990 - Feb 1992., *in* 'Bulletin of the American Astronomical Society', Vol. 24 of *baas*, pp. 839–840.

Lawrence, A. (1991), 'The relative frequency of broad-lined and narrow-lined active galactic nuclei : implications for unified schemes.', *mnras* **252**, 586.

Lehmer, B. D., Xue, Y. Q., Brandt, W. N., Alexand er, D. M., Bauer, F. E., Brusa, M., Comastri, A., Gilli, R., Hornschemeier, A. E. & Luo, B. (2012), 'The 4 Ms Chandra Deep Field-South Number Counts Apportioned by Source Class: Pervasive Active Galactic Nuclei and the Ascent of Normal Galaxies', *apj* **752**(1), 46.

Leipski, C., Meisenheimer, K., Walter, F., Klaas, U., Dannerbauer, H., De Rosa, G., Fan, X., Haas, M., Krause, O. & Rix, H.-W. (2014), 'Spectral Energy Distributions of QSOs at z $>$ 5: Common Active Galactic Nucleus-heated Dust and Occasionally Strong Star-formation', *apj* **785**, 154.

Lodieu, N., Boudreault, S. & Béjar, V. J. S. (2014), 'Spectroscopy of Hyades L dwarf candidates', *mnras* **445**(4), 3908–3918.

Luo, B., Brandt, W. N., Hall, P. B., Wu, J., Anderson, S. F., Garmire, G. P., Gibson, R. R., Plotkin, R. M., Richards, G. T., Schneider, D. P., Shemmer, O. & Shen, Y. (2015), 'X-ray Insights into the Nature of PHL 1811 Analogs and Weak Emission-line Quasars: Unification with a Geometrically Thick Accretion Disk?', *apj* **805**, 122.

Luo, B., Brandt, W. N., Xue, Y. Q., Brusa, M., Alexand er, D. M., Bauer, F. E., Comastri, A., Koekemoer, A., Lehmer, B. D. & Mainieri, V. (2010), 'Identifications and Photometric Redshifts of the 2 Ms Chandra Deep Field-South Sources', *apjs* **187**(2), 560–580.

Luo, B., Brandt, W. N., Xue, Y. Q., Lehmer, B., Alexander, D. M., Bauer, F. E., Vito, F., Yang, G., Basu-Zych, A. R., Comastri, A., Gilli, R., Gu, Q.-S., Hornschemeier, A. E., Koekemoer, A., Liu, T., Mainieri, V., Paolillo, M., Ranalli, P., Rosati, P., Schneider, D. P., Shemmer, O., Smail, I., Sun, M., Tozzi, P., Vignali, C. & Wang, J.-X. (2017), 'The Chandra Deep Field-South Survey: 7 Ms Source Catalogs', *apjs* **228**, 2.

Lusso, E., Comastri, A., Vignali, C., Zamorani, G., Brusa, M., Gilli, R., Iwasawa, K., Salvato, M., Civano, F., Elvis, M., Merloni, A., Bongiorno, A., Trump, J. R., Koekemoer, A. M., Schinnerer, E., Le Floc'h, E., Cappelluti, N., Jahnke, K., Sargent, M., Silverman, J., Mainieri, V., Fiore, F., Bolzonella, M., Le Fèvre, O., Garilli, B., Iovino, A., Kneib, J. P., Lamareille, F., Lilly, S., Mignoli, M., Scodeggio, M. & Vergani, D. (2010), 'The X-ray to optical-UV luminosity ratio of X-ray selected type 1 AGN in XMM-COSMOS', *aap* **512**, A34.

Lusso, E., Comastri, A., Vignali, C., Zamorani, G., Treister, E., Sanders, D., Bolzonella, M., Bongiorno, A., Brusa, M., Civano, F., Gilli, R., Mainieri, V., Nair, P., Aller, M. C., Carollo, M., Koekemoer, A. M., Merloni, A. & Trump, J. R. (2011), 'The bolometric output and host-galaxy properties of obscured AGN in the XMM-COSMOS survey', *aap* **534**, A110.

Lusso, E., Hennawi, J. F., Comastri, A., Zamorani, G., Richards, G. T., Vignali, C., Treister, E., Schawinski, K., Salvato, M. & Gilli, R. (2013), 'The Obscured Fraction of Active Galactic Nuclei in the XMM-COSMOS Survey: A Spectral Energy Distribution Perspective', *apj* **777**(2), 86.

Lusso, E. & Risaliti, G. (2016), 'The Tight Relation between X-Ray and Ultraviolet Luminosity of Quasars', *apj* **819**, 154.

Lusso, E. & Risaliti, G. (2017), 'Quasars as standard candles. I. The physical relation between disc and coronal emission', *aap* **602**, A79.

Lyons, L. (1991), *A Practical Guide to Data Analysis for Physical Science Students*.

Mace, G. N. (2014), Investigating Low-Mass Binary Stars And Brown Dwarfs with Near-Infrared Spectroscopy, PhD thesis, University of California, Los Angeles.

Madau, P., Haardt, F. & Dotti, M. (2014), 'Super-critical Growth of Massive Black Holes from Stellar-mass Seeds', *apjl* **784**, L38.

Madau, P. & Rees, M. J. (2001), 'Massive Black Holes as Population III Remnants', *apjl* **551**, L27–L30.

Magnier, E. (2006), The Pan-STARRS PS1 Image Processing Pipeline, *in* 'The Advanced Maui Optical and Space Surveillance Technologies Conference', p. E50.

Magnier, E. (2007), Calibration of the Pan-STARRS 3π Survey, *in* C. Sterken, ed., 'The Future of Photometric, Spectrophotometric and Polarimetric Standardization', Vol. 364 of *Astronomical Society of the Pacific Conference Series*, p. 153.

Magorrian, J., Tremaine, S., Richstone, D., Bender, R., Bower, G., Dressler, A., Faber, S. M., Gebhardt, K., Green, R., Grillmair, C., Kormendy, J. & Lauer, T. (1998), 'The Demography of Massive Dark Objects in Galaxy Centers', *aj* **115**(6), 2285–2305.

Marchese, E., Della Ceca, R., Caccianiga, A., Severgnini, P., Corral, A. & Fanali, R. (2012), 'The optical-UV spectral energy distribution of the unabsorbed AGN population in the XMM-Newton Bright Serendipitous Survey', *aap* **539**, A48.

Marchesi, S., Civano, F., Salvato, M., Shankar, F., Comastri, A., Elvis, M., Lanzuisi, G., Trakhtenbrot, B., Vignali, C., Zamorani, G., Allevato, V., Brusa, M., Fiore, F., Gilli, R., Griffiths, R., Hasinger, G., Miyaji, T., Schawinski, K., Treister, E. & Urry, C. M. (2016), 'The Chandra COSMOS-Legacy Survey: The z>3 Sample', *apj* **827**, 150.

Marconi, A. & Hunt, L. K. (2003), 'The Relation between Black Hole Mass, Bulge Mass, and Near-Infrared Luminosity', *apjl* **589**(1), L21–L24.

Marocco, F., Jones, H. R. A., Day-Jones, A. C., Pinfield, D. J., Lucas, P. W., Burningham, B., Zhang, Z. H., Smart, R. L., Gomes, J. I. & Smith, L. (2015), 'A large spectroscopic sample of L and T dwarfs from UKIDSS LAS: peculiar objects, binaries, and space density', *mnras* **449**(4), 3651–3692.

Matsuoka, Y., Onoue, M., Kashikawa, N., Iwasawa, K., Strauss, M. A., Nagao, T., Imanishi, M., Niida, M., Toba, Y., Akiyama, M., Asami, N., Bosch, J., Foucaud,

S., Furusawa, H., Goto, T., Gunn, J. E., Harikane, Y., Ikeda, H., Kawaguchi, T., Kikuta, S., Komiyama, Y., Lupton, R. H., Minezaki, T., Miyazaki, S., Morokuma, T., Murayama, H., Nishizawa, A. J., Ono, Y., Ouchi, M., Price, P. A., Sameshima, H., Silverman, J. D., Sugiyama, N., Tait, P. J., Takada, M., Takata, T., Tanaka, M., Tang, J.-J. & Utsumi, Y. (2016), 'Subaru High-z Exploration of Low-luminosity Quasars (SHELLQs). I. Discovery of 15 Quasars and Bright Galaxies at $5.7 < z < 6.9$', *apj* **828**, 26.

Matsuoka, Y., Onoue, M., Kashikawa, N., Strauss, M. A., Iwasawa, K., Lee, C.-H., Imanishi, M., Nagao, T., Akiyama, M., Asami, N., Bosch, J., Furusawa, H., Goto, T., Gunn, J. E., Harikane, Y., Ikeda, H., Izumi, T., Kawaguchi, T., Kato, N., Kikuta, S., Kohno, K., Komiyama, Y., Koyama, S., Lupton, R. H., Minezaki, T., Miyazaki, S., Murayama, H., Niida, M., Nishizawa, A. J., Noboriguchi, A., Oguri, M., Ono, Y., Ouchi, M., Price, P. A., Sameshima, H., Schulze, A., Shirakata, H., Silverman, J. D., Sugiyama, N., Tait, P. J., Takada, M., Takata, T., Tanaka, M., Tang, J.-J., Toba, Y., Utsumi, Y., Wang, S.-Y. & Yamashita, T. (2019), 'Discovery of the First Low-luminosity Quasar at z > 7', *apjl* **872**(1), L2.

Matsuoka, Y., Strauss, M. A., Kashikawa, N., Onoue, M., Iwasawa, K., Tang, J.-J., Lee, C.-H., Imanishi, M., Nagao, T., Akiyama, M., Asami, N., Bosch, J., Furusawa, H., Goto, T., Gunn, J. E., Harikane, Y., Ikeda, H., Izumi, T., Kawaguchi, T., Kato, N., Kikuta, S., Kohno, K., Komiyama, Y., Lupton, R. H., Minezaki, T., Miyazaki, S., Murayama, H., Niida, M., Nishizawa, A. J., Noboriguchi, A., Oguri, M., Ono, Y., Ouchi, M., Price, P. A., Sameshima, H., Schulze, A., Shirakata, H., Silverman, J. D., Sugiyama, N., Tait, P. J., Takada, M., Takata, T., Tanaka, M., Toba, Y., Utsumi, Y., Wang, S.-Y. & Yamashita, T. (2018), 'Subaru High-z Exploration of Low-luminosity Quasars (SHELLQs). V. Quasar Luminosity Function and Contribution to Cosmic Reionization at $z = 6$', *apj* **869**(2), 150.

Mazzucchelli, C., Bañados, E., Decarli, R., Farina, E. P., Venemans, B. P., Walter, F. & Overzier, R. (2017), 'No Overdensity of Lyman-Alpha Emitting Galaxies around a Quasar at $z = 5.7$', *apj* **834**, 83.

McConnell, N. J. & Ma, C.-P. (2013), 'Revisiting the Scaling Relations of Black Hole Masses and Host Galaxy Properties', *apj* **764**(2), 184.

Menci, N., Fiore, F., Puccetti, S. & Cavaliere, A. (2008), 'The Blast Wave Model for AGN Feedback: Effects on AGN Obscuration', *apj* **686**(1), 219–229.

Menzel, M. L., Merloni, A., Georgakakis, A., Salvato, M., Aubourg, E., Brandt, W. N., Brusa, M., Buchner, J., Dwelly, T., Nandra, K., Pâris, I., Petitjean, P.

& Schwope, A. (2016), 'A spectroscopic survey of X-ray-selected AGNs in the northern XMM-XXL field', *mnras* **457**(1), 110–132.

Merloni, A., Bongiorno, A., Brusa, M., Iwasawa, K., Mainieri, V., Magnelli, B., Salvato, M., Berta, S., Cappelluti, N., Comastri, A., Fiore, F., Gilli, R., Koekemoer, A., Le Floc'h, E., Lusso, E., Lutz, D., Miyaji, T., Pozzi, F., Riguccini, L., Rosario, D. J., Silverman, J., Symeonidis, M., Treister, E., Vignali, C. & Zamorani, G. (2014), 'The incidence of obscuration in active galactic nuclei', *Monthly Notices of the Royal Astronomical Society* **437**(4), 3550–3567.

Miller, B. P., Brandt, W. N., Schneider, D. P., Gibson, R. R., Steffen, A. T. & Wu, J. (2011), 'X-ray Emission from Optically Selected Radio-intermediate and Radio-loud Quasars', *apj* **726**, 20.

Miyaji, T., Hasinger, G. & Schmidt, M. (2000), 'Soft X-ray AGN luminosity function from it ROSAT surveys. I. Cosmological evolution and contribution to the soft X-ray background', *aap* **353**, 25–40.

Moorwood, A., Cuby, J. G. & Lidman, C. (1998), 'SOFI sees first light at the NTT.', *The Messenger* **91**, 9–13.

Moretti, A., Ballo, L., Braito, V., Caccianiga, A., Della Ceca, R., Gilli, R., Salvaterra, R., Severgnini, P. & Vignali, C. (2014), 'X-ray observation of ULAS J1120+0641, the most distant quasar at z = 7.08', *aap* **563**, A46.

Moretti, A., Campana, S., Mineo, T., Romano, P., Abbey, A. F., Angelini, L., Beardmore, A., Burkert, W., Burrows, D. N., Capalbi, M., Chincarini, G., Citterio, O., Cusumano, G., Freyberg, M. J., Giommi, P., Goad, M. R., Godet, O., Hartner, G. D., Hill, J. E., Kennea, J., La Parola, V., Mangano, V., Morris, D., Nousek, J. A., Osborne, J., Page, K., Pagani, C., Perri, M., Tagliaferri, G., Tamburelli, F. & Wells, A. (2005), In-flight calibration of the Swift XRT Point Spread Function, *in* O. H. W. Siegmund, ed., 'UV, X-Ray, and Gamma-Ray Space Instrumentation for Astronomy XIV', Vol. 5898 of *procspie*, pp. 360–368.

Morselli, L., Mignoli, M., Gilli, R., Vignali, C., Comastri, A., Sani, E., Cappelluti, N., Zamorani, G., Brusa, M., Gallozzi, S. & Vanzella, E. (2014), 'Primordial environment of super massive black holes: large-scale galaxy overdensities around z ˜ 6 quasars with LBT', *aap* **568**, A1.

Mortlock, D. (2016), Quasars as Probes of Cosmological Reionization, *in* A. Mesinger, ed., 'Understanding the Epoch of Cosmic Reionization: Challenges and Progress', Vol. 423 of *Astrophysics and Space Science Library*, p. 187.

Mortlock, D. J., Warren, S. J., Venemans, B. P., Patel, M., Hewett, P. C., McMahon, R. G., Simpson, C., Theuns, T., Gonzáles-Solares, E. A., Adamson, A., Dye, S., Hambly, N. C., Hirst, P., Irwin, M. J., Kuiper, E., Lawrence, A. & Röttgering, H. J. A. (2011), 'A luminous quasar at a redshift of z = 7.085', *nat* **474**, 616–619.

Nandra, K., George, I. M., Mushotzky, R. F., Turner, T. J. & Yaqoob, T. (1997), 'ASCA Observations of Seyfert 1 Galaxies. I. Data Analysis, Imaging, and Timing', *apj* **476**, 70–82.

Nandra, K., Laird, E. S., Aird, J. A., Salvato, M., Georgakakis, A., Barro, G., Perez-Gonzalez, P. G., Barmby, P., Chary, R.-R., Coil, A., Cooper, M. C., Davis, M., Dickinson, M., Faber, S. M., Fazio, G. G., Guhathakurta, P., Gwyn, S., Hsu, L.-T., Huang, J.-S., Ivison, R. J., Koo, D. C., Newman, J. A., Rangel, C., Yamada, T. & Willmer, C. (2015), 'AEGIS-X: Deep Chandra Imaging of the Central Groth Strip', *apjs* **220**, 10.

Nanni, R., Gilli, R., Vignali, C., Mignoli, M., Comastri, A., Vanzella, E., Zamorani, G., Calura, F., Lanzuisi, G. & Brusa, M. (2018), 'The 500 ks Chandra observation of the z = 6.31 QSO SDSS J1030 + 0524', *aap* **614**, A121.

Nanni, R., Vignali, C., Gilli, R., Moretti, A. & Brandt, W. N. (2017), 'The X-ray properties of z 6 luminous quasars', *aap* **603**, A128.

Norman, C., Ptak, A., Hornschemeier, A., Hasinger, G., Bergeron, J., Comastri, A., Giacconi, R., Gilli, R., Glazebrook, K., Heckman, T., Kewley, L., Ranalli, P., Rosati, P., Szokoly, G., Tozzi, P., Wang, J., Zheng, W. & Zirm, A. (2004), 'The X-Ray-derived Cosmological Star Formation History and the Galaxy X-Ray Luminosity Functions in the Chandra Deep Fields North and South', *apj* **607**(2), 721–738.

Onoue, M., Kashikawa, N., Matsuoka, Y., Kato, N., Izumi, T., Nagao, T., Strauss, M. A., Harikane, Y., Imanishi, M., Ito, K., Iwasawa, K., Kawaguchi, T., Lee, C.-H., Noboriguchi, A., Suh, H., Tanaka, M. & Toba, Y. (2019), 'Subaru High-z Exploration of Low-Luminosity Quasars (SHELLQs). VI. Black Hole Mass Measurements of Six Quasars at 6.1<z<6.7', *arXiv e-prints* p. arXiv:1904.07278.

Overzier, R. A., Guo, Q., Kauffmann, G., De Lucia, G., Bouwens, R. & Lemson, G. (2009), 'ΛCDM predictions for galaxy protoclusters - I. The relation between galaxies, protoclusters and quasars at z ˜ 6', *mnras* **394**, 577–594.

Overzier, R. A., Harris, D. E., Carilli, C. L., Pentericci, L., Röttgering, H. J. A. & Miley, G. K. (2005), 'On the X-ray emission of z =2 radio galaxies: IC scattering of the CMB and no evidence for fully-formed potential wells', *aap* **433**, 87–100.

Padovani, P. (2017), 'Active Galactic Nuclei at all wavelengths and from all angles', *Frontiers in Astronomy and Space Sciences* **4**, 35.

Page, K. L., Reeves, J. N., O'Brien, P. T. & Turner, M. J. L. (2005), 'XMM-Newton spectroscopy of high-redshift quasars', *mnras* **364**, 195–207.

Page, M. J., Simpson, C., Mortlock, D. J., Warren, S. J., Hewett, P. C., Venemans, B. P. & McMahon, R. G. (2014), 'X-rays from the redshift 7.1 quasar ULAS J1120+0641', *mnras* **440**, L91–L95.

Paolillo, M., Fabbiano, G., Peres, G. & Kim, D.-W. (2002), 'Deep ROSAT HRI Observations of the NGC 1399/NGC 1404 Region: Morphology and Structure of the X-Ray Halo', *apj* **565**, 883–907.

Paolillo, M., Papadakis, I., Brandt, W. N., Luo, B., Xue, Y. Q., Tozzi, P., Shemmer, O., Allevato, V., Bauer, F. E., Comastri, A., Gilli, R., Koekemoer, A. M., Liu, T., Vignali, C., Vito, F., Yang, G., Wang, J. X. & Zheng, X. C. (2017), 'Tracing the accretion history of supermassive black holes through X-ray variability: results from the ChandraDeep Field-South', *mnras* **471**, 4398–4411.

Papadakis, I. E. (2004), 'The scaling of the X-ray variability with black hole mass in active galactic nuclei', *mnras* **348**, 207–213.

Petric, A. O., Carilli, C. L., Bertoldi, F., Fan, X., Cox, P., Strauss, M. A., Omont, A. & Schneider, D. P. (2003), 'Sensitive Observations at 1.4 and 250 GHz of z>5 QSOs', *aj* **126**, 15–23.

Pezzulli, E., Valiante, R., Orofino, M. C., Schneider, R., Gallerani, S. & Sbarrato, T. (2017), 'Faint progenitors of luminous z = 6 quasars: Why do not we see them?', *mnras* **466**, 2131–2142.

Piconcelli, E., Jimenez-Bailón, E., Guainazzi, M., Schartel, N., Rodríguez-Pascual, P. M. & Santos-Lleó, M. (2005), 'The XMM-Newton view of PG quasars. I. X-ray continuum and absorption', *aap* **432**, 15–30.

Pons, E., McMahon, R. G., Banerji, M. & Reed, S. L. (2019), 'X-ray properties of z>6.5 quasars', *arXiv e-prints* p. arXiv:1910.04122.

Priddey, R. S., Isaak, K. G., McMahon, R. G., Robson, E. I. & Pearson, C. P. (2003), 'Quasars as probes of the submillimetre cosmos at z > 5 - I. Preliminary SCUBA photometry', *mnras* **344**, L74–L78.

Priddey, R. S., Ivison, R. J. & Isaak, K. G. (2008), 'Environments of z > 5 quasars: searching for protoclusters at submillimetre wavelengths', *mnras* **383**, 289–296.

Puccetti, S., Vignali, C., Cappelluti, N., Fiore, F., Zamorani, G., Aldcroft, T. L., Elvis, M., Gilli, R., Miyaji, T. & Brunner, H. (2009), 'The Chandra Survey of the COSMOS Field. II. Source Detection and Photometry', *apjs* **185**(2), 586–601.

Pudritz, R. E., Hardcastle, M. J. & Gabuzda, D. C. (2012), 'Magnetic Fields in Astrophysical Jets: From Launch to Termination', *ssr* **169**(1-4), 27–72.

Quadri, R., Marchesini, D., van Dokkum, P., Gawiser, E., Franx, M., Lira, P., Rudnick, G., Urry, C. M., Maza, J., Kriek, M., Barrientos, L. F., Blanc, G. A., Castander, F. J., Christlein, D., Coppi, P. S., Hall, P. B., Herrera, D., Infante, L., Taylor, E. N., Treister, E. & Willis, J. P. (2007), 'The Multiwavelength Survey by Yale-Chile (MUSYC): Deep Near-Infrared Imaging and the Selection of Distant Galaxies', *aj* **134**, 1103–1117.

Ranalli, P., Comastri, A. & Setti, G. (2005), 'The X-ray luminosity function and number counts of spiral galaxies', *aap* **440**(1), 23–37.

Reed, S. L., McMahon, R. G., Banerji, M., Becker, G. D., Gonzalez-Solares, E., Martini, P., Ostrovski, F., Rauch, M., Abbott, T., Abdalla, F. B., Allam, S., Benoit-Levy, A., Bertin, E., Buckley-Geer, E., Burke, D., Carnero Rosell, A., da Costa, L. N., D'Andrea, C., DePoy, D. L., Desai, S., Diehl, H. T., Doel, P., Cunha, C. E., Estrada, J., Evrard, A. E., Fausti Neto, A., Finley, D. A., Fosalba, P., Frieman, J., Gruen, D., Honscheid, K., James, D., Kent, S., Kuehn, K., Kuropatkin, N., Lahav, O., Maia, M. A. G., Makler, M., Marshall, J., Merritt, K., Miquel, R., Mohr, J., Nord, B., Ogando, R., Plazas, A., Romer, K., Roodman, A., Rykoff, E., Sako, M., Sanchez, E., Santiago, B., Schubnell, M., Sevilla, I., Smith, C., Soares-Santos, M., Suchyta, E., Swanson, M. E. C., Tarle, G., Thomas, D., Tucker, D., Walker, A. & Wechsler, R. H. (2015), 'DES J0454-4448: discovery of the first luminous z $>$ 6 quasar from the Dark Energy Survey', *mnras* **454**(4), 3952–3961.

Reed, S. L., McMahon, R. G., Martini, P., Banerji, M., Auger, M., Hewett, P. C., Koposov, S. E., Gibbons, S. L. J., Gonzalez-Solares, E., Ostrovski, F., Tie, S. S., Abdalla, F. B., Allam, S., Benoit-Lévy, A., Bertin, E., Brooks, D., Buckley-Geer, E., Burke, D. L., Carnero Rosell, A., Carrasco Kind, M., Carretero, J., da Costa, L. N., DePoy, D. L., Desai, S., Diehl, H. T., Doel, P., Evrard, A. E., Finley, D. A., Flaugher, B., Fosalba, P., Frieman, J., García-Bellido, J., Gaztanaga, E., Goldstein, D. A., Gruen, D., Gruendl, R. A., Gutierrez, G., James, D. J., Kuehn, K., Kuropatkin, N., Lahav, O., Lima, M., Maia, M. A. G., Marshall, J. L., Melchior, P., Miller, C. J., Miquel, R., Nord, B., Ogando, R., Plazas, A. A., Romer, A. K., Sanchez, E., Scarpine, V., Schubnell, M., Sevilla-Noarbe, I., Smith, R. C., Sobreira, F., Suchyta, E., Swanson, M. E. C., Tarle, G., Tucker,

D. L., Walker, A. R. & Wester, W. (2017*a*), 'Eight new luminous z >= 6 quasars discovered via SED model fitting of VISTA, WISE and Dark Energy Survey Year 1 observations', *mnras* **468**, 4702–4718.

Reed, S. L., McMahon, R. G., Martini, P., Banerji, M., Auger, M., Hewett, P. C., Koposov, S. E., Gibbons, S. L. J., Gonzalez-Solares, E., Ostrovski, F., Tie, S. S., Abdalla, F. B., Allam, S., Benoit-Lévy, A., Bertin, E., Brooks, D., Buckley-Geer, E., Burke, D. L., Carnero Rosell, A., Carrasco Kind, M., Carretero, J., da Costa, L. N., DePoy, D. L., Desai, S., Diehl, H. T., Doel, P., Evrard, A. E., Finley, D. A., Flaugher, B., Fosalba, P., Frieman, J., García-Bellido, J., Gaztanaga, E., Goldstein, D. A., Gruen, D., Gruendl, R. A., Gutierrez, G., James, D. J., Kuehn, K., Kuropatkin, N., Lahav, O., Lima, M., Maia, M. A. G., Marshall, J. L., Melchior, P., Miller, C. J., Miquel, R., Nord, B., Ogando, R., Plazas, A. A., Romer, A. K., Sanchez, E., Scarpine, V., Schubnell, M., Sevilla-Noarbe, I., Smith, R. C., Sobreira, F., Suchyta, E., Swanson, M. E. C., Tarle, G., Tucker, D. L., Walker, A. R. & Wester, W. (2017*b*), 'Eight new luminous z > 6 quasars discovered via SED model fitting of VISTA, WISE and Dark Energy Survey Year 1 observations', *mnras* **468**(4), 4702–4718.

Ricci, C., Koss, M., Trakhtenbrot, B., Bauer, F., Treister, E., Ueda, Y., Schawinski, K., Oh, K. & Lamperti, I. (2017), The relation between nuclear obscuration, galaxy interactions and accretion properties of AGN, *in* 'The X-ray Universe 2017', p. 190.

Richards, G. T., Lacy, M., Storrie-Lombardi, L. J., Hall, P. B., Gallagher, S. C., Hines, D. C., Fan, X., Papovich, C., Vanden Berk, D. E., Trammell, G. B., Schneider, D. P., Vestergaard, M., York, D. G., Jester, S., Anderson, S. F., Budavári, T. & Szalay, A. S. (2006), 'Spectral Energy Distributions and Multiwavelength Selection of Type 1 Quasars', *apjs* **166**, 470–497.

Risaliti, G. & Elvis, M. (2004), A Panchromatic View of AGN, *in* A. J. Barger, ed., 'Supermassive Black Holes in the Distant Universe', Vol. 308 of *Astrophysics and Space Science Library*, p. 187.

Risaliti, G., Elvis, M., Fabbiano, G., Baldi, A., Zezas, A. & Salvati, M. (2007), 'Occultation Measurement of the Size of the X-Ray-emitting Region in the Active Galactic Nucleus of NGC 1365', *apjl* **659**, L111–L114.

Salvestrini, F., Risaliti, G., Bisogni, S., Lusso, E. & Vignali, C. (2019), 'Quasars as standard candles II: The non linear relation between UV and X-ray emission at high redshifts', *arXiv e-prints* p. arXiv:1909.12309.

Schmidt, M. & Green, R. F. (1983), 'Quasar evolution derived from the Palomar bright quasar survey and other complete quasar surveys.', *apj* **269**, 352–374.

Shemmer, O., Brandt, W. N., Netzer, H., Maiolino, R. & Kaspi, S. (2008), 'The Hard X-Ray Spectrum as a Probe for Black Hole Growth in Radio-Quiet Active Galactic Nuclei', *apj* **682**, 81–93.

Shemmer, O., Brandt, W. N., Paolillo, M., Kaspi, S., Vignali, C., Lira, P. & Schneider, D. P. (2017), 'Exploratory X-Ray Monitoring of Luminous Radio-quiet Quasars at High Redshift: No Evidence for Evolution in X-Ray Variability', *apj* **848**, 46.

Shemmer, O., Brandt, W. N., Schneider, D. P., Fan, X., Strauss, M. A., Diamond-Stanic, A. M., Richards, G. T., Anderson, S. F., Gunn, J. E. & Brinkmann, J. (2006), 'Chandra Observations of the Highest Redshift Quasars from the Sloan Digital Sky Survey', *apj* **644**, 86–99.

Shemmer, O., Trakhtenbrot, B., Anderson, S. F., Brandt, W. N., Diamond-Stanic, A. M., Fan, X., Lira, P., Netzer, H., Plotkin, R. M., Richards, G. T., Schneider, D. P. & Strauss, M. A. (2010), 'Weak Line Quasars at High Redshift: Extremely High Accretion Rates or Anemic Broad-line Regions?', *apjl* **722**, L152–L156.

Silverman, J. D., Green, P. J., Barkhouse, W. A., Kim, D. W., Kim, M., Wilkes, B. J., Cameron, R. A., Hasinger, G., Jannuzi, B. T., Smith, M. G., Smith, P. S. & Tananbaum, H. (2008), 'The Luminosity Function of X-Ray-selected Active Galactic Nuclei: Evolution of Supermassive Black Holes at High Redshift', *apj* **679**(1), 118–139.

Simpson, C. (2005), 'The luminosity dependence of the type 1 active galactic nucleus fraction', *mnras* **360**(2), 565–572.

Simpson, C., Mortlock, D., Warren, S., Cantalupo, S., Hewett, P., McLure, R., McMahon, R. & Venemans, B. (2014), 'No excess of bright galaxies around the redshift 7.1 quasar ULAS J1120+0641', *mnras* **442**, 3454–3461.

Skrzypek, N., Warren, S. J., Faherty, J. K., Mortlock, D. J., Burgasser, A. J. & Hewett, P. C. (2015), 'Photometric brown-dwarf classification. I. A method to identify and accurately classify large samples of brown dwarfs without spectroscopy', *aap* **574**, A78.

Smail, I., Blundell, K. M., Lehmer, B. D. & Alexander, D. M. (2012), 'Inverse Compton X-Ray Halos around High-z Radio Galaxies: A Feedback Mechanism Powered by Far-infrared Starbursts or the Cosmic Microwave Background?', *apj* **760**, 132.

Sobolewska, M. A. & Papadakis, I. E. (2009), 'The long-term X-ray spectral variability of AGN', *mnras* **399**, 1597–1610.

Springel, V., White, S. D. M., Jenkins, A., Frenk, C. S., Yoshida, N., Gao, L., Navarro, J., Thacker, R., Croton, D., Helly, J., Peacock, J. A., Cole, S., Thomas, P., Couchman, H., Evrard, A., Colberg, J. & Pearce, F. (2005), 'Simulations of the formation, evolution and clustering of galaxies and quasars', *nat* **435**, 629–636.

Steffen, A. T., Strateva, I., Brandt, W. N., Alexander, D. M., Koekemoer, A. M., Lehmer, B. D., Schneider, D. P. & Vignali, C. (2006), 'The X-Ray-to-Optical Properties of Optically Selected Active Galaxies over Wide Luminosity and Redshift Ranges', *aj* **131**, 2826–2842.

Stiavelli, M., Djorgovski, S. G., Pavlovsky, C., Scarlata, C., Stern, D., Mahabal, A., Thompson, D., Dickinson, M., Panagia, N. & Meylan, G. (2005), 'Evidence of Primordial Clustering around the QSO SDSS J1030+0524 at z=6.28', *apjl* **622**, L1–L4.

Sutherland, W. & Saunders, W. (1992), 'On the likelihood ratio for source identification.', *mnras* **259**, 413–420.

Tombesi, F., Cappi, M., Reeves, J. N., Nemmen, R. S., Braito, V., Gaspari, M. & Reynolds, C. S. (2013), 'Unification of X-ray winds in Seyfert galaxies: from ultra-fast outflows to warm absorbers', *mnras* **430**, 1102–1117.

Tombesi, F., Meléndez, M., Veilleux, S., Reeves, J. N., González-Alfonso, E. & Reynolds, C. S. (2015), 'Wind from the black-hole accretion disk driving a molecular outflow in an active galaxy', *nat* **519**, 436–438.

Tozzi, P., Gilli, R., Mainieri, V., Norman, C., Risaliti, G., Rosati, P., Bergeron, J., Borgani, S., Giacconi, R., Hasinger, G., Nonino, M., Streblyanska, A., Szokoly, G., Wang, J. X. & Zheng, W. (2006), 'X-ray spectral properties of active galactic nuclei in the Chandra Deep Field South', *Astronomy and Astrophysics* **451**(2), 457–474.

Treister, E. & Urry, C. M. (2006), 'The Evolution of Obscuration in Active Galactic Nuclei', *apjl* **652**(2), L79–L82.

Treister, E., Urry, C. M. & Virani, S. (2009), 'The Space Density of Compton-Thick Active Galactic Nucleus and the X-Ray Background', *The Astrophysical Journal* **696**(1), 110–120.

Turner, T. J., George, I. M., Nandra, K. & Turcan, D. (1999), 'On X-Ray Variability in Seyfert Galaxies', *apj* **524**, 667–673.

Ueda, Y., Akiyama, M., Hasinger, G., Miyaji, T. & Watson, M. G. (2014), 'Toward the Standard Population Synthesis Model of the X-Ray Background: Evolution of X-Ray Luminosity and Absorption Functions of Active Galactic Nuclei Including Compton-thick Populations', *apj* **786**(2), 104.

Ueda, Y., Akiyama, M., Ohta, K. & Miyaji, T. (2003), 'Cosmological Evolution of the Hard X-Ray Active Galactic Nucleus Luminosity Function and the Origin of the Hard X-Ray Background', *apj* **598**(2), 886–908.

Urry, C. M. & Padovani, P. (1995), 'Unified Schemes for Radio-Loud Active Galactic Nuclei', *pasp* **107**, 803.

Valiante, R., Schneider, R. & Volonteri, M. (2016), 'Editorial: Understanding the Growth of the First Supermassive Black Holes', *pasa* **33**, e032.

Venemans, B. P., Findlay, J. R., Sutherland, W. J., De Rosa, G., McMahon, R. G., Simcoe, R., González-Solares, E. A., Kuijken, K. & Lewis, J. R. (2013), 'Discovery of Three z > 6.5 Quasars in the VISTA Kilo-Degree Infrared Galaxy (VIKING) Survey', *apj* **779**, 24.

Venemans, B. P., Walter, F., Decarli, R., Ferkinhoff, C., Weiß, A., Findlay, J. R., McMahon, R. G., Sutherland, W. J. & Meijerink, R. (2017), 'Molecular Gas in Three z = 7 Quasar Host Galaxies', *apj* **845**, 154.

Venemans, B. P., Walter, F., Zschaechner, L., Decarli, R., De Rosa, G., Findlay, J. R., McMahon, R. G. & Sutherland, W. J. (2016), 'Bright [C II] and Dust Emission in Three z > 6.6 Quasar Host Galaxies Observed by ALMA', *apj* **816**, 37.

Vignali, C., Brandt, W. N., Schneider, D. P., Anderson, S. F., Fan, X., Gunn, J. E., Kaspi, S., Richards, G. T. & Strauss, M. A. (2003), 'Chandra and XMM-Newton Observations of the First Quasars: X-Rays from the Age of Cosmic Enlightenment', *aj* **125**, 2876–2890.

Vignali, C., Brandt, W. N., Schneider, D. P. & Kaspi, S. (2005), 'X-Ray Lighthouses of the High-Redshift Universe. II. Further Snapshot Observations of the Most Luminous z>4 Quasars with Chandra', *aj* **129**, 2519–2530.

Vito, F., Brandt, W. N., Bauer, F. E., Calura, F., Gilli, R., Luo, B., Shemmer, O., Vignali, C., Zamorani, G., Brusa, M., Civano, F., Comastri, A. & Nanni, R. (2019), 'The X-ray properties of z>6 quasars: no evident evolution of accretion physics in the first Gyr of the Universe', *arXiv e-prints* p. arXiv:1908.09849.

Vito, F., Brandt, W. N., Yang, G., Gilli, R., Luo, B., Vignali, C., Xue, Y. Q., Comastri, A., Koekemoer, A. M., Lehmer, B. D., Liu, T., Paolillo, M., Ranalli, P., Schneider, D. P., Shemmer, O., Volonteri, M. & Wang, J. (2018), 'High-redshift AGN in the Chandra Deep Fields: the obscured fraction and space density of the sub-L_* population', *mnras* **473**, 2378–2406.

Vito, F., Gilli, R., Vignali, C., Brandt, W. N., Comastri, A., Yang, G., Lehmer, B. D., Luo, B., Basu-Zych, A., Bauer, F. E., Cappelluti, N., Koekemoer, A., Mainieri, V., Paolillo, M., Ranalli, P., Shemmer, O., Trump, J., Wang, J. X. & Xue, Y. Q. (2016), 'The deepest X-ray view of high-redshift galaxies: constraints on low-rate black hole accretion', *mnras* **463**, 348–374.

Vito, F., Gilli, R., Vignali, C., Comastri, A., Brusa, M., Cappelluti, N. & Iwasawa, K. (2014), 'The hard X-ray luminosity function of high-redshift ($3 < z < 5$) active galactic nuclei', *mnras* **445**(4), 3557–3574.

Vito, F., Vignali, C., Gilli, R., Comastri, A., Iwasawa, K., Brandt, W. N., Alexander, D. M., Brusa, M., Lehmer, B., Bauer, F. E., Schneider, D. P., Xue, Y. Q. & Luo, B. (2013), 'The high-redshift ($z > 3$) active galactic nucleus population in the 4-Ms Chandra Deep Field-South', *mnras* **428**, 354–369.

Volonteri, M., Habouzit, M., Pacucci, F. & Tremmel, M. (2016), The evolution of high-redshift massive black holes, *in* S. Kaviraj, ed., 'Galaxies at High Redshift and Their Evolution Over Cosmic Time', Vol. 319 of *IAU Symposium*, pp. 72–79.

Volonteri, M., Lodato, G. & Natarajan, P. (2008), 'The evolution of massive black hole seeds', *mnras* **383**, 1079–1088.

Volonteri, M. & Rees, M. J. (2006), 'Quasars at z=6: The Survival of the Fittest', *apj* **650**(2), 669–678.

West, A. A., Morgan, D. P., Bochanski, J. J., Andersen, J. M., Bell, K. J., Kowalski, A. F., Davenport, J. R. A., Hawley, S. L., Schmidt, S. J., Bernat, D., Hilton, E. J., Muirhead, P., Covey, K. R., Rojas-Ayala, B., Schlawin, E., Gooding, M., Schluns, K., Dhital, S., Pineda, J. S. & Jones, D. O. (2011), 'The Sloan Digital Sky Survey Data Release 7 Spectroscopic M Dwarf Catalog. I. Data', *aj* **141**(3), 97.

White, R. L., Becker, R. H., Helfand, D. J. & Gregg, M. D. (1997), 'A Catalog of 1.4 GHz Radio Sources from the FIRST Survey', *apj* **475**, 479–493.

Willott, C. J., Delorme, P., Reylé, C., Albert, L., Bergeron, J., Crampton, D., Delfosse, X., Forveille, T., Hutchings, J. B., McLure, R. J., Omont, A. & Schade,

D. (2010), 'The Canada-France High-z Quasar Survey: Nine New Quasars and the Luminosity Function at Redshift 6', *aj* **139**, 906–918.

Willott, C. J., Rawlings, S., Jarvis, M. J. & Blundell, K. M. (2003), 'Near-infrared imaging and the K-z relation for radio galaxies in the 7C Redshift Survey', *mnras* **339**, 173–188.

Wu, J., Brandt, W. N., Miller, B. P., Garmire, G. P., Schneider, D. P. & Vignali, C. (2013), 'An X-Ray and Multiwavelength Survey of Highly Radio-loud Quasars at z > 4: Jet-linked Emission in the Brightest Radio Beacons of the Early Universe', *apj* **763**, 109.

Wu, X.-B., Chen, Z.-Y., Jia, Z.-D., Zuo, W.-W., Zhao, Y.-H., Luo, A. L., Bai, Z.-R., Chen, J.-J., Zhang, H.-T., Yan, H.-L., Ren, J.-J., Sun, S.-W., Wu, H., Zhang, Y., Li, Y.-P., Lu, Q.-S., Wang, Y., Ni, J.-J., Wang, H., Kong, X. & Shen, S.-Y. (2010), 'A very bright (i = 16.44) quasar in the 'redshift desert' discovered by the Guoshoujing Telescope (LAMOST)', *Research in Astronomy and Astrophysics* **10**(8), 737–744.

Wu, X.-B., Wang, F., Fan, X., Yi, W., Zuo, W., Bian, F., Jiang, L., McGreer, I. D., Wang, R., Yang, J., Yang, Q., Thompson, D. & Beletsky, Y. (2015), 'An ultraluminous quasar with a twelve-billion-solar-mass black hole at redshift 6.30', *nat* **518**, 512–515.

Xue, Y. Q., Luo, B., Brandt, W. N., Alexander, D. M., Bauer, F. E., Lehmer, B. D. & Yang, G. (2016), 'The 2 Ms Chandra Deep Field-North Survey and the 250 ks Extended Chandra Deep Field-South Survey: Improved Point-source Catalogs', *apjs* **224**, 15.

Xue, Y. Q., Luo, B., Brandt, W. N., Bauer, F. E., Lehmer, B. D., Broos, P. S., Schneider, D. P., Alexand er, D. M., Brusa, M. & Comastri, A. (2011), 'The Chandra Deep Field-South Survey: 4 Ms Source Catalogs', *apjs* **195**(1), 10.

Yang, J., Fan, X., Wu, X.-B., Wang, F., Bian, F., Yang, Q., McGreer, I. D., Yi, W., Jiang, L., Green, R., Yue, M., Wang, S., Li, Z., Ding, J., Dye, S. & Lawrence, A. (2017), 'Discovery of 16 New z = 5.5 Quasars: Filling in the Redshift Gap of Quasar Color Selection', *aj* **153**, 184.

Zamorani, G., Henry, J. P., Maccacaro, T., Tananbaum, H., Soltan, A., Avni, Y., Liebert, J., Stocke, J., Strittmatter, P. A., Weymann, R. J., Smith, M. G. & Condon, J. J. (1981), 'X-ray studies of quasars with the Einstein Observatory. II', *apj* **245**, 357–374.

Zamorani, G., Mignoli, M., Hasinger, G., Burg, R., Giacconi, R., Schmidt, M., Trümper, J., Ciliegi, P., Gruppioni, C. & Marano, B. (1999), 'The ROSAT deep survey. V. X-ray sources and optical identifications in the Marano field', *aap* **346**, 731–752.